UPPER EQUATORIAL ATLANTIC CIRCULATION AND COLD TONGUE VARIABILITY

DISSERTATION
ZUR ERLANGUNG DES DOKTORGRADES
DER MATHEMATISCH-NATURWISSENSCHAFTLICHEN FAKULTÄT
DER CHRISTIAN-ALBRECHTS-UNIVERSITÄT
ZU KIEL

vorgelegt von

Verena Hormann

IFM-GEOMAR
Leibniz-Institut für Meereswissenschaften
an der Universität Kiel

Kiel 2008

Referent/in:	Prof. Dr. Peter Brandt
Korreferent/in:	PD Dr. Carsten Eden
Tag der mündlichen Prüfung:	08.12.2008
Zum Druck genehmigt:	08.12.2008

Der Dekan

Abstract

The eastern equatorial Atlantic, with its characteristic cold tongue during boreal summer, is a region where upper ocean variability is reflected in the most obvious way through sea surface temperature (SST) anomalies. This region is of high interest for a better understanding of climate fluctuations in the tropical Atlantic sector because its SST variability is significantly correlated with rainfall variability over the tropical ocean and adjacent land regions. The heat budget in the eastern equatorial Atlantic is largely determined by non-local exchanges, and this study focuses on the role of horizontal advection via zonal currents as well as equatorial waves for SST variability.

The Equatorial Undercurrent (EUC) is studied using a simulation for the period 1990−2002 with a high-resolution ocean general circulation model of the Atlantic Ocean. Simulated transports of the EUC (19.2 Sv across 35°W and 13.7 Sv across 23°W) which supplies the annual mean upwelling in the central and eastern equatorial Atlantic agree well with new transport estimates derived from shipboard observations. Although the observations are not conclusive concerning the seasonal cycle of EUC transports, the simulated seasonal cycles fit largely in the observed range. The analysis of the EUC variability associated with interannual boreal summer variability of the equatorial cold tongue indicates that the supply of cold thermocline waters by the EUC weakens (increases) during warm (cold) events. Additionally, the cold tongue region is found to be affected by equatorial waves.

Moored observations as 20°C-isotherm depth anomalies and dynamic height anomalies at the equator, 35°W and 23°W also indicate the presence of equatorial Kelvin waves during both a warm event in 2002 and a cold event in 2005, with relaxed (intensified) winds in the west and the EUC embedded in a shallower (deeper) thermocline at 23°W during boreal summer 2002 (2005). Basinwide satellite sea surface height anomalies are used to derive an equatorial Kelvin wave mode. The time evolution of this mode represents the basis for a regression analysis to investigate related oceanic variability with respect to differences in upper equatorial Atlantic variability during 2002 and 2005: Compared to the exceptionally strong wave activity in 2002, equatorial Kelvin waves were generally weaker during 2005. The main effect of equatorial Kelvin waves on zonal velocity anomalies at 23°W, 0° is evident well below the EUC core, with a secondary maximum near the surface. Their direct influence on cold tongue SST is small, but they are found to affect the equatorial thermocline slope. Prior to the cold tongue onset in 2002 (2005), the presence of equatorial Kelvin waves results in a flat (inclined) thermocline that is crucial for the shallowing (deepening) of the EUC core at 23°W during boreal summer 2002 (2005) and that might precondition the development of the warm (cold) event.

The present study shows that knowledge about the input from the west and thus about the preconditioning of the upper layer stratification in the eastern equatorial Atlantic by equatorial waves as well as horizontal advection via the zonal currents may be of prime importance for the prediction of Atlantic extreme events.

Zusammenfassung

Der äquatoriale Ostatlantik mit seiner charakteristischen Kaltwasserzunge im Nordsommer ist eine Region, in der sich die Variabilität des oberflächennahen Ozeans am deutlichsten in der Variabilität der Meeresoberflächentemperatur (SST) widerspiegelt. Diese Region ist von großer Bedeutung für ein besseres Verständnis von Klimaschwankungen im atlantischen Raum, da Niederschlagsschwankungen in den Tropen und insbesondere auch über Land eng mit SST-Schwankungen im äquatorialen Ostatlantik verbunden sind. Die Wärmebilanz im äquatorialen Ostatlantik wird auch durch nichtlokale Prozesse bestimmt, und diese Studie konzentriert sich auf die Rolle der Wasserzufuhr zum äquatorialen Auftrieb über Zonalströmungen sowie der äquatorialen Wellen für SST-Schwankungen.
Der Äquatoriale Unterstrom (EUC) wird anhand einer Simulation für den Zeitraum $1990-2002$ mit einem hochauflösenden Ozeanmodell des Atlantiks untersucht. Im Jahresmittel ist der EUC die wichtigste Quelle zur Versorgung des Auftriebs im zentralen und östlichen äquatorialen Atlantik. Simulierte EUC-Transporte von 19.2 Sv über 35°W sowie 13.7 Sv über 23°W stimmen gut mit neuen Transportabschätzungen aus Schiffsmessungen überein. Obwohl die Beobachtungen keine eindeutige Aussage über den Jahresgang der EUC-Transporte zulassen, fügen sich die simulierten Jahresgänge weitestgehend in den beobachteten Schwankungsbereich ein. Die Analyse von EUC-Schwankungen verbunden mit der interannualen Variabilität der äquatorialen Kaltwasserzunge im Nordsommer zeigt, dass sich der Transport von kaltem Thermoklinenwasser durch den EUC während eines Warmereignisses (Kaltereignisses) abschwächt (verstärkt). Darüberhinaus findet sich auch ein Einfluss von äquatorialen Wellen auf die Region der Kaltwasserzunge.
Anomalien der 20°C-Isothermentiefe sowie der dynamischen Höhe aus verankerten Instrumenten am Äquator bei 35°W und 23°W lassen sowohl während eines Warmereignisses im Jahr 2002 als auch während eines Kaltereignisses im Jahr 2005 auf äquatoriale Kelvinwellen schließen. Im Nordsommer 2002 (2005) zeigt sich dabei eine Abschwächung (Verstärkung) der Winde über dem Westatlantik und der EUC ist in eine flachere (tiefere) Thermokline bei 23°W eingebettet. Beckenweite Anomalien der Meeresoberflächenhöhe aus Satellitenmessungen werden zur Bestimmung eines äquatorialen Kelvinwellen Modus verwendet. Die zeitliche Entwicklung dieses Modus stellt die Basis für eine Regressionsanalyse dar, um die mit dem Modus verbundene ozeanische Variabilität im Hinblick auf Unterschiede in der Variabilität des oberflächennahen äquatorialen Atlantiks während der Jahre 2002 und 2005 zu untersuchen: Während 2002 eine außergewöhnlich starke Wellenaktivität zu beobachten ist, waren die äquatorialen Kelvinwellen 2005 vergleichsweise schwach. Der größte Effekt äquatorialer Kelvinwellen auf Anomalien der Zonalgeschwindigkeit bei 23°W, 0° findet sich deutlich unterhalb des EUC-Kerns, mit einem zweiten Maximum nahe der Oberfläche. Die direkten Auswirkungen dieser Wellen auf die SST in der Kaltwasserzunge sind klein, aber es wurde ein Einfluss auf die äquatoriale Thermoklinenneigung festgestellt. Die Präsenz äquatorialer Kelvinwellen führt zu einer flachen (geneigten) Thermokline vor dem

Einsetzen der Kaltwasserzunge im Jahr 2002 (2005), die entscheidend ist für die Verflachung (Vertiefung) des EUC-Kerns im Nordsommer 2002 (2005) und die die Entwicklung des Warmereignisses (Kaltereignisses) begünstigt haben könnte.
Diese Studie zeigt, dass Kenntnisse über den Eintrag aus dem Westbecken und damit über eine Präkonditionierung der oberflächennahen Schichtung im äquatorialen Ostatlantik durch äquatoriale Wellen und Advektion über die Zonalströmungen von großer Bedeutung für eine Vorhersage von atlantischen Extremereignissen sein können.

Contents

Publications

Chapter 3 Brandt, P., F. A. Schott, C. Provost, A. Kartavtseff, V. Hormann, B. Bourlès, and J. Fischer (2006), Circulation in the central equatorial Atlantic: Mean and intraseasonal to seasonal variability, Geophys. Res. Lett., 33 (L07609), doi:10.1029/2005GL025498.

Fischer, J., V. Hormann, P. Brandt, F. A. Schott, B. Rabe, and A. Funk (2008), The South Equatorial Undercurrent in the western to central tropical Atlantic, Geophys. Res. Lett., 35 (L21601), doi:10.1029/2008GL035753.

Chapter 4 Hormann, V., and P. Brandt (2007), Atlantic Equatorial Undercurrent and associated cold tongue variability, J. Geophys. Res., 112 (C06017), doi:10.1029/2006JC003931.

Chapter 5 Hormann, V., and P. Brandt (2008), Upper equatorial Atlantic variability during 2002 and 2005 associated with equatorial Kelvin waves, J. Geophys. Res., submitted.

Appendix A2 Brandt, P., V. Hormann, B. Bourlès, J. Fischer, F. A. Schott, L. Stramma, and M. Dengler (2008), Oxygen tongues and zonal currents in the equatorial Atlantic, J. Geophys. Res., 113 (C04012), doi:10.1029/2007JC00435.

1. Introduction

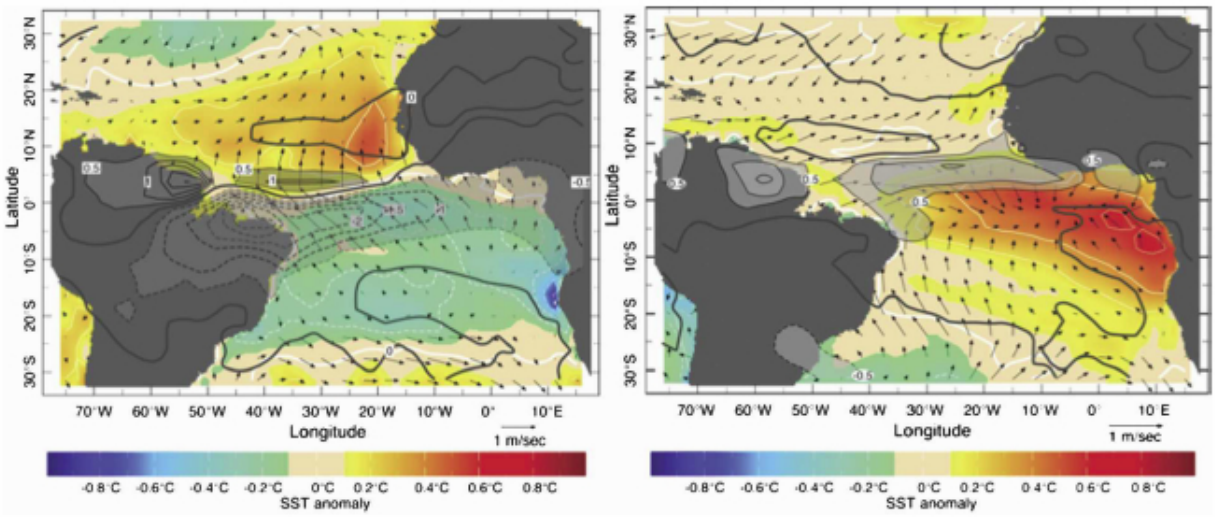

Figure 1.1: The dominant pattern of surface ocean-atmosphere variability in the tropical Atlantic region during (left) boreal spring and (right) boreal summer. The black contours depict the first empirical orthogonal function (EOF) of the regional March - April and June - August rainfall anomaly (from Global Precipitation Climatology Project data 1979 – 2001) [mm/day]. The EOFs explain 33% and 23% of the seasonal variance in boreal spring and summer, respectively. The colored field is the March - April and June - August SST anomaly [°C, white contours every 0.2°C] regressed on the principal component time series of the rainfall EOF. Arrows depict the seasonal mean surface wind vector [m/s], regressed on the same time series (see arrow scale below frame). [*Kushnir et al.*, 2006]

The ocean is of major importance for tropical Atlantic variability mainly through the influence of tropical Atlantic sea surface temperature (SST) on variations of the Atlantic marine Intertropical Convergence Zone (ITCZ) complex. Climate fluctuations in the tropical Atlantic sector are dominated by two distinct patterns of coupled ocean-atmosphere variability (Figure 1.1). These modes, collectively referred to as tropical Atlantic variability (TAV), are tightly phase locked to the pronounced Atlantic seasonal cycle and vary on interannual to decadal time scales. During boreal spring, when the equatorial Atlantic is uniformly warm, conditions are favorable for the development of an interhemispheric

gradient of SST anomalies often termed as the meridional mode. The so-called zonal mode is frequently viewed as the Atlantic counterpart of the Pacific El Niño Southern Oscillation (ENSO) and is most pronounced during boreal summer coinciding with the seasonal development of the eastern cold tongue [e.g., *Weare*, 1977; *Merle et al.*, 1980; *Xie and Carton*, 2004; *Kushnir et al.*, 2006; *Chang et al.*, 2006].

The most notable climate impacts of these modes in the tropical Atlantic sector are the variability of rainfall over northeast Brazil and the coastal regions surrounding the Gulf of Guinea, as well as fluctuations in rainfall and dustiness in sub-Saharan Africa (Sahel) (see Figure 1.1). During boreal summer, rainfall variability is well correlated with SST anomalies along the equator and to the south in the eastern cold tongue region. In this case, the rainfall increases on the anomalously warmer side of the mean ITCZ leading to an impact on the Guinean coast [e.g., *Giannini et al.*, 2003; *Xie and Carton*, 2004; *Kushnir et al.*, 2006; *Chang et al.*, 2006]. This phenomenon has led to speculations that, akin to the Pacific ENSO mode, the underlying feedback in the Atlantic zonal mode is also the dynamical *Bjerknes* [1969] mechanism [e.g., *Zebiak*, 1993; *Xie and Carton*, 2004; *Chang et al.*, 2006; *Keenlyside and Latif*, 2007]. Although the growth rate in the Atlantic is up to 50% smaller compared to the Pacific, the Bjerknes feedback was found to be strong during boreal spring and summer [*Keenlyside and Latif*, 2007]. But due to the weaker net feedback, other mechanisms can also contribute to SST variability in the eastern equatorial Atlantic: 1) There may be a possible link between the two TAV modes as first suggested by *Servain et al.* [1999], and 2) ENSO may act as a remote forcing of equatorial Atlantic variability [e.g., *Carton and Huang*, 1994; *Latif and Grötzner*, 2000].

Wyrtki [1975] early proposed that long equatorial waves play a fundamental role in the context of ENSO. During the extensively studied Atlantic warm event in 1984 that revealed in many respects conditions similar to those during an El Niño [e.g., *Philander*, 1986; *Katz et al.*, 1986; *Hisard et al.*, 1986; *Weisberg and Colin*, 1986], *Katz* [1987] also observed prominent eastward propagations along the equator with first baroclinic mode Kelvin wave characteristics. But *Carton and Huang* [1994] pointed out that the role of subsurface ocean dynamics can be different during individual Atlantic warm events: By contrasting responses of a model simulation to the observed wind changes during 1983/84 and 1987/88, they showed that the subsurface ocean played a preconditioning role for the warm event in 1984 while such a role was not evident for the warm event in 1988.

Equatorial Kelvin waves also cause perturbations in the zonal current field. A model study by *Seidel and Giese* [1999] showed that the passage of these waves at the onset of the 1997/98 ENSO event was associated with an initial strengthening of the Pacific Equatorial Undercurrent (EUC) followed by a rapid shutdown. Such a weakening of the EUC during ENSO was first noted by *Firing et al.* [1983] and attributed to an adjustment of the EUC to the relaxed pressure gradient created by the westerly wind anomalies in the

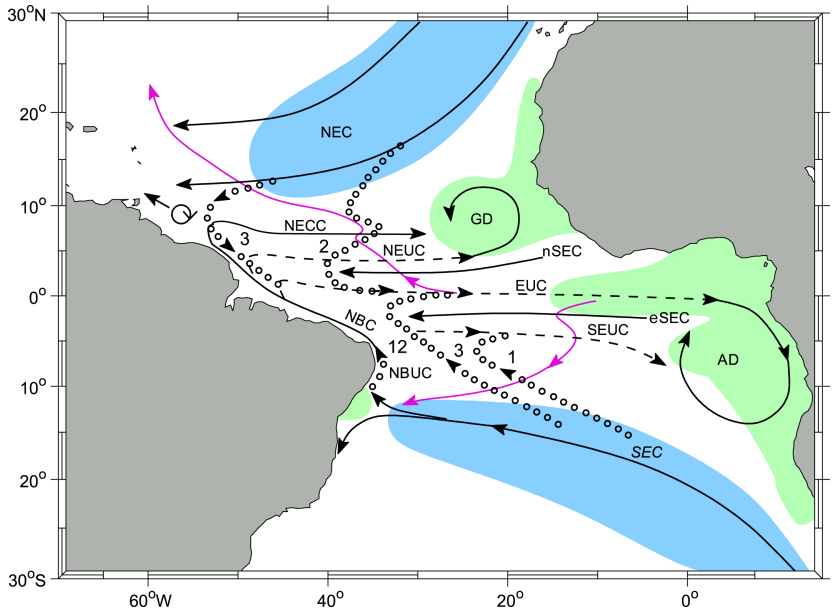

Figure 1.2: Schematic representation of the Atlantic STC circulation with subduction (blue) and upwelling (green) zones. Current branches participating in STC flows are EUC, North and South Equatorial Currents (NEC and SEC), North Equatorial Countercurrent (NECC), North and South Equatorial Undercurrents (NEUC and SEUC), North Brazil Current (NBC) and Undercurrent (NBUC), Guinea and Angola Domes (GD and AD). Interior equatorward thermocline pathways dotted, transport estimates [Sv = 10^6 m^3/s] marked for interior and western boundary pathways; surface poleward pathways for the central basin (from drifter tracks, after *Grodsky and Carton* [2002]) marked by magenta line. [After *Schott et al.*, 2004]

western and central Pacific. But at odds with expectations, the observations by *Hisard and Hénin* [1987] during the warm event in 1984 revealed that the Atlantic EUC appeared to remain relatively strong and to penetrate nearly to the eastern boundary at the peak of this event.

The EUC is also the primary equatorial branch of the Atlantic subtropical cells (STCs) that connect the subtropical subduction regions of both hemispheres to the eastern equatorial upwelling regimes by equatorward thermocline and poleward surface flows (Figure 1.2) [e.g., *Liu et al.*, 1994; *McCreary and Lu*, 1994; *Malanotte-Rizzoli et al.*, 2000; *Schott et al.*, 2004]. One function of the STCs is to provide the cool subsurface water that is required to maintain the tropical thermocline. For this reason, STC variability has been hypothesized to be important for the decadal modulation of ENSO and for Pacific decadal variability, and it may affect Atlantic equatorial SST as well [*Snowden and Molinari*, 2003; *Schott et al.*, 2004]. In the Atlantic, STC pathways are complicated by their interaction with the other ocean currents, in particular the northward flow of warm water by the

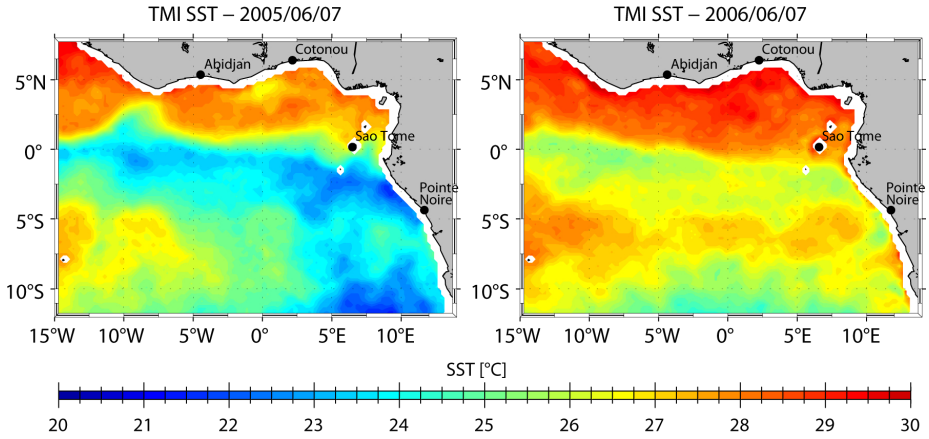

Figure 1.3: Maps of SST [°C] as measured by the microwave imager on board the Tropical Rainfall Measuring Mission (TRMM) satellite: June 7, 2005 (left) and June 7, 2006 (right). [After *Bourlès et al.*, 2007]

meridional overturning circulation (MOC) [*Ganachaud and Wunsch*, 2001; *Lumpkin and Speer*, 2003]. As a consequence of these interactions, the southern STC is stronger than the northern one [e.g., *Malanotte-Rizzoli et al.*, 2000; *Fratantoni et al.*, 2000; *Zhang et al.*, 2003]. The STCs also interact with even shallower overturning cells confined to the tropics that are associated with downwelling driven by the decrease of the poleward Ekman transport $4-6°$ off the equator [e.g., *Liu et al.*, 1994; *McCreary and Lu*, 1994]. *Inui et al.* [2002] pointed out that the Atlantic STCs are sensitive to changes in wind stress, and it has been established that wind-driven STC transport variations ($v'\bar{T}$-hypothesis: *Kleeman et al.* [1999]) are more relevant than advection of subducted temperature anomalies by the mean STC currents ($\bar{v}T'$-hypothesis: *Gu and Philander* [1997]) in generating equatorial SST anomalies [*Schott et al.*, 2004]. The supply of the upwelling regions is foremost by the EUC but also, at somewhat deeper thermocline levels, by the NEUC and SEUC at $3-5°$ in latitude (see Figure 1.2) [*Schott et al.*, 2004]. Thus, understanding EUC variability is important because it can affect SST through its effects on equatorial upwelling.

The main objective here is to determine the role of ocean dynamics for SST variability in the eastern equatorial Atlantic, focusing on horizontal advection via zonal currents and equatorial wave processes. As illustrated in Figure 1.1 (right), interannual cold tongue SST variability during boreal summer is closely linked with wind and rainfall fluctuations over wide areas of the tropical Atlantic sector. This correlation suggests a potential predictability of rainfall variability in case of a predictability of SST. In this regard ocean dynamics are of significance and thus investigating their role in cold tongue SST variability, such as the large interannual SST difference noted during June 2005 and 2006 (Figure 1.3) [*Bourlès et al.*, 2007], is crucial.

The outline of this study, with the presented results based on already published or submitted manuscripts, is as follows: Chapter 2 introduces the used data, including various kinds of observations as well as a numerical model simulation. A brief review of the tropical Atlantic circulation is provided in Chapter 3 before discussing the mean flow in the western to central equatorial Atlantic from the available shipboard observations. The Atlantic EUC and associated cold tongue variability are then analyzed using the numerical model simulation (Chapter 4), while the upper equatorial Atlantic variability during 2002 and 2005 associated with equatorial Kelvin waves is investigated by use of moored and satellite observations (Chapter 5). A concluding synthesis of the results is given in Chapter 6.

2. Data

2.1 Shipboard observations

In this study, current and hydrographic data from several ship cruises carried out in the equatorial Atlantic are analyzed (Table 2.1). For direct current measurements, vessel-mounted (VM) and lowered (L) acoustic Doppler current profilers (ADCPs) have usually been in use. Near the western boundary, some additional Pegasus drop sonde profilings were applied during $1990 - 1994$ [see *Schott et al.*, 2003]. The VM-ADCP data cover the range between about 30 m and some intermediate depth, depending on instrument type used. Uncertainties of 1 h VM-ADCP averages were estimated to be better than $2-4$ cm/s [*Fischer et al.*, 2003] and the accuracy of L-ADCP data was assumed to be better than 5 cm/s [*Visbeck*, 2002]. Hydrographic parameters, i.e. temperature, salinity and dissolved oxygen (O_2), have been obtained from different conductivity-temperature-depth (CTD) systems. Typical accuracies for these measurements are 0.002°C for temperature, 0.002 for salinity and 1% for dissolved oxygen, with salinity and oxygen sensors calibrated versus water samples. During post-processing, all available current measurements are merged with respect to the higher accuracy and better horizontal resolution of the VM-ADCP. For each section, the current and hydrographic data are finally mapped on a regular horizontal (0.05°) and vertical (10 m) grid using a Gaussian interpolation scheme.

Cruise	Section	Measurements
Meteor (Oct. 1990)	35°W, 5°S - 2.5°N	VM-ADCP, L-ADCP, Pegasus, CTD-O_2
Meteor (Jun. 1991)	35°W, 5.5°S - 2.5°N	VM-ADCP, L-ADCP, Pegasus, CTD-O_2
	$\sim$ 31°W, 5.25°S - 0°	VM-ADCP, L-ADCP, Pegasus, CTD-O_2
Meteor (Nov. 1992)	35°W, 5°S - 4°N	VM-ADCP, L-ADCP, Pegasus, CTD-O_2
L'Atalante (Feb. 1993)	35°W, 5°S - 7.5°N	VM-ADCP, CTD-O_2

(Cont.)

Cruise	Section	Measurements
Maurice Ewing (Feb./Mar. 1994)	31°W, 11.25°S - 1°S	VM-ADCP, CTD-O_2
Meteor (Mar. 1994)	35°W, 5°S - 4.5°N	VM-ADCP, L-ADCP, Pegasus, CTD-O_2
Le Noroit (Sep. 1995)	35°W, 5°S - 7.5°N	VM-ADCP, CTD-O_2
Meteor (Mar. 1996)	$\sim$ 26°W, 6°S - 0°	VM-ADCP, CTD
Edwin A. Link (Apr. 1996)	35°W, 4.5°S - 7.5°N	VM-ADCP, L-ADCP, CTD
Thalassa (Jul./Aug. 1999)	35°W, 5°S - 7°N	VM-ADCP, L-ADCP, CTD-O_2
	23°W, 6°S - 6°N	VM-ADCP, L-ADCP, CTD-O_2
Seward Johnson (Jan. 2000)	28°W, 6°S - 0°	L-ADCP, CTD
	25.5°W, 6°S - 4°N	L-ADCP, CTD
	23°W, 6°S - 4°N	L-ADCP, CTD
Meteor (Apr. 2000)	35°W, 5°S - 5°N	VM-ADCP, L-ADCP, CTD-O_2
	23°W, 5°S - 4°N	VM-ADCP, L-ADCP, CTD-O_2
Sonne (Dec. 2000)	35°W, 5°S - 9°N	VM-ADCP, L-ADCP, CTD-O_2
Oceanus (Mar. 2001)	35°W, 1°S - 7°N	VM-ADCP, L-ADCP, CTD
Ron Brown (Feb. 2002)	35°W, 6°S - 7°N	VM-ADCP, L-ADCP, CTD
Meteor (May 2002)	35°W, 5.5°S - 8°N	VM-ADCP, L-ADCP, CTD-O_2
	28°W, 11.5°S - 2.5°N	VM-ADCP, L-ADCP, CTD-O_2
Meteor (Oct. 2002)	24°W, 0° - 10°N	VM-ADCP, CTD
Sonne (May 2003)	35°W, 5°S - 6.5°N	VM-ADCP, L-ADCP, CTD-O_2
	28.5°W, 11.5°S - 2.5°S	VM-ADCP, L-ADCP, CTD-O_2
Ron Brown (Aug. 2003)	$\sim$ 27°W, 6°S - 10°N	VM-ADCP, L-ADCP, CTD-O_2

(Cont.)

Cruise	Section	Measurements
Meteor (Aug. 2004)	35°W, 5.5°S - 5°N	VM-ADCP, L-ADCP, CTD
	∼ 29°W, 5°S - 2°N	VM-ADCP
	28°W, 5°S - 2°N	VM-ADCP, L-ADCP, CTD
Polarstern (Jun. 2005)	23°W, 20°S - 20°N	VM-ADCP
Meteor (May 2006)	∼ 23°W, 2°S - 0.5°N	VM-ADCP
Ron Brown (Jun. 2006)	23°W, 5°S - 20°N	VM-ADCP, CTD-O_2
Ron Brown (Jun./Jul. 2006)	23°W, 5°S - 14.5°N	VM-ADCP, CTD-O_2
Meteor (Jun./Jul. 2006)	35°W, 5°S - 5°N	VM-ADCP, CTD-O_2
	23°W, 4°S - 15.25°N	VM-ADCP, CTD-O_2
	10°W, 1.5°S - 1.5°N	VM-ADCP, CTD-O_2
	0°, 23°W - 10°W	VM-ADCP, CTD-O_2
	2°N, 22°W - 11°W	VM-ADCP, CTD-O_2
Ron Brown (May 2007)	23°W, 4°N - 20°N	VM-ADCP, CTD-O_2
James Clark Ross (May 2007)	∼ 30°W, 10°S - 10°N	VM-ADCP
L'Atalante (Feb./Mar. 2008)	23°W, 2°S - 14°N	VM-ADCP, L-ADCP, CTD-O_2
Polarstern (Apr./May 2008)	∼ 26°W, 20°S - 20°N	VM-ADCP

Table 2.2: Ship cruises carried out in the western and central equatorial Atlantic during 1990 – 2008.

2.2 Moored observations

Data from two equatorial current meter moorings at 35°W and 23°W are also used here together with data from nearby Pilot Research Moored Array in the Tropical Atlantic (PIRATA, http://www.pmel.noaa.gov/pirata) moorings [*Servain et al.*, 1998]. The current meter mooring at 35°W was deployed in August 2004 and finally recovered in June 2006. At about 150 m depth, two ADCPs looking up- and downward, with a typical measurement range of 350 m each, were in use. At 500 m, 652 m, 809 m, and 1107 m additional Sontek (Argonaut) acoustic current meters were applied. The first current meter mooring at 23°W, consisting (among other instruments[1]) of one upward looking ADCP at about

[1] The horizontal velocity measurements at intermediate depths as used in *Bunge et al.* [2008] were not available here.

130 m depth, was deployed in December 2001 and recovered in December 2002 within the framework of the PIRATA program [e.g., *Provost et al.*, 2004; *Giarolla et al.*, 2005]. The successive second and third deployment periods began in February 2004 and lasted to June 2006. During these deployment periods, the mooring was equipped with both an up- and a downward looking ADCP covering the water column from the near-surface down to about 700 m. Unfortunately, a reexamination of the raw data revealed an erroneous behavior of two of the four beams of the upward looking ADCP used during the second deployment period from February 2004 to May 2005 [see *Brandt et al.*, 2006] and these data are excluded in Chapter 5. However, ADCP data of both instruments from each individual equatorial mooring at 35°W and 23°W are combined to a continuous data set. The combined data sets have variable depth limits due to mooring motions and in each case a gap of about 30 m arising from the separation of the two ADCP transducers plus their individual blanking distance. These gaps are filled by a Lagrangian interpolation algorithm and the accuracy of the interpolation was estimated as follows: Using the interpolated field as a reference, a similar gap but with different temporal variability was introduced and the interpolation repeated. Statistics (reference versus interpolated field) showed a negligible mean difference (< 1 cm/s) at a standard deviation of about $3 - 5$ cm/s, which appears small relative to the mean speed of the EUC (the gaps are near the EUC center). Finally, the data (5 m resolution, 1 h intervals) are detided by applying a 40 h low-pass filter and by subsequent subsampling to 12 h resolution.

At the PIRATA moorings, temperature is recorded at 11 depths between 1 and 500 m, with 20 m spacing in the upper 140 m. In this study, daily values at 23°W, 0° are used and gaps are filled by the Langrangian interpolation algorithm as also applied to the velocity gap of about 30 m arising from the separation of the two ADCP transducers. Besides, daily 20°C-isotherm depth and dynamic height data at the equator, 35°W and 23°W are utilized as provided by the PIRATA project. Note that corresponding time series farther east are very gappy during the current meter deployment periods, in particular nearly no data are available in 2002, and thus data from equatorial PIRATA moorings at 10°W and 0° are not considered here. The depth of the 20°C-isotherm was calculated from temperature profiles using linear interpolation of depth versus temperature and dynamic heights were computed from temperature profiles by vertically integrating the specific volume anomaly from the surface to 500 m depth, resulting in dynamic heights at the sea surface referenced to 500 decibars [*Servain et al.*, 1998].

2.3 Satellite observations

Additionally, satellite products of sea surface height (SSH), surface wind stress and SST are used in this study. Multimission gridded SSHs, generated by the SSALTO/DUACS[2] altimeter data processing software and computed with respect to a 7-year mean, are obtained from Archiving, Validation and Interpretation of Satellite Oceanographic data (AVISO, http://www.aviso.oceanobs.com). The horizontal resolution is regularly $1/3^\circ \times 1/3^\circ$ on a Mercator grid, while the temporal resolution is 7 days prior to mid-February 2003 and 3 to 4 days thereafter. Daily surface wind stress fields, as retrieved from the NASA SeaWinds scatterometer on board QuikSCAT, are provided by the Centre de Recherche et d'Exploitation Satellitaire (CERSAT, http://cersat.ifremer.fr) on global $1/2^\circ \times 1/2^\circ$ resolution geographical grids. In order to reconstruct gap-filled and averaged synoptic fields from discrete observations, a statistical interpolation was performed at CERSAT using an objective method. Besides, daily Microwave Optimally Interpolated SST data based on the microwave imager on board the TRMM satellite are used here. The gridded SST fields as provided at http://www.remss.com were derived by blending together the available data using the optimum interpolation scheme described in *Reynolds and Smith* [1994], with a horizontal resolution of $1/4^\circ \times 1/4^\circ$. These satellite data sets are finally mapped on a common 3.5-days temporal and $1/2^\circ \times 1/2^\circ$ spatial grid using linear interpolation in time and a Gaussian interpolation scheme in space, with coastal regions less than 500 m deep discarded.

2.4 Drifter climatology

Drifters sample regions of the ocean inhomogeneously which can cause aliased time-mean values if the presence of strong seasonal variations is neglected. To address this, *Lumpkin* [2003] developed a methodology to simultaneously decompose the drifter observations into time-mean, seasonal and eddy components. Climatological monthly mean fields of the tropical Atlantic, as provided at http://www.aoml.noaa.gov/phod/dac/drifter_climatology.html on a regular $1^\circ \times 1^\circ$ grid, were derived by combining and integrating time-mean, annual and semiannual components of the total velocity; results were smoothed via optimum interpolation (OI), assuming a Gaussian autocorrelation function with an isotropic e-folding scale of 150 km [*Lumpkin and Garzoli*, 2005].

[2] Segment Sol multimissions d'Altimétrie, d'Orbitographie et de localisation précise/Data Unification and Altimeter Combination System

2.5 FLAME

This study also utilizes monthly mean fields of a numerical model simulation performed as part of the Family of Linked Atlantic Ocean Model Experiments (FLAME) hierarchy of models for studying various aspects of the Atlantic Ocean [*Dengg et al.*, 1999]. FLAME follows up the kind of ocean models as used in the Community Modeling Effort (CME) [*Bryan and Holland*, 1989; *Böning and Bryan*, 1996] and the European Dynamics of North Atlantic Models (DYNAMO) ocean model intercomparison study [*Willebrand et al.*, 2001]. The numerical code[3] is based on a refined configuration [*Redler et al.*, 1998] of the GFDL MOM 2.1 code [*Pacanowski*, 1995]. The model domain covers the Atlantic Ocean between 18°S and 70°N, 100°W and 30°E, with a horizontal resolution of 1/12° in longitude and $1/12° cos\,\phi$ in latitude. This z-coordinate model version uses 45 levels in the vertical, with 10 m - resolution near the surface, smoothly increasing to a maximum of 250 m below 2250 m. Vertical mixing is parameterized based on the stability-dependent scheme for vertical diffusivity ($\kappa_h = 0.1 - 4.0$ cm^2/s) and viscosity ($\kappa_m = 2.0 - 10.0$ cm^2/s) as described in *Böning and Kröger* [2005], and a KT-scheme [*Kraus and Turner*, 1967] is used for the mixed layer. The model uses biharmonic friction and isopycnal diffusion, with a diffusivity of 50 m^2/s and a viscosity of $2 \cdot 10^{10}$ m^4/s. The model spin-up starts from the Levitus climatology [*Boyer and Levitus*, 1997] for 10 model years under climatological forcing, based on the monthly mean wind stresses and linearized heat fluxes as derived from European Center for Medium-Range Weather Forecast (ECMWF) analyses for the years $1986 - 1988$ by *Barnier et al.* [1995]. The surface heat flux includes a relaxation to climatological SST in a formulation following the work of *Haney* [1971]:

$$Q = Q_0 + Q_2 \left(SST_{model} - SST_{clim}\right) \tag{2.1}$$

with $Q_2 = \frac{\partial Q}{\partial SST}\Big|_{SST_{clim}}$ and Q_0 denotes the prescribed surface heat flux. The spin-up phase is followed by an interannually forced period from 1987 to 2003, based on the National Center for Environmental Prediction/National Center for Atmospheric Research (NCEP/NCAR) reanalysis [*Kalnay et al.*, 1996], i.e. the variable surface forcing is realized by adding the monthly net heat flux and wind stress anomalies from the NCEP/NCAR reanalysis to the ECMWF-based climatology data. In the present study, monthly output fields of the time period from 1990 to 2002 are used. Further details and specifications are found in e.g., *Eden and Böning* [2002] and *Hüttl and Böning* [2006].
Monthly mean output fields of the last 2 spin-up years of a second experiment (SPFLAME), based on the same numerical code and with the same vertical and horizontal resolution as described above, are additionally used. Subgrid-scale parameterization are here biharmonic friction and diffusion (with diffusivity of $0.8 \cdot 10^{10}$ m^4/s and viscosity of $2 \cdot 10^{10}$ m^4/s)

[3] http://www.ifm-geomar.de/∼spflame

and a closure for the vertical turbulent kinetic energy (TKE) following *Gaspar et al.* [1990]. The surface forcing is due to the monthly fields of the ECMWF climatology which were linearly interpolated onto the model time. For further information see e.g., *Eden* [2006].

In the context of an extensive model validation, the following monthly observational data sets are considered: National Oceanic and Atmospheric Administration (NOAA) OI SST monthly fields (version 2), derived by a linear interpolation of the corresponding weekly OI fields to daily fields and then averaging the daily values over a month [*Reynolds et al.*, 2002], are utilized. The horizontal resolution is globally $1^\circ \times 1^\circ$ and monthly averages are available from November 1981 onward. Besides, along-track Topex/Poseidon (T/P) sea surface anomalies as produced by the Jet Propulsion Laboratory, PO.DAAC[4] are used. This data set is organized as 10-day repeat cycles and available from September 1992 onward. The sea surface anomaly represents the difference between the best estimate of the sea level and a mean sea surface. The sea level was corrected for atmospheric effects (ionosphere, wet and dry troposphere), effects due to surface conditions (electromagnetic bias) and other contributions (ocean tides, pole tide and inverse barometer). The value of the mean sea surface used to calculate sea surface anomalies is from the mean sea level fields by *Rapp et al.* [1994] computed using Deos3, Seasat and about 15 months of T/P altimeter data [*Berwin and Benada*, 2000]. For the purpose of the present study, the along-track data are first mapped on a regular $1^\circ \times 1^\circ$ grid using a Gaussian interpolation scheme and averaged per month afterward.

[4] Physical Oceanography Distributed Active Archive Center

3. Mean flow

The shallow tropical Atlantic circulation is characterized by vigorous zonal currents in the ocean interior and intense boundary currents near the coasts. In the near-surface layer, the flow structure is largely influenced by the wind (see Figure 3.1) and the seasonal changes of the wind field also lead to variations of this circulation [e.g., *Richardson and McKee*, 1984; *Arnault*, 1987; *Stramma and Schott*, 1999; *Stramma et al.*, 2003; *Schouten et al.*, 2005; *Lumpkin and Garzoli*, 2005]. The quiver plots of the near-surface flow (Figure 3.1) emphasize the strong zonal and western boundary currents, among them the northern and equatorial branches of the SEC (nSEC and eSEC), the NECC and the NBC (see Figure 3.2). The NBC flows northward along the Brazilian coast and after crossing the equator, a component of the NBC retroflects eastward into the EUC. From its western source region,

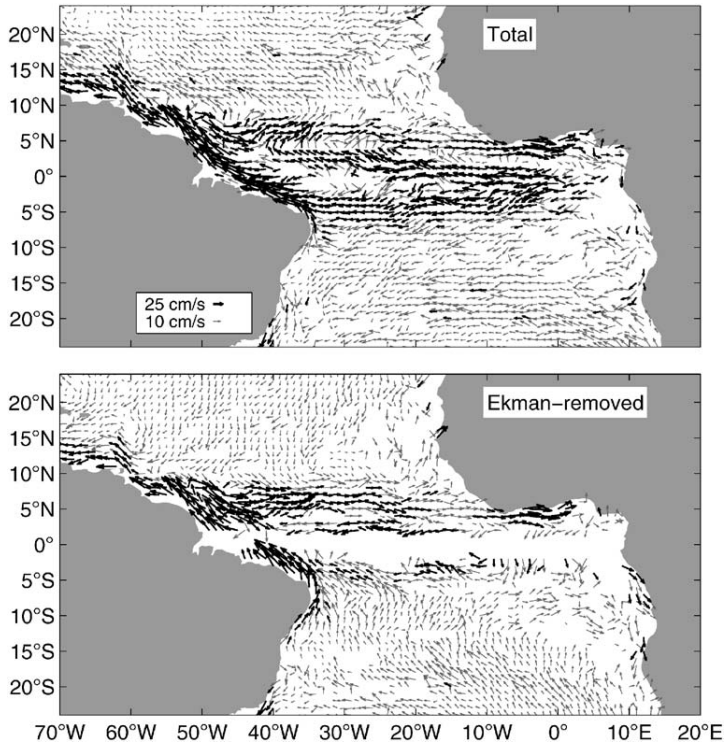

Figure 3.1: Time-mean near-surface currents derived from satellite-tracked drifter trajectories: (Top) total currents and (bottom) Ekman-removed currents. [*Lumpkin and Garzoli*, 2005]

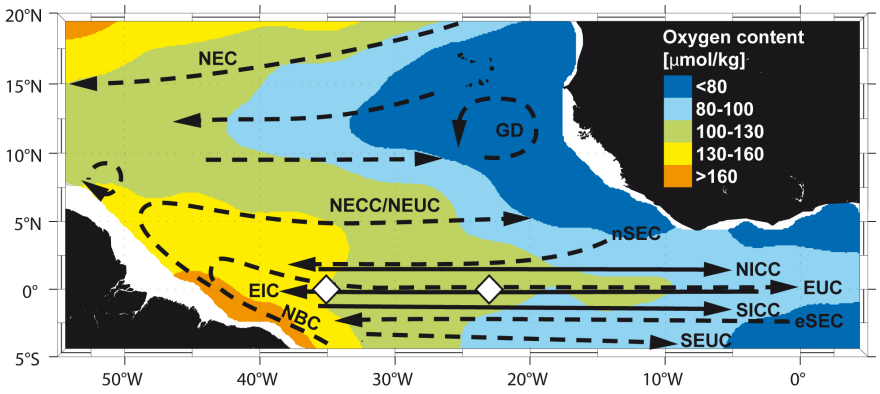

Figure 3.2: Schematic diagram of the shallow subtropical and tropical circulation superimposed on the climatological distribution of oxygen content [μmol/kg] at $300 - 500$ m depth (based on the climatology of *Gouretski and Jancke* [1998]). Also shown are the locations of the equatorial moorings at 35°W and 23°W (white diamonds). Surface and thermocline current branches are marked by black dashed lines, and intermediate currents by black solid lines; see text for details. [After *Brandt et al.*, 2008]

the EUC crosses the entire Atlantic while reducing in strength. In addition, the EUC is one of the main warm water routes of the Atlantic MOC [e.g., *Fratantoni et al.*, 2000; *Hazeleger et al.*, 2003]. Studying the fate of the Atlantic EUC, *Hazeleger and de Vries* [2003] found that about 2/3 of the EUC transport at 20°W contributes to the MOC while about 1/3 recirculates within the STC. On either side of the equator there are additional subsurface current bands transporting water away from the western boundary toward the eastern upwelling regimes of the tropical Atlantic, the NEUC and SEUC (see Figure 3.2).

In the western equatorial Atlantic *Schott et al.* [1995] could verify the existence of the Equatorial Intermediate Current (EIC) from direct velocity measurements, flowing westward underneath the EUC, and two off-equatorial eastward intermediate currents, the Southern and Northern Intermediate Countercurrents (SICC and NICC) at $1.5 - 2.0°$ in latitude. At thermocline and intermediate levels, the western boundary regime is characterized by an oxygen maximum, while the eastern part of the basin is occupied by low-oxygen waters (see Figure 3.2). The strong gradient in the oxygen concentration along the equator is the reason why eastward and westward flows in the equatorial Atlantic can often be identified by high and low oxygen values, respectively. While the (eastward decreasing) oxygen maximum in the thermocline layer associated with the EUC is located directly on the equator [*Metcalf and Stalcup*, 1967; *Tsuchiya et al.*, 1992; *Schott et al.*, 1995], high oxygen values at intermediate depths are typically associated with the eastward flowing SICC and NICC [*Tsuchiya et al.*, 1992; *Schott et al.*, 1995; *Boebel et al.*, 1999; *Bourlès et al.*, 2002]. An analysis of equatorial zonal currents and associated oxygen distributions is found in Appendix A2.

However, *Schott et al.* [2003] presented a first mean zonal velocity section at 35°W from 13 cross-equatorial shipboard profiling sections, with transport estimates for individual current branches. Here, this work is extended to the central part of the Atlantic basin and the mean zonal equatorial circulation of the upper 700 m is now studied based on ship sections taken during 1990 – 2008 (see Table 2.1); the results will also provide a useful validation base for model simulations.

3.1 Central equatorial Atlantic

A mean section of zonal currents is here constructed from 19 VM-ADCP/L-ADCP ship sections taken between 29 – 23°W during 1996 – 2008. Above 30 m, the mean flow field is linearly interpolated toward the mean surface flow obtained from the surface drifter climatology by *Lumpkin and Garzoli* [2005] (see Figure 3.1). The resulting mean zonal current section (Figure 3.3) is then evaluated for transports in the same isopycnal layers that have previously been used for analyzing the mean 35°W section [*Schott et al.*, 2003]. As there is reasonable seasonal coverage of the available sections from the central tropical Atlantic, only a minor seasonal bias is expected.

The EUC transports 14.9 Sv eastward, of which 2.3 Sv occur in the surface layer above $\sigma_\theta = 24.5\,\mathrm{kg/m^3}$, and 12.6 Sv in the thermocline layer $24.5 - 26.8\,\mathrm{kg/m^3}$. The transports across this mean section can be compared with the transport across the mean 35°W section, in the western source region of the EUC.

For this purpose the mean 35°W section of *Schott et al.* [2003], which was based on 13 ship surveys has been updated to 16 sections (Figure 3.4), now adding the subsequent Sonne and Meteor (2) surveys of May 2003 as well as August 2004 and June 2006, respectively. Furthermore, the top layer, for which *Schott et al.* [2003] extrapolated the ADCP shears to the surface, has been treated the same way as the 29 – 23°W section here, i.e. by applying mean surface drifter currents. The resulting mean EUC transport at 35°W amounts to 19.9 Sv, with 5.3 Sv above $\sigma_\theta = 24.5\,\mathrm{kg/m^3}$ and 14.6 Sv in the thermocline layer. While the mean EUC transport is about the same as the value of 20.9 Sv given by *Schott et al.* [2003], the combined effects of added cruises, different surface layer treatment, and reanalysis of earlier cruises result in a somewhat different distribution between surface layer and thermocline layer.

The standard error of the estimated mean EUC transports at both longitudes is evaluated from the standard deviation of EUC transports calculated for each individual section under the assumption of independent individual realizations. The errors of the mean are determined to be 1.5 Sv (n = 15) at 35°W and 1.2 Sv (n = 13) between 29 – 23°W, respectively.

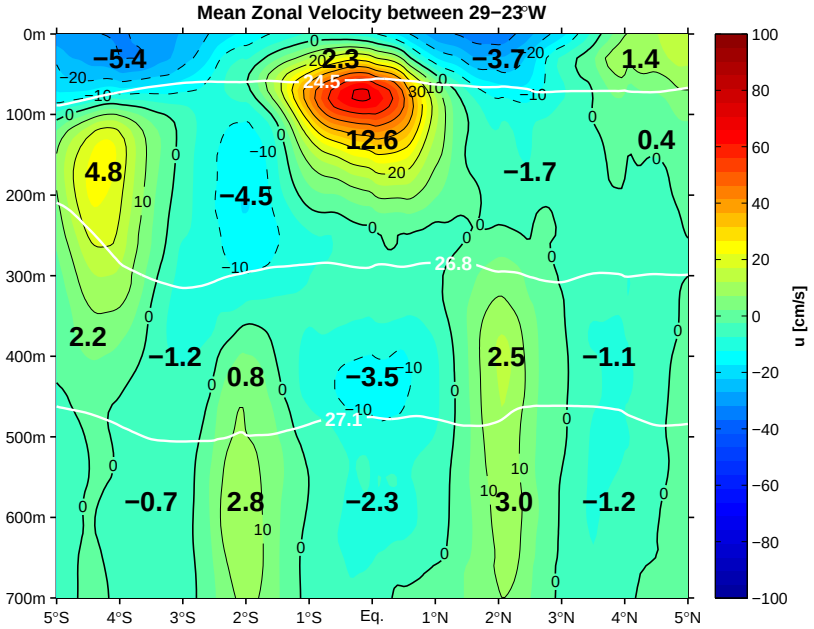

Figure 3.3: Mean zonal velocity distribution from 19 sections taken between $29 - 23°$W [cm/s], with layer transports [Sv] of different current branches overlaid on potential density (white lines). [After *Brandt et al.*, 2006]

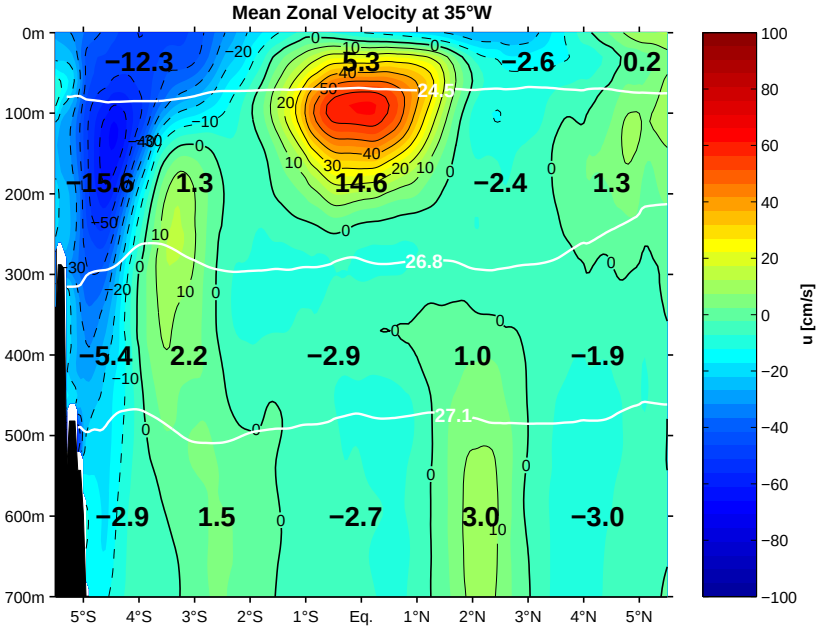

Figure 3.4: Mean zonal velocity distribution from 16 sections taken at 35°W [cm/s], with layer transports [Sv] of different current branches overlaid on potential density (white lines). [After *Schott et al.*, 2003; *Brandt et al.*, 2006]

Thus, there is a significant difference in the mean EUC transports: Over about 1000 km of equatorial extent between both mean sections the EUC loses about 5 Sv.
Underneath the EUC, there is the westward core of the EIC transporting 3.5 Sv in the $\sigma_\theta = 26.8 - 27.1\,\mathrm{kg/m^3}$ density range. To either side of this westward flow, in latitude range $1 - 3°$N and S, there are two narrow eastward cores, in correspondence to what was found at 35°W [*Schott et al.*, 2003], the NICC and SICC.
The SEUC, with its core located at about 4.5°S and 160 m depth, transports 7.0 Sv eastward in the $\sigma_\theta = 24.5 - 27.1\,\mathrm{kg/m^3}$ density range, thus doubling its transport after leaving the 35°W section. The increase occurs solely in the $\sigma_\theta = 24.5 - 26.8\,\mathrm{kg/m^3}$ density range (from 1.3 to 4.8 Sv), while the lower thermocline layer stays constant (2.2 Sv). Inspection of the individual sections between $29 - 23°$W that run to 5°S and reach down to 500 m depth shows that the SEUC actually extends southward to beyond 5°S, i.e. some transport fractions are lost in the average of Figure 3.3, and the SEUC increase along the way eastward from the 35°W section is even larger than these transport numbers express.

3.2 South Equatorial Undercurrent

The evolution of the SEUC from the western to central tropical Atlantic is now investigated in more detail by considering the available meridional sections at 35°W (14 cruises), near 30°W (4 cruises), at 28°W (5 cruises), near 25°W (4 cruises), and at 23°W (4 cruises) between 6°S - 0° (see Table 3.1). Most of the sections covered the total vertical extent of the SEUC at different times of the year, but only at 35°W all seasons are covered. The mean flow across each of the sections (Figure 3.5) is calculated by averaging the gridded individual realizations as an Eulerian mean flow field. At 35°W, the SEUC is only weakly developed at a mean core speed of about 10 cm/s and the onshore flank is bounded by the intense north-westward flowing NBUC; thus the SEUC is shifted more to the north, compared to the SEUC location at the other sections, and centered around 3°S. Besides the zonal component, there are several realizations [see *Schott et al.*, 1998] showing a significant southward (opposite to the NBUC direction) component. Toward the east, already at 30°W and more pronounced at 28°W, the SEUC is significantly stronger (maximum mean speed is above 20 cm/s), and its width and vertical extent are larger than near the boundary at 35°W. East of 35°W, the SEUC core is located slightly south of 4°S. Additionally, the flow at 23°W appeared weaker, but wider than farther west, with slightly less mean SEUC transports compared to 28°W (Table 3.1).

Cruise	Transport [Sv] $(24.5 - 27.1\,\mathrm{kg/m^3})$	Transport [Sv] $(100 - 500$ m)
35°W		
L'Atalante (Feb. 1993)	8.0	8.0
Ron Brown (Feb. 2002)	5.6	5.4
Meteor (Mar. 1994)	3.7	3.6
Edwin A. Link (Apr. 1996)	8.9	9.5
Meteor (Apr. 2000)	8.7	9.3
Meteor (May 2002)	3.7	4.3
Sonne (May 2003)	5.0	4.7
Meteor (Jun. 1991) [100 − 400 m]	(2.9)**	3.7* [1.28]
Meteor (Jun. 2006)	4.0	4.1
Thalassa (Jul. 1999)	4.3	4.3
Meteor (Aug. 2004)	6.6	6.5
Meteor (Oct. 1990)	6.1	6.3
Meteor (Nov. 1992)	3.7	3.9
Sonne (Dec. 2000)	4.6	4.6
Mean	5.6 ($n = 13$)	5.7 ($n = 14$)
Standard error	0.5 ($n = 13$)	0.5 ($n = 14$)
31 − 30°W		
Maurice Ewing (Mar. 1994) [100 − 400 m]	(5.1)**	5.4* [1.03]
James Clark Ross (May 2007)		6.9
Meteor (Jun. 1991)	5.4	5.5
Meteor (Aug. 2004)		8.5
Mean		6.7 ($n = 4$)
Standard error		0.7 ($n = 4$)
28°W		
Seward Johnson (Jan. 2000)	9.5	9.4
Meteor (May 2002)	9.9	10.1
Sonne (May 2003)	10.3	10.4
Polarstern (May 2008) [100 − 250m]		4.6* [1.61]
Meteor (Aug. 2004)	11.2	11.0
Mean	10.2 ($n = 4$)	9.7 ($n = 5$)
Standard error	0.4 ($n = 4$)	0.6 ($n = 5$)
26 − 25°W		
Seward Johnson (Jan. 2000)	4.8	4.8
Ron Brown (Feb. 2005)	10.2	10.0

(Cont.)

Cruise	Transport [Sv] ($24.5 - 27.1\,\mathrm{kg/m^3}$)	Transport [Sv] ($100 - 500$ m)
Meteor (Mar. 1996) [$100 - 450$ m]	(11.2)**	12.9* [1.01]
Ron Brown (Aug. 2003)	10.4	10.4
Mean	8.4 ($n = 3$)	9.6 ($n = 4$)
Standard error	1.8 ($n = 3$)	1.7 ($n = 4$)
23°W		
Seward Johnson (Jan. 2000)	8.6	8.7
Meteor (Apr. 2000)	10.7	10.6
Polarstern (Jun. 2005) [$100 - 300$ m]		6.0* [1.23]
Thalassa (Aug. 1999)	5.1	5.0
Mean	8.1 ($n = 3$)	7.9 ($n = 4$)
Standard error	1.6 ($n = 3$)	1.2 ($n = 4$)

* reduced depth range, scaled by factor in brackets for calculating the mean

** for density range $24.5 - 26.9\,\mathrm{kg/m^3}$, not used in mean

Table 3.2: SEUC transports [Sv] in the western to central tropical Atlantic, for the density range $\sigma_\theta = 24.5 - 27.1\,\mathrm{kg/m^3}$ and the depth range $100 - 500$ m. [*Fischer et al.*, 2008]

The mean transports are derived by averaging the individual section transport estimates, and uncertainties are calculated from the transport standard deviations and the number of (independent) section occupations. In order to incorporate the few data sets with somewhat shallower measurement range, a scaling factor is determined to take that into account. At the respective locations, full range measurements are used to determine full SEUC transports, and secondly, transports over the reduced depth range are derived. The ratio of the two estimates is then used to up-scale the transports from the shallower data sets.

Quantitatively, the SEUC transports increase significantly (see error estimates in Table 3.1) from 5.6 Sv near the western boundary at 35°W to about 10 Sv 800 km farther east. Two types of vertical boundaries are chosen for the transport calculations, isopycnals ($24.5 < \sigma_\theta \leq 27.1\,\mathrm{kg/m^3}$; see Figure 3.5 and Table 3.1) and depth range ($100 - 500$ m); both give roughly the same values. In order to uniformly capture the full SEUC transports from the western boundary to the interior, the here chosen isopycnal range is somewhat wider than that used by *Schott et al.* [1998] for the western boundary only. East of 28°W, the transports of the SEUC remain almost constant, with some insignificant reduction in the area 25°W to 23°W.

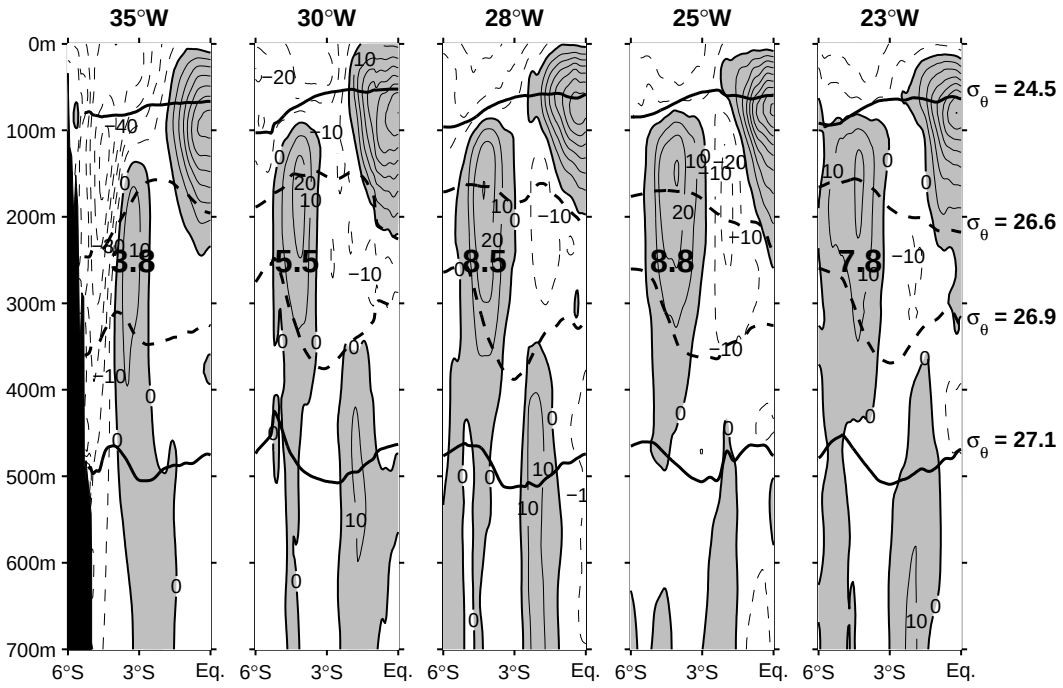

Figure 3.5: Mean sections of zonal velocity at 35°W (14 occupations), near 30°W (4 occupations), at 28°W (5 occupations), near 25°W (4 occupations), and at 23°W (4 occupations); contour interval is 10 cm/s, bold numbers are transports [Sv], isopycnals are included as thick solid (σ_θ = 24.5 and 26.8 kg/m^3) and dashed (σ_θ = 26.6 and 26.9 kg/m^3) black lines, respectively. [*Fischer et al.*, 2008]

In contrast to this method, transport averages are also calculated from the mean (Eulerian) velocity sections of Figure 3.5, which should be somewhat smaller than the average core transports listed in Table 3.1. Particularly, the 35°W transports from the mean velocity section are 3.8 Sv compared to 5.6 Sv and thus by about 30% smaller, which is an indication of relatively large variability in the position of the current core at this location. Large variability and large differences between the two methods point to meandering as the primary source of the variability at 35°W. At 28°W, the scatter of core location is much smaller, and the transport estimates are more similar, at 8.5 Sv and 10.2 Sv, respectively (Table 3.1). Presumably, meandering is less dominant and SEUC pulsation may add to the variability. Finally, at 23°W transports scatter quite significantly, but means are rather similar (7.8 Sv vs. 8.1 Sv) again making pulsations more likely than meandering.

3.3 Summary and discussion

A new mean cross-equatorial section of zonal currents between $29 - 23°$W, based on 19 VM-ADCP/L-ADCP ship sections, was composed and allowed mean transport estimates of the principal equatorial current branches in the central equatorial Atlantic. From an updated earlier mean zonal velocity section at 35°W near the western boundary [*Schott et al.*, 2003] and the new central equatorial Atlantic section, a reduction of the EUC transport by about a quarter is derived, suggesting substantial recirculation into westward flowing current branches surrounding the western EUC. Below the EUC, a mean westward flow associated with the EIC was observed in the shipboard velocity measurements. The EIC transport was estimated to be about 10 Sv between $\sigma_\theta = 26.8\,\mathrm{kg/m^3}$ (about 300 m) and $\sigma_1 = 32.15\,\mathrm{kg/m^3}$ (about 1150 m) at 35°W [*Schott et al.*, 2003]. Out of the 10 Sv at 35°W, about 6 Sv are transported between $\sigma_\theta = 26.8\,\mathrm{kg/m^3}$ and 700 m which is the same value estimated for the central part of the basin. Up to now, the observed westward EIC flow with mean velocities above 5 cm/s could not be reproduced by state-of-the-art numerical models, and *Jochum and Malanotte-Rizzoli* [2003] suggested that the shipboard measurements represented snapshots in time that were biased by seasonal Rossby waves.

Near its origin at 35°W, the SEUC transport is fairly well determined to be 5.6 ± 0.5 Sv and it increases substantially during its eastward progression; at 28°W the transport has almost doubled and then stays fairly constant (just a slight decay) out to 23°W. This transport variation is caused by a significant increase in SEUC volume and core velocity. Water mass properties indicated that the SEUC is not supplied out of the oxygen-rich and low-salinity NBUC, but is mostly made up of low-oxygen interior recirculation waters out of the SEC [*Schott et al.*, 1998], yet recognizable by admixtures of boundary waters [*Arhan et al.*, 1998]. A supply through interior recirculations is also suggested by comparing the almost nonexistent SEUC above $\sigma_\theta = 26.6\,\mathrm{kg/m^3}$ at 35°W with the strong eastward flow in the same layer but farther east (Figure 3.5).
Numerical models of the tropical Atlantic Ocean have been used for investigating the structure and physical mechanisms of the off-equatorial undercurrents: *Jochum and Malanotte-Rizzoli* [2004] suggested by using an idealized model configuration that eddy fluxes induced by tropical instability waves (TIWs) maintain the SEUC in the central equatorial Atlantic. In a more realistic high-resolution simulation of the Atlantic Ocean, *Hüttl-Kabus and Böning* [2008] noted that the SEUC in the western part of the equatorial Atlantic is almost exclusively fed by internal recirculations between eastward and westward current bands. Both these types of present-day models show eastward SEUC flow at the observed latitude, but current speeds and transports are weaker than observed.

Away from the recirculation cells in the western tropical Atlantic, the 23°W section seems to be an optimal place for studying the supply route of thermocline waters toward the eastern equatorial and off-equatorial upwelling regimes. As discussed by *Foltz et al.* [2003] for the seasonal cycle of the upper layer heat budget, zonal temperature advection is of particular importance for the cold tongue region during boreal summer. This might also hold for the interannual variability, with zonal advection contributing significantly to the zonal SST mode, which is associated with interannual wind and rainfall variability of wide areas of the tropical Atlantic [e.g., *Kushnir et al.*, 2006].

4. Equatorial Undercurrent variability

In the Pacific, mean transport and seasonal cycle of the EUC are fairly well known across most of the basin, and EUC variability is known to occur in association with SST variations in the eastern cold tongue region on both seasonal and interannual time scales [*Philander et al.*, 1987; *Yu and McPhaden*, 1999; *Keenlyside and Kleeman*, 2002; *Johnson et al.*, 2002; *Izumo*, 2005].
Presently, little can be said about the seasonal cycle of Atlantic EUC transport from observations, but a sufficient number of cross-equatorial ship sections are now available at 35°W and near 23°W to afford reasonable estimates of the mean EUC structure and transport at these locations (see Section 3.1). Farther east, measurements are sparse and the observed snapshot transports indicate a large variability of the current system [*Hisard and Hénin*, 1987; *Bourlès et al.*, 2002; *Mercier et al.*, 2003]. Due to the limited number of observations in the equatorial Atlantic, a high-resolution ocean model is used here to investigate the Atlantic EUC and associated cold tongue variability.

4.1 Model-data comparison

Mean and seasonal cycle

In order to validate the FLAME model, mean sections at 35°W and at/near 23°W from SPFLAME as well as from observations (see Section 3.1) are considered (Figure 4.1). The mean sections from the models are evaluated for transports in isopycnal layers according to the observations, but because of a too shallow $\sigma_\theta = 24.5\,\mathrm{kg/m^3}$-isopycnal in the FLAME model $\sigma_\theta = 25.4\,\mathrm{kg/m^3}$ is chosen instead as a lower boundary of the surface layer. This feature can primarily be ascribed to a too diffuse thermocline as already noted by *Schott and Böning* [1991] for the CME model. Besides, individual EUC transport estimates from observations at 35°W and at/near 23°W are calculated by taking only eastward velocities into account for both the density range $\sigma_\theta = 24.5 - 26.8\,\mathrm{kg/m^3}$ and the depth range $30 - 300$ m. Mean transports are derived by averaging the individual section transports and uncertainties are estimated from the standard deviation of EUC transports assuming

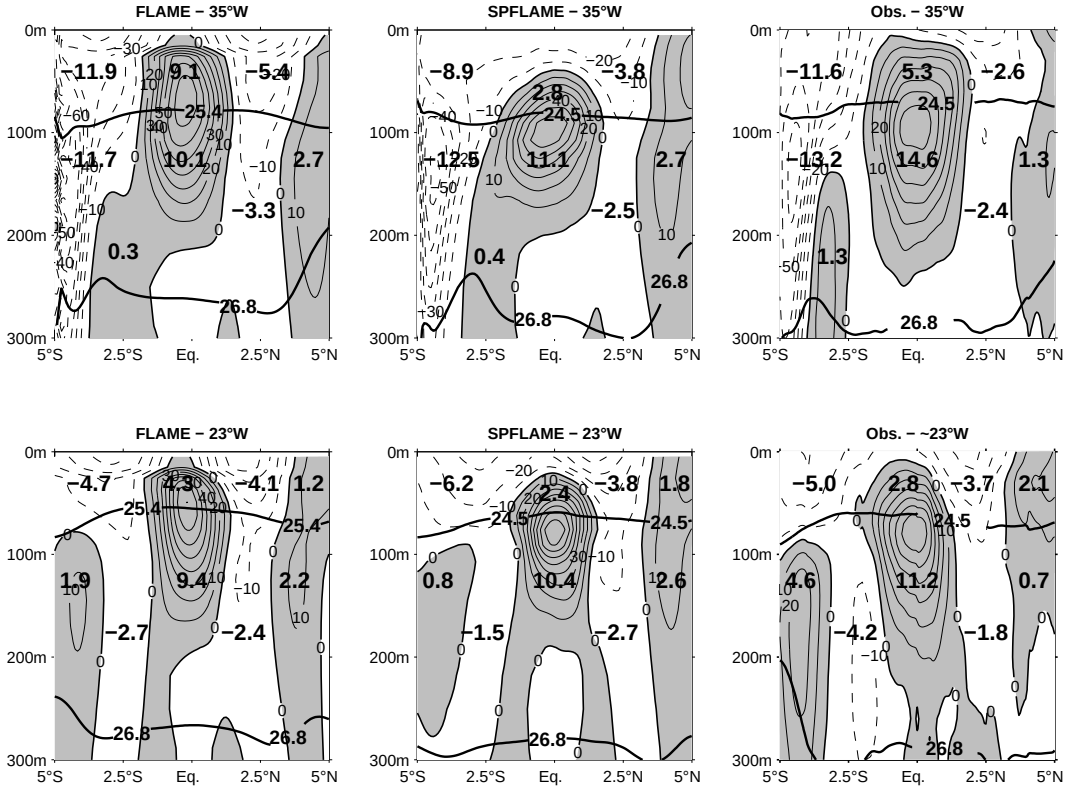

Figure 4.1: Upper panels: Mean zonal velocity [contour interval is 10 cm/s] at 35°W from FLAME (left), SPFLAME (middle) and from 16 ship sections (right), with layer transports [Sv] of different current branches overlaid on potential density (thick solid lines). Lower panels: Mean zonal velocity [contour interval is 10 cm/s] at/near 23°W from FLAME (left), SPFLAME (middle) and from 13 ship sections (right), with layer transports [Sv] of different current branches overlaid on potential density (thick solid lines). [*Hormann and Brandt*, 2007]

independent individual realizations (Table 4.1). The transports for the density range are somewhat smaller compared to the ones for the depth range, thus some eastward transport above $\sigma_\theta = 24.5\,\mathrm{kg/m^3}$ is missed by the chosen density range. In order to capture the total range of EUC transport variability from observations, the transports for the $30 - 300$ m depth range are chosen here. Figure 4.2 presents these individual transport estimates at 35°W and at/near 23°W in comparison with the respective seasonal cycles of EUC transport from both models, calculated from the eastward zonal velocities between ±2.5° in latitude and within the layer $31.5 - 310.6$ m by monthly averaging.

35° W Section. The mean 35°W zonal velocity section from 16 cruises shows the EUC centered at the equator, with its core at about 100 m depth and a maximum velocity of about 65 cm/s. The EUC transport calculated from the mean velocity section amounts to 19.9 Sv,

with 5.3 Sv in the surface layer and 14.6 Sv in the thermocline layer $\sigma_\theta = 24.5 - 26.8\,\mathrm{kg/m^3}$. Although the mean EUC transport at 35°W from the FLAME model (19.2 Sv) is in good agreement with the value derived from observations, the transport distribution between surface and thermocline layer is different, i.e. of nearly equal magnitude. This difference is mainly due to a shallower model EUC core, located slightly south of the equator at about 70 m depth in the surface layer. In case of the SPFLAME model, the vertical extent of the EUC is, particularly toward the surface, much diminished compared to the FLAME model and the observations. But in agreement with the observations, the core of the SPFLAME EUC is found in the thermocline layer at about 100 m depth. Due to its shrunken upper part the EUC transports here only 2.8 Sv in the surface layer and 11.1 Sv in the thermocline layer. The too deep SPFLAME EUC also results in significant differences concerning the westward surface flow. While the FLAME model and the observations show two separated bands of westward flow in the surface layer, the SPFLAME model has just a broad band of westward surface flow. Note that the EUC in both models is not clearly separated from the SEUC in the thermocline layer as indicated by the observations.
The seasonal cycle of EUC transport at 35°W from the FLAME model is characterized by two transport maxima of about equal magnitude during March/April and September. On the other hand, the seasonal cycle of EUC transport in the SPFLAME model run shows a maximum during April and another during November. But EUC transports obtained from 15 cross-equatorial sections at 35°W are in reasonable agreement with both simulated seasonal cycles, with the largest discrepancies during June 1991 and September 1995. Because of the limited number of measurements, the EUC transport observations do not allow to evaluate the quality of the simulated seasonal cycles of both model runs.

23° W Section. As pointed out in Chapter 3, the EUC transport reduces by about a quarter over about 1000 km of equatorial extent between 35°W and about 23°W. This reduction is well reproduced by the FLAME model, with an EUC transport of 13.7 Sv across 23°W compared to 19.2 Sv across 35°W. The differences concerning the characteristics of the mean EUC core from observations and the FLAME model, as noted above for the comparison of the mean 35°W sections, are also apparent in the central Atlantic. But the observed and simulated EUC transport distributions between surface and thermocline layer are in better agreement in the central equatorial Atlantic than near the western boundary. Contrary to the observations, the EUC transport in the SPFLAME model run stays fairly constant, with 12.8 Sv across 23°W compared to 13.9 Sv across 35°W. However, the shape of the SPFLAME EUC is in an overall better agreement with the observations in the central equatorial Atlantic. To the north and south of both observed and simulated EUC, two branches of the westward SEC are present in the surface layer and the corresponding westward transports are of comparable magnitude. Contrary to the

Cruise	Transport [Sv] ($24.5 - 26.8\,\mathrm{kg/m^3}$)	Transport [Sv] ($30 - 300$ m)
L'Atalante, 35°W (Feb. 1993)	18.50	23.67
Ron Brown, 35°W (Feb. 2002)	15.98	20.92
Meteor, 35°W (Mar. 1994)	13.43	19.38
Oceanus, 35°W (Mar. 2001)		
Edwin A. Link, 35°W (Apr. 1996)	16.63	24.55
Meteor, 35°W (Apr. 2000)	13.44	22.58
Meteor, 35°W (May 2002)	15.02	23.98
Sonne, 35°W (May 2003)	17.50	21.81
Meteor, 35°W (Jun. 1991)	24.83	36.24
Meteor, 35°W (Jun. 2006)	17.10	23.52
Thalassa, 35°W (Jul. 1999)	13.54	17.63
Meteor, 35°W (Aug. 2004)	19.24	23.76
Le Noroit, 35°W (Sep. 1995)	23.85	35.83
Meteor, 35°W (Oct. 1990)	19.51	24.77
Meteor, 35°W (Nov. 1992)	14.76	18.63
Sonne, 35°W (Dec. 2000)	12.28	14.75
Mean	17.04 ($n = 15$)	23.47 ($n = 15$)
Standard error	0.96($n = 15$)	1.51 ($n = 15$)
Seward Johnson, 23°W (Jan. 2000)	10.32	15.07
Seward Johnson, 25.5°W (Jan. 2000)	10.87	17.27
Seward Johnson, 28°W (Jan. 2000)		
Meteor, 23°W (Apr. 2000)	9.77	14.19
Meteor, 28°W (May 2002)	9.23	10.47
Sonne, 28.5°W (May 2003)		
Meteor, $\sim$ 23°W (May 2006)		
Polarstern, 23°W (Jun. 2005)		22.48
Meteor, 23°W (Jun. 2006)	19.41	20.17
Thalassa, 23°W (Aug. 1999)	12.81	14.73
Ron Brown, 25°W (Aug. 2003)	21.51	24.50
Meteor, 28°W (Aug. 2004)	14.70	22.01
Meteor, 24°W (Oct. 2002)		
Mean	13.58 ($n = 8$)	17.88 ($n = 9$)
Standard error	1.64 ($n = 8$)	1.56 ($n = 9$)

Table 4.1: EUC transports [Sv] in the western and central equatorial Atlantic from cross-equatorial ship sections, for the density range $\sigma_\theta = 24.5 - 26.8\,\mathrm{kg/m^3}$ and the depth range $30 - 300$ m. [*Hormann and Brandt*, 2007]

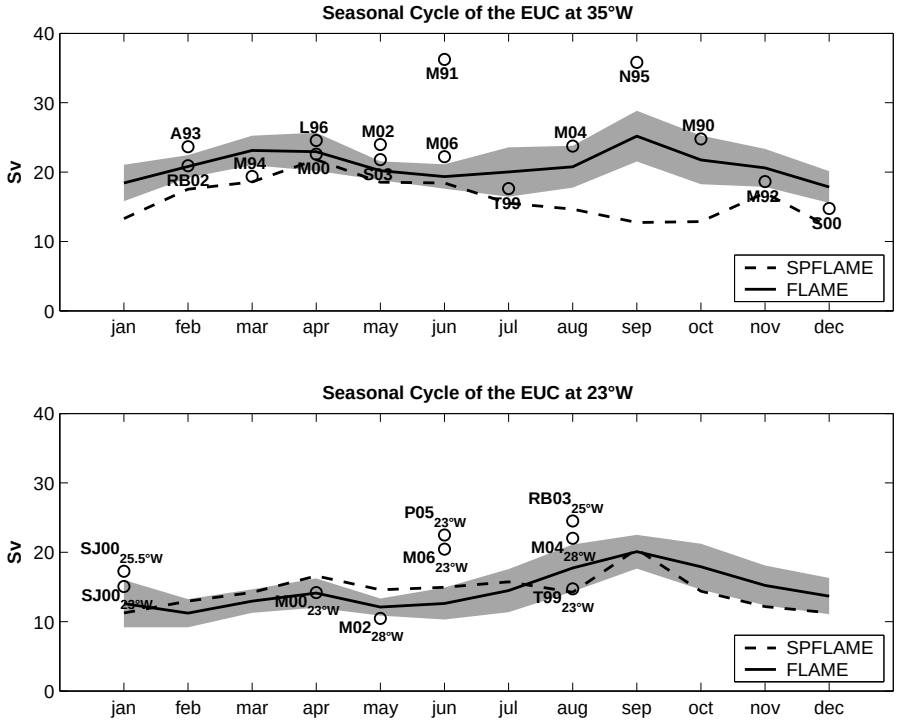

Figure 4.2: Upper panel: Seasonal cycle of EUC transport [Sv], calculated between $\pm 2.5°$ in latitude and within the layer $31.5 - 310.6$ m, at 35°W from FLAME (solid line) and SPFLAME (dashed line), with standard deviation for FLAME (shaded). Marked are EUC transports [Sv] from 15 cross-equatorial ship sections carried out at 35°W during $1990 - 2006$; indicated are shipname (A = L'Atalante, RB = Ron Brown, M = Meteor, L = Edwin A. Link, S = Sonne, T = Thalassa, N = Le Noroit) and year of survey. Lower panel: Same as upper panel, but at 23°W. Marked are EUC transports [Sv] from 9 cross-equatorial ship sections carried out between $29 - 23°$W during $1999 - 2006$; indicated are shipname (SJ = Seward Johnson, M = Meteor, P = Polarstern, RB = Ron Brown, T = Thalassa), year of survey and location. [*Hormann and Brandt*, 2007]

35°W section, the SEUC is clearly separated from the EUC at 23°W in both simulations and its eastward transport amounts to 1.9 Sv and 0.8 Sv in the thermocline layer of the FLAME and SPFLAME model, respectively. In agreement with the mean sections from observations, the simulated SEUCs increase toward the east, but the model transports are significantly lower than observed.

Considering the seasonal cycle of EUC transport at 23°W from the FLAME model, transport maxima during September and April as well as minima during February and May/June are apparent. While the simulated maxima at 35°W are of nearly equal magnitude, the September maximum is significantly stronger compared to the April one at 23°W. Contrary to the 35°W section, the simulated seasonal cycles of EUC transport from FLAME and

SPFLAME are in general agreement in the central equatorial Atlantic. Individual EUC transports are derived here from 9 cross-equatorial sections carried out between $29-23°$W. These snapshot transports exhibit a large range of variability that prevents from establishing a definite seasonal cycle from observations. In particular, one of the highest transport estimates is obtained at 23°W during June 2005, coincident with a minimum of the simulated seasonal cycles.

The comparison between the FLAME and SPFLAME model runs reveals significant differences concerning the annual mean and seasonal cycle of the EUC at 35°W, whereas a general agreement is found at 23°W. As first pointed out by *Pacanowski and Philander* [1981], the simulation of the equatorial upper-layer currents, and in particular the EUC, depends strongly on the parameterization of the vertical mixing of momentum. The strong sensitivity of the simulated EUC to the vertical viscosity is here suspected to be the main reason for differences in the representation of the simulated EUC. Apart from different vertical mixing schemes, the larger discrepancies at 35°W may be attributed to the sensitivity of the recirculation patterns near the western boundary to parameterization choices of lateral mixing as stated by *Böning and Kröger* [2005]. However, analysis of the model sensitivity to different mixing parameterizations is beyond the scope of this study.
Both at 35°W and 23°W, the simulated seasonal cycles of EUC transport from the FLAME model are in general agreement with results presented in previous studies. *Philander and Pacanowski* [1986b, Figure 3] found a maximum EUC transport during July to September at 30°W and 10°W as well as secondary maxima during March/April and January/February, respectively. Likewise, *Schott and Böning* [1991, Figure 8] at 30°W and *Hazeleger et al.* [2003, Figure 2] at 35°W and 20°W yielded comparable results. The basinwide description of the seasonal cycle of EUC transport by *Arhan et al.* [2006, Figure 6a] also revealed two maxima, one during August to November in the basin interior and the other one during January to June, most pronounced between $40-35°$W near the western boundary, but extending eastward to about 10°W. A recent study by *Hüttl and Böning* [2006, Figure 6a], also based on the FLAME hierarchy of models, yielded significant differences concerning the seasonal cycle of the EUC at 35°W in the 1/12° and 1/3° model versions. While the 1/12°-case reveals the double-maximum EUC cycle (see Figure 4.2, upper panel), the boreal winter/spring maximum is missing in the coarser resolution case, attributed to an unrealistically weak thermocline part. These findings by *Hüttl and Böning* [2006] along with the here presented results concerning the seasonal cycle of EUC transport at 35°W point toward the uncertainties in determining a seasonal cycle of EUC transport near the western boundary from model simulations. But evidence from observations is still limited, as exemplified in case of the 35°W and near 23°W sections. *Katz et al.* [1981], using 22 sections taken between $33-25°$W during the Global Weather Experiment, found the highest

EUC transport during early March (based on a single section) and a secondary maximum during August. From an evaluation of the 8 FOCAL/SEQUAL[1] cruises at 23°W, *Hisard and Hénin* [1987] obtained maximum EUC transports during autumn, but time series of moored current meters at 28°W, 0° by *Weisberg et al.* [1987] during $1983 - 1985$ did not show a detectable seasonal cycle of EUC transport.

Surface velocity

Inspection of longitude-time diagrams of the zonal surface velocity, averaged between $\pm 2.5°$ in latitude, from the FLAME model and the drifter climatology by *Lumpkin and Garzoli* [2005] (Figure 4.3) yields good agreement concerning the periods of maximum westward velocities during April to July and during November to December. But besides, there are remarkable differences regarding periods of weakest westward or even eastward velocities particularly in the region east of 5°E. The drifter climatology reveals slightly westward velocities west of about 0° during both January to March and August to October, with an eastward velocity maximum between about $0 - 5°$E during the latter period. Otherwise, the model shows mainly eastward velocities during the first quarter of the year as well as to the east of about 4°W during August to October and largest velocities (≥ 20 cm/s) occur between about 4°W and 5°E during February and March. But note that despite these differences the longitudinal averaged seasonal cycle from the FLAME model fits generally in the error margins of the drifter climatology.

Cold tongue

In this study, the simulated near-surface temperature in 15 m depth is chosen instead of SST because of the applied Haney-type surface heat flux relaxation [*Haney*, 1971]. The modeled SST will therefore be constrained to be close to the climatological SST and, in particular, interannual SST variability is significantly affected. However, near-surface temperature anomalies are derived here by removing the respective seasonal cycle of the 13-year model simulation at each grid point and Figure 4.4 shows a time series of the near-surface temperature anomaly within the cold tongue region 20°W - 5°E, 6°S - 2°N in comparison with a corresponding time series of the NOAA OI SST data set. Overall, the agreement between the two time series is reasonable ($r = 0.52$), with largest differences occuring in

[1] Programme Français Océan et Climat dans l'Atlantique Equatorial/Seasonal Response of the Equatorial Atlantic

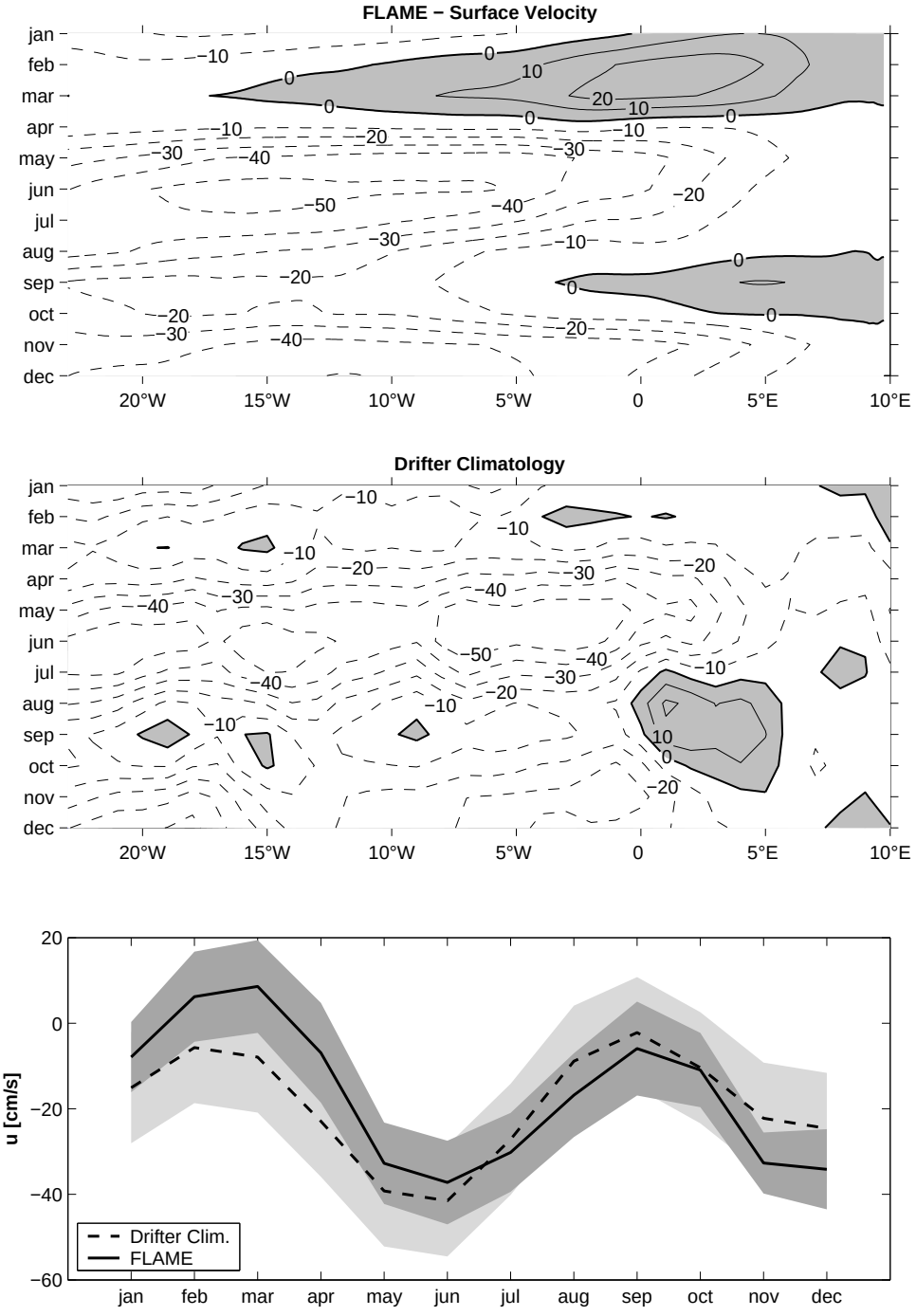

Figure 4.3: Longitude-time diagrams of the annual mean zonal surface velocity [contour interval is 10 cm/s], averaged between ±2.5° in latitude, from FLAME (upper panel) and the drifter climatology by *Lumpkin and Garzoli* [2005] (middle panel). Lower panel: corresponding longitudinal averaged seasonal cycles from FLAME (solid line), with standard deviation (dark gray shaded), and the drifter climatology (dashed line), with standard error (light gray shaded). [*Hormann and Brandt*, 2007]

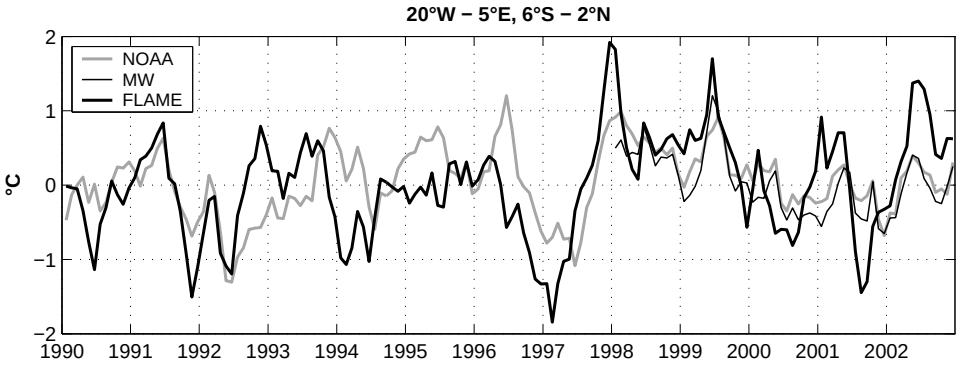

Figure 4.4: Time series of 15m-temperature anomalies from FLAME (thick black line), NOAA (thick gray line) and Microwave (MW) OI SST anomalies (thin black line) [°C] within the box 20°W - 5°E, 6°S - 2°N. [*Hormann and Brandt*, 2007]

the mid-1990s. The additionally marked monthly anomaly values from the original daily Microwave OI SST data set give an idea of the uncertainties inherent in the observations.

4.2 Mean and seasonal cycle

Mean flow

In order to present a view of the EUC evolution in the eastern equatorial Atlantic, Figure 4.5 shows the annual mean zonal velocity distributions at 10°W and 3°E from the FLAME model. In comparison to the 23°W section (Figure 4.1, lower left panel), the EUC has significantly weakened at 10°W. Above $\sigma_\theta = 26.8\,\mathrm{kg/m^3}$ the EUC transports only 9.2 Sv eastward and the velocity of its core, still located slightly south of the equator at about 50 m depth, has reduced to about 65 cm/s compared to 80 cm/s at 23°W. But note that contrary to the above discussed 23°W section, the EUC is found here nearly completely below $\sigma_\theta = 25.4\,\mathrm{kg/m^3}$. The aforementioned two branches of the SEC are again observable in the surface layer to either side of the EUC as well as the SEUC in the thermocline layer near the southern boundary of the section. In the surface layer to the north of about 2°N there are indications of the eastward Guinea Current. At 3°E, the overall circulation has largely weakened and the EUC transport has reduced to 2.3 Sv, only three quarters of the transport at 10°W.

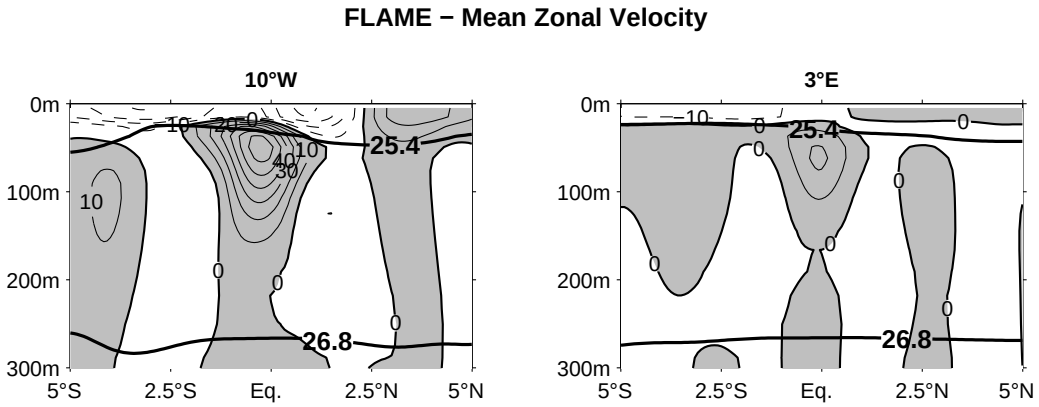

Figure 4.5: Annual mean zonal velocity [contour interval is 10 cm/s] at 10°W (left panel) and 3°E (right panel) from FLAME. Marked are isopycnals $\sigma_\theta = 25.4$ and $26.8\,\mathrm{kg/m^3}$ (thick solid lines). [*Hormann and Brandt*, 2007]

Seasonal cycle

Contrary to the afore discussed seasonal cycles of EUC transport that are calculated for a fixed depth range, isopycnal layers are considered here for the meridional sections at 23°W, 10°W and 3°E. Isopycnal layers are chosen because they follow the depth range of the thermocline better. The seasonal cycle of thermocline EUC transport is derived from eastward zonal velocities between ±2.5° in latitude and within the isopycnal range $\sigma_\theta = 25.4 - 26.8\,\mathrm{kg/m^3}$, whereas the seasonal cycle of total eastward transport is calculated between ±2.5° in latitude and above $\sigma_\theta = 26.8\,\mathrm{kg/m^3}$ (Figure 4.6). It is differentiated here between thermocline EUC transport and total eastward transport because of the presence of eastward surface currents, particularly in the eastern equatorial Atlantic during January to March (Figure 4.3, upper panel).

At 23°W, where a significant part of the EUC is found above $\sigma_\theta = 25.4\,\mathrm{kg/m^3}$ (Figure 4.1, lower left panel) and equatorial surface currents are usually westward (Figure 4.3, upper panel), the seasonal cycle of total eastward transport represents that of the EUC. In correspondence to Figure 4.2 (lower panel), the seasonal cycle of total eastward transport at 23°W is characterized by a maximum during September, a secondary maximum during April and minima during May/June and February. The seasonal cycle of thermocline EUC transport shows rather an annual cycle, with a maximum during August/September and a minimum during February. At 10°W, the seasonal cycles of thermocline EUC transport and total eastward transport are in close agreement except during February to April. The seasonal cycle of total eastward transport reveals maxima during September and March and minima during May and boreal winter. In agreement with the 23°W section, the seasonal cyle of thermocline EUC transport is characterized by a maximum during September

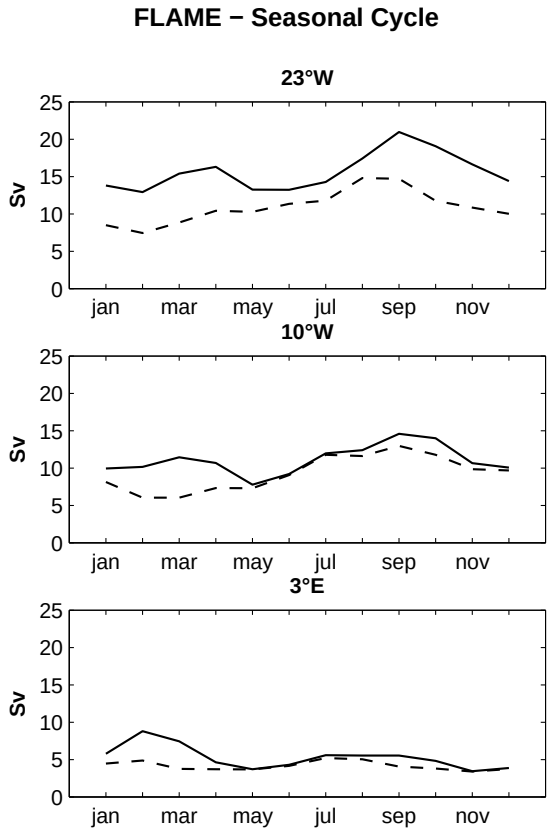

Figure 4.6: Seasonal cycle of thermocline EUC transport (dashed lines) and total eastward transport (solid lines) [Sv] at 23°W (upper panel), 10°W (middle panel) and 3°E (lower panel) from FLAME. Transports are calculated between ±2.5° in latitude and between $\sigma_\theta = 25.4 - 26.8\,\mathrm{kg/m^3}$ in case of the thermocline EUC transport and above $\sigma_\theta = 26.8\,\mathrm{kg/m^3}$ in case of the total eastward transport, respectively. [*Hormann and Brandt*, 2007]

and a minimum during February/March. Overall, the seasonal cycles of both isopycnal ranges are much diminished at 3°E. But weak thermocline EUC transport maxima during February and July as well as a pronounced total eastward transport maximum during February are observable.

The strong thermocline EUC transport reduction compared to the total eastward transport during boreal winter/spring at all three locations suggests that the boreal winter/spring maximum is rather due to an eastward flow in the surface layer than in the thermocline layer. This feature is in agreement with recent time series from moored ADCPs at 23°W, 0° revealing the EUC closer to the surface during January to May [*Provost et al.*, 2004; *Giarolla et al.*, 2005; *Brandt et al.*, 2006].

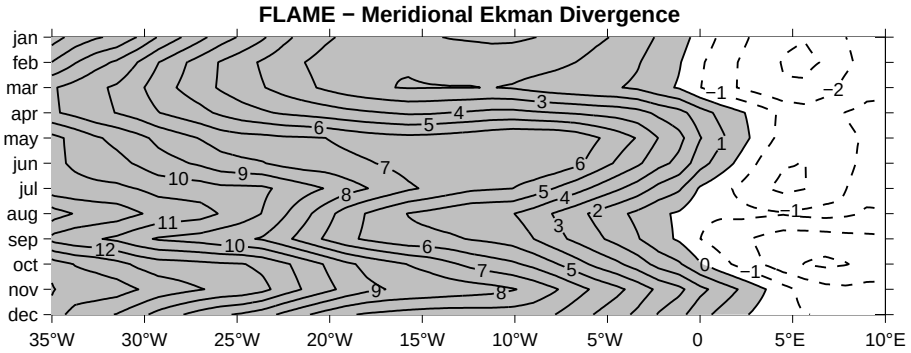

Figure 4.7: Longitude-time diagram of the meridional Ekman divergence between 2.5°N and S from FLAME. Contour interval is 1 m^2/s. [*Hormann and Brandt*, 2007]

Meridional Ekman divergence

In order to study the relation between the seasonal cycle of EUC transport and wind-induced equatorial upwelling, the meridional Ekman divergence between 2.5°N and S $\left(T_{ek}^{2.5°N} - T_{ek}^{2.5°S}\right)$ from the FLAME model is presented (Figure 4.7). The pattern can generally be described by divergences, associated with prevailing easterly winds, to the west of about 0° and convergences, due to an eastward wind stress component related to the low-pressure system on the African continent [*du Penhoat and Treguier*, 1985], farther east. While the meridional Ekman divergence maximum during November can be found throughout the equatorial Atlantic, there are regional differences concerning another maximum during boreal spring/summer. To the east of about 15°W, this maximum shows up during April to June whereas it appears between about $25 - 15$°W during July and farther west during August. In the central and eastern equatorial Atlantic, the meridional Ekman divergence is at minimum during August/September and February/March.

However, seasonal variations of the meridional Ekman divergence are rather dominated by an annual harmonic near the western boundary, whereas a prevailing semiannual signal is apparent in the central and eastern part of the basin [see *Philander and Pacanowski*, 1986a].

Obviously, the seasonal cycle of the meridional Ekman divergence is not simply related with the seasonal cycle of thermocline EUC transport, in particular due to a remote forcing of the EUC strength. The boreal summer/autumn maximum of the EUC is regarded as a near-equilibrium response to the equatorial easterly trades in the western and central Atlantic [e.g., *Philander and Pacanowski*, 1980, 1986a], and thus a correspondence between this EUC maximum and a maximum of the meridional Ekman divergence can be expected near the western boundary during boreal summer/autumn. During February/March, the meridional Ekman divergence minimum that is present throughout the equatorial Atlantic

coincides with the thermocline EUC transport minima at 23°W and 10°W as well as with the weak thermocline EUC transport maximum at 3°E. Favored by the eastward shoaling of the EUC, eastward wind stress anomalies drive directly surface and undercurrent layer in the easternmost part of the equatorial Atlantic.

Mean box budget

For the purpose of further examining the relation between horizontal transports and upwelling, in particular with regard to the EUC, Figure 4.8 (upper panel) shows an annual mean box budget of the central and eastern equatorial Atlantic calculated from the FLAME model. The boxes are defined by zonal sections at 2.5°N, 2.5°S, 7.5°S and 15°S as well as by meridional sections at 23°W, 10°W and 3°E, with section horizontal transports indicated for both thermocline and surface layer. These mean transports are derived by first calculating the respective transports for each time step and then averaging over the whole period. Upwelling across $\sigma_\theta = 25.4\,\mathrm{kg/m^3}$, which is generally below the mixed layer, results from the continuity of the corresponding section horizontal transports of the surface layer, i.e. horizontal transport divergences (convergences) lead to upwelling (downwelling).
At 23°W, the thermocline layer is characterized by a strong eastward inflow in the equatorial belt (5.9 Sv) due to the EUC and a reduction of the eastward flow toward the African coast. Associated with the eastward weakening of the thermocline flow along the equator, there is significant upwelling throughout the equatorial belt. In this region, the surface layer transports are predominantly characterized by a meridional divergence west of 10°W and a zonal divergence east of 10°W. This feature is also illustrated in Figure 4.8 (lower panel). While the total surface layer transport divergence is mainly determined by the zonal transport divergence from the eastern boundary up to about 10°W, the meridional transport divergence contributes significantly just to the west of about 10°W. The additionally depicted annual mean meridional Ekman divergence shows weak convergences to the east of 5°W, followed by a steep increase toward the west. As discussed by *McCreary and Lu* [1994], the meridional transport in the surface layer is given by the Ekman drift and the geostrophic transport [see *Schott et al.*, 2004]. The geostrophic transport always counteracts the Ekman transport which is the main reason for the difference between total surface layer transport divergence and meridional Ekman divergence. However, equatorial upwelling is most intense between 10°W and 3°E (1.5 Sv), coincident with strongest thermocline EUC transport reduction (4.3 vs. 1.1 Sv). Although the eastward weakening of the EUC is in part also due to a southward transport in the thermocline layer across 2.5°S, a significant part of the EUC supplies the equatorial upwelling. The adjacent southern belt reveals also eastward transports in the thermocline layer, here attributed to the SEUC, as

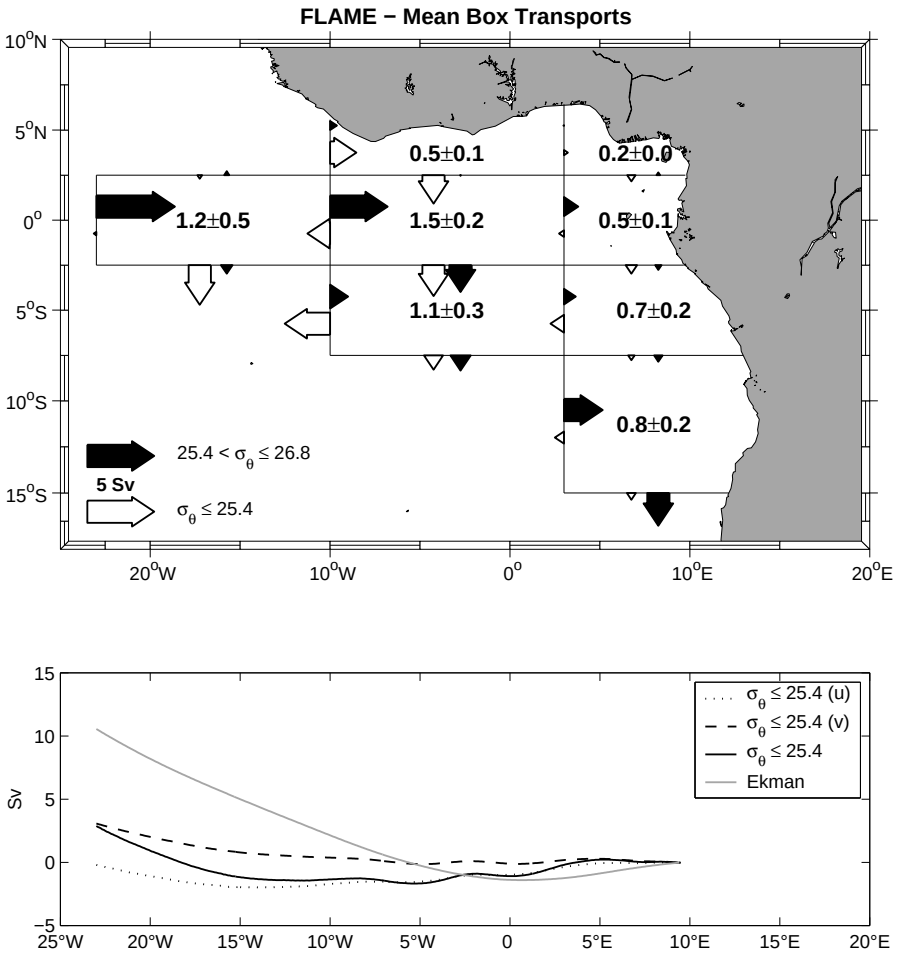

Figure 4.8: Upper panel: Annual mean transports [Sv] across box boundaries from FLAME for thermocline [$\sigma_\theta = 25.4 - 26.8$ kg/m^3] (black arrows) and surface layer [$\sigma_\theta \leq 25.4$ kg/m^3] (white arrows), with scale indicated in the figure. Upwelling [Sv] across $\sigma_\theta = 25.4$ kg/m^3, with standard deviation, is marked in box centers, positive is upward. Lower panel: Annual mean zonal (black dotted line), meridional (black dashed line) and total (black solid line) surface layer transport divergence between 2.5°N and S as well as annual mean meridional Ekman divergence between 2.5°N and S (gray solid line) from FLAME. These transport values are cumulated westward starting at the African coast. [*Hormann and Brandt*, 2007]

well as westward transports above $\sigma_\theta = 25.4$ kg/m^3. As aforementioned, between 10°W and 3°E the EUC loses some transport toward the south and thus contributes partly to the strong upwelling (1.1 Sv) between $2.5 - 7.5$°S. But besides, the SEUC is also of importance considering the upwelling in this belt. The coastal upwelling south of 2.5°S is supplied by a weak southward flow out of the equatorial belt and eastward flow across 3°E. The southernmost box, located east of 3°E between $7.5 - 15$°S, indicates a cyclonic circulation in the thermocline layer as well as significant upwelling. These features can be associated

with the Angola Dome which center was reported at 5°E, 13°S by *Gordon and Bosley* [1991].
The annual mean box budget of the central and eastern equatorial Atlantic from the FLAME model suggests a partial supply of both equatorial and coastal upwelling by the EUC. In agreement with Figure 4.8 (upper panel), showing that the EUC transport loss between 23°W and 10°W is mainly due to equatorial upwelling, a former study of the tropical Atlantic's mean mass budget by *Philander and Pacanowski* [1986b] yielded that the EUC reduces its transport from 14.6 Sv across 30°W to 4.5 Sv across 10°W because of equatorial upwelling. *Philander and Pacanowski* [1986a] pointed out that the eastern equatorial Atlantic has a distinct semiannual cycle of upwelling and downwelling which is primarily associated with the divergence of the westward surface flow, not with the divergence of the meridional Ekman drift [*Philander and Pacanowski*, 1986b]. Similarly, *Verstraete* [1992] noted that neither the meridional Ekman divergence at the equator nor the coastal Ekman divergence due to alongshore winds can explain a significant part of the upwelling in the Gulf of Guinea. A concomitant analysis of thermocline water masses indicated a supply of the coastal upwelling by the EUC. *Hazeleger and de Vries* [2003] studied the fate of water masses in the Atlantic EUC using a global 1/4° ocean model and determined sites where water masses from the EUC upwell and later downwell by analyzing Lagrangian trajectories. In the model study by *Hazeleger and de Vries* [2003], most of the EUC water upwells in the equatorial region, even though other upwelling sites are found close to the African continent.

4.3 Interannual variability

Boreal summer cold tongue variability

In order to further investigate the relation between zonal advection and equatorial upwelling in the Atlantic cold tongue region, the focus is here on the period from June to August (JJA) when the cold tongue is most pronounced. Considering the mean June-July-August average of the near-surface temperature from the FLAME model in the central and eastern equatorial Atlantic (Figure 4.9, left panel), a patch of low temperatures shows up within the region 20°W - 5°E, 6°S - 2°N [see *Xie and Carton*, 2004] and in correspondence, steric height values are also dropped in this region during boreal summer (Figure 4.9, right panel). For both quantities, cold tongue indices are derived by averaging the near-surface temperature and steric height anomalies of the 13-year model simulation during boreal summer over the specified region (Figure 4.10a, b). The resulting time series are highly

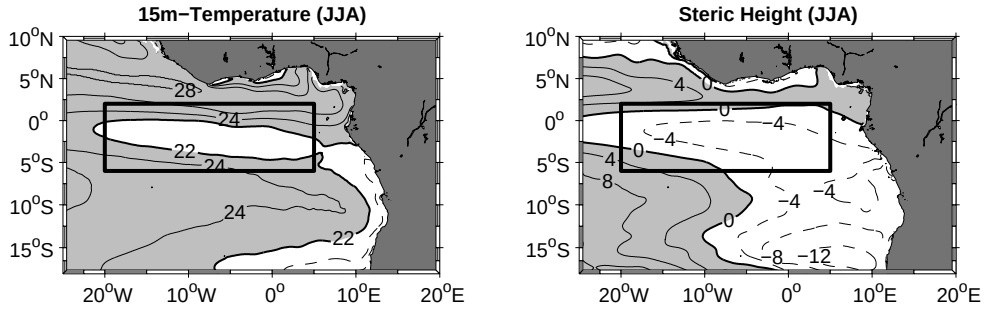

Figure 4.9: Mean June-July-August averages of 15m-temperature [contour interval is 2°C] (left panel) and steric height (relative to about 500 m) [contour interval is 4 cm] (right panel) from FLAME. Marked is the box 20°W - 5°E, 6°S - 2°N. [*Hormann and Brandt*, 2007]

correlated with each other ($r = 0.87$) and warm events occur generally in conjunction with positive steric height anomalies. Calculating comparable cold tongue indices from the NOAA OI SST and T/P sea surface anomaly data sets (Figure 4.10a, b) confirms the close link between both time series found in the model ($r = 0.84$). Overall, there is also a reasonable agreement of the respective extrema from the model and the observations, with largest differences in the mid-1990s (see Figure 4.4).

Figure 4.10c shows the June-July-August averages of the thermocline EUC transport anomalies, i.e. within the isopycnal range $\sigma_\theta = 25.4 - 26.8\,\mathrm{kg/m^3}$, at 35°W, 23°W and 10°W. While the two time series at 23°W and 10°W are significantly anticorrelated with both cold tongue indices from the model, correlation coefficients, in particular concerning the near-surface temperature-based cold tongue index, are lower regarding the thermocline EUC transport anomalies at 35°W (Table 4.2). Both simulated cold tongue indices are significantly correlated with the time series of the June-July-August average of equatorial zonal wind stress anomalies in the western and central Atlantic (Figure 4.10d). This wind time series is in turn anticorrelated with the time series of the thermocline EUC transport anomalies, i.e. stronger EUC under enhanced easterlies.

In order to further illustrate the relation between extreme events and thermocline EUC transport anomalies during boreal summer, Figure 4.11 presents the mean June-July-August equatorial zonal velocities, zonal velocity anomalies and potential temperature anomalies at 23°W and 10°W for three warm [1991, 1999, 2002] (cold [1990, 1992, 2001]) years occurring in conjunction with significantly reduced (enhanced) thermocline EUC transports. The warm and cold events are clearly captured by the temperature distributions, with anomalies generally more pronounced near the surface at 10°W. It is also apparent that the eastward EUC and the westward SEC north and south of the equator are weaker (stronger) during warm (cold) events. Largest anomalies are found above the

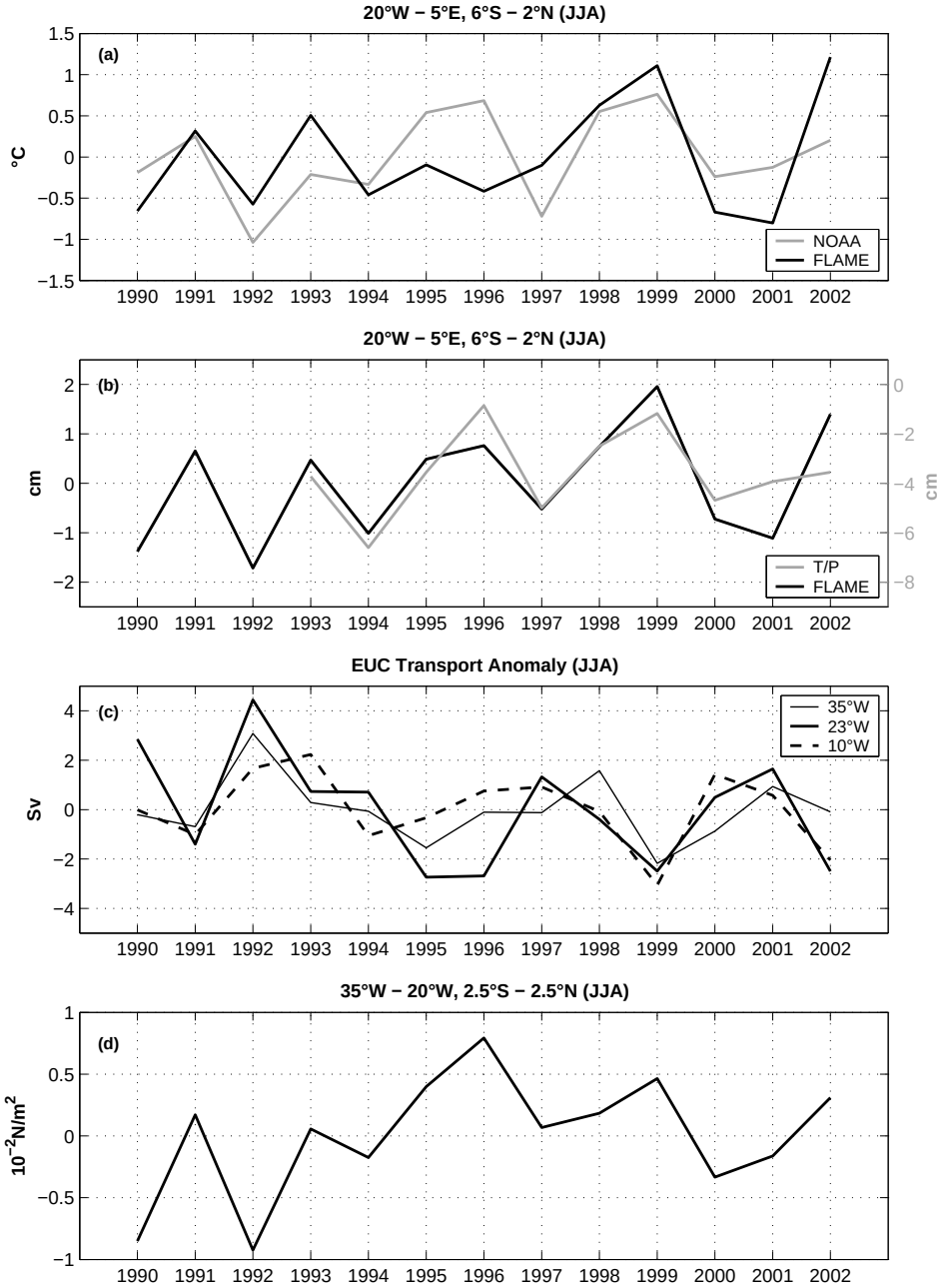

Figure 4.10: (a) June-July-August averages of 15m-temperature anomalies from FLAME (black line) and NOAA OI SST anomalies (gray line) [°C] within the box 20°W - 5°E, 6°S - 2°N. (b) Same as (a), but for steric height anomalies (relative to about 500 m) from FLAME (black line) and T/P sea surface anomalies (gray line) [cm]. (c) June-July-August averages of thermocline EUC transport anomalies from FLAME [Sv] at 35°W (thin solid line), 23°W (thick solid line) and 10°W (thick dashed line). (d) June-July-August average of zonal wind stress anomalies from FLAME [10^{-2} N/m^2] within the box 35°W - 20°W, 2.5°S - 2.5°N. [*Hormann and Brandt*, 2007]

	$CTI_{\theta_{15m}}$	$CTI_{SH_{500m}}$
EUC, 35°W	-0.29	-0.53
EUC, 23°W	-0.59	-0.88
EUC, 10°W	-0.59	-0.58

Table 4.2: Correlation coefficients between cold tongue indices (CTI) and June-July-August thermocline EUC transport anomalies from FLAME at 35°W, 23°W and 10°W. 95%- and 99%-significance levels are 0.51 and 0.64, respectively. [*Hormann and Brandt*, 2007]

EUC core, i.e. mainly above $\sigma_\theta = 25.4\,\mathrm{kg/m^3}$, at 23°W extending up to the surface. Thus, westward surface velocities directly above the EUC core are enhanced (reduced) during warm (cold) events.

It has been shown here that during boreal summer positive (negative) near-surface temperature and steric height anomalies in the equatorial cold tongue region are linked with reduced (enhanced) thermocline EUC transports in the central and eastern Atlantic as well as weakened (increased) easterlies in the western and central part of the basin. Several studies [e.g., *Merle*, 1980; *Servain et al.*, 1982; *Zebiak*, 1993; *Ruiz-Barradas et al.*, 2000] already indicated that there is a link between SSTs in the east and surface winds in the west and *Góes and Wainer* [2003] showed that the upper-ocean circulation decreases (intensifies) during extreme warm (cold) years, with warm events usually occurring during July.

Role of equatorial waves

Inspection of the zonal velocity and temperature anomalies during warm and cold events showed generally largest anomalies within the surface layer (see Figure 4.11). Figure 4.12 (left panels) depicts transport anomalies of the 13-year model simulation after subtracting the mean seasonal cycle, calculated between ±2.5° in latitude and above $\sigma_\theta = 25.4\,\mathrm{kg/m^3}$ at 23°W and 10°W. The corresponding variance-conserving power spectra (Figure 4.12, right panels) reveal in both cases a spectral peak at a period of about 5 months, i.e. on intraseasonal time scales. Cross-correlation analyses are now carried out between these two transport time series and both near-surface temperature and steric height anomalies (Figures 4.13 and 4.14). Note that transports within the surface layer are enhanced (reduced) during warm (cold) events. The surface layer transports in the equatorial belt are generally dominated by the westward SEC that weakens (strengthens) during warm (cold) events, although westward surface velocities directly above the EUC core are enhanced (reduced) during warm (cold) events (Figure 4.11).

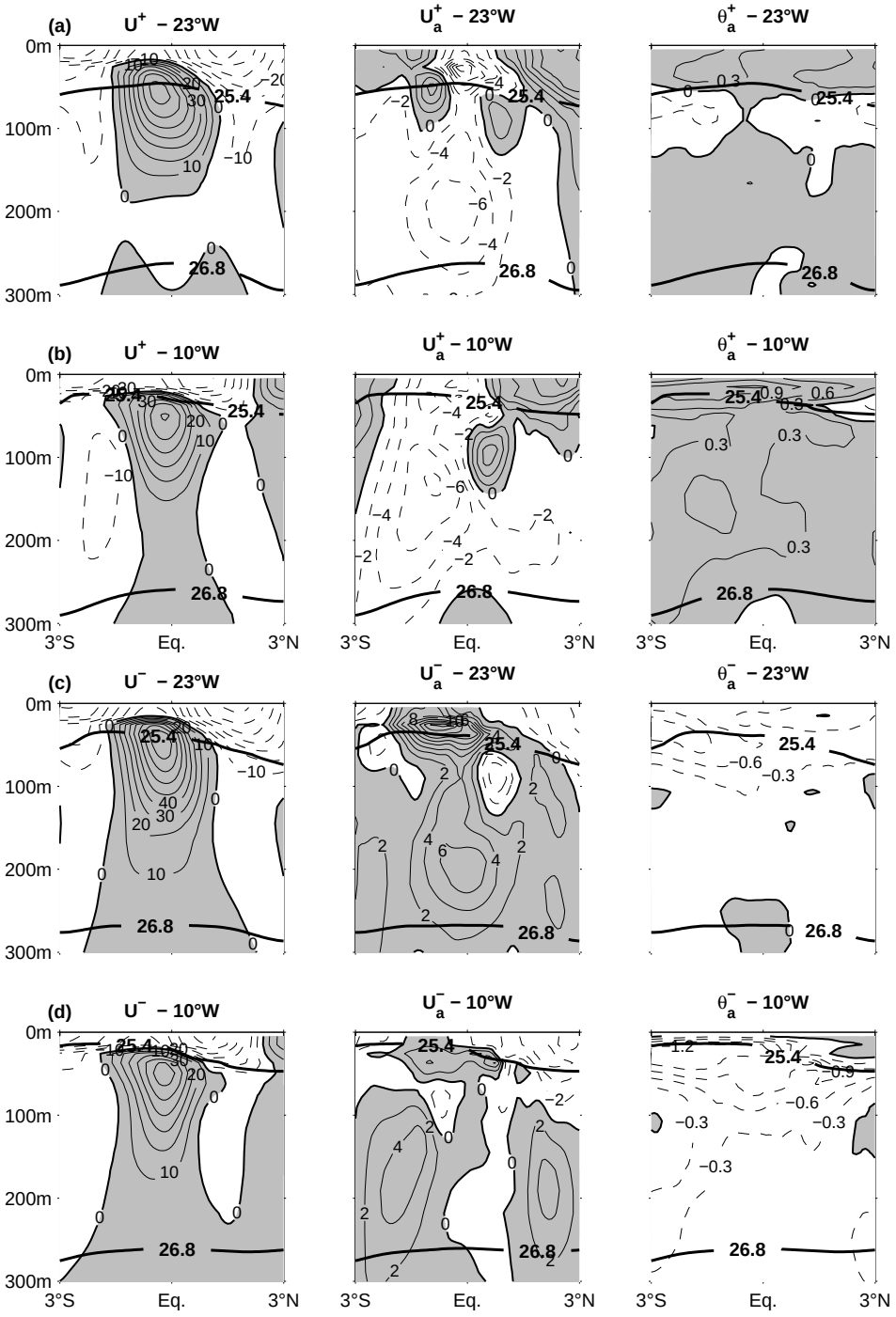

Figure 4.11: (a) Mean June-July-August zonal velocity [contour interval is 10 cm/s] (left panel), zonal velocity anomaly [contour interval is 2 cm/s] (middle panel) and potential temperature anomaly [contour interval is 0.3°C] (right panel) during 3 warm years (1991, 1999, 2002) at 23°W from FLAME. (b) Same as (a), but for 10°W. (c) Same as (a), but for 3 cold years (1990, 1992, 2001). (d) Same as (c), but for 10°W. [*Hormann and Brandt*, 2007]

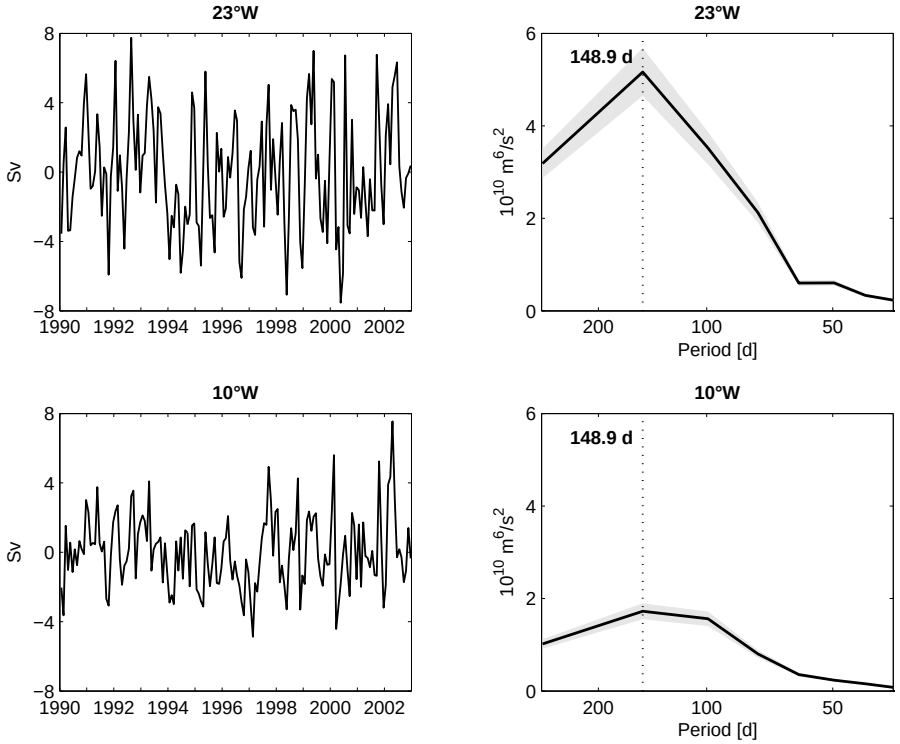

Figure 4.12: Left panels: Transport anomalies between ±2.5° in latitude and above $\sigma_\theta = 25.4\,\mathrm{kg/m^3}$ at 23°W (upper panel) and 10°W (lower panel) from FLAME. Right panels: Corresponding variance-conserving power spectra, with 95%-confidence interval (shaded). [*Hormann and Brandt*, 2007]

The cross-correlation of the transport anomalies at 23°W and 10°W with near-surface temperature anomalies in the central and eastern equatorial Atlantic (Figure 4.13, left panels) reveals high correlations (up to 0.7) in the near-equatorial region to the west of 10°W in the cases of both sections. Focusing on the 10°W section, somewhat weaker correlations are also found in the near-equatorial region to the east of 10°W as well as in coastal regions south of the equator. The examination of the corresponding cross-correlations between the transport anomalies and steric height anomalies (Figure 4.13, right panels) shows significant correlations along the equator up to the African coast. Along the coast, the signal can be traced up to 10°N and 18°S, respectively. This pattern is more pronounced regarding the 10°W section, particularly in the easternmost part of the basin.

Considering the corresponding cross-correlation time scales (Figure 4.14), an eastward phase propagation along the equator, indicative of the presence of equatorial Kelvin waves, can be found. Note that the time scales are somewhat different: Near-surface temperature anomalies react slower to surface layer transport anomalies than steric height anomalies. This can be explained by considering the propagation of downwelling/upwelling equatorial Kelvin waves. The deepening and shallowing of the isopycnals associated with these waves

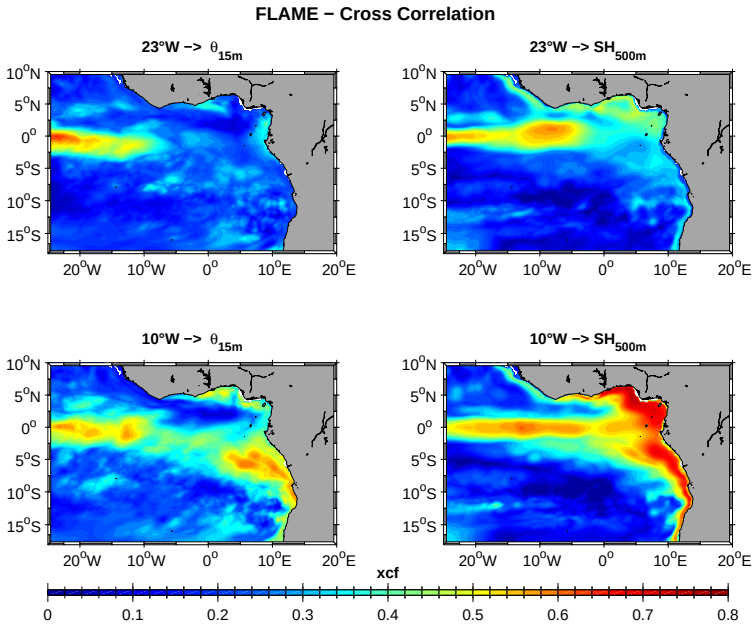

Figure 4.13: Cross-correlation of transport anomalies, calculated between ±2.5° in latitude and above $\sigma_\theta = 25.4\,\mathrm{kg/m^3}$, at 23°W (upper panels) and 10°W (lower panels) with 15m-temperature (left panels) and steric height anomalies (relative to about 500 m) (right panels) in the central and eastern equatorial Atlantic from FLAME (95%-confidence interval is 0.16). [*Hormann and Brandt*, 2007]

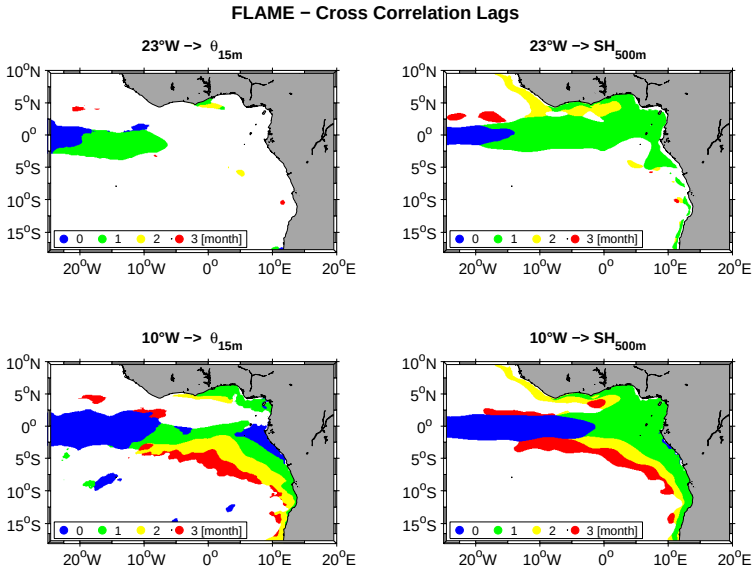

Figure 4.14: Cross-correlation lags [month] corresponding to Figure 4.13, shown only for cross-correlations ≥ 2· 95%-upper confidence bound and lags ≥ 0. [*Hormann and Brandt*, 2007]

act in different ways: While the steric height relative to a fixed depth (here about 500 m) is increased (reduced) in case of deeper (shallower) isopycnals, the near-surface temperature is more indirectly affected by vertical mixing leading to a reduced (increased) downward heat flux at the base of the mixed layer in case of deeper (shallower) isopycnals.
At the African coast, there are as well differences between the two quantities. In case of the steric height anomalies, the signal bifurcates into two poleward branches along the coast and a separation from the coast as well as an associated westward phase propagation can be found between about $2-5°$N and S. The correlation between the 10°W surface layer transport anomalies and the near-surface temperature anomalies shows only a westward phase propagation south of the equator whereas the northern counterpart is missing.
The cross-correlation analyses suggest a significant relation between equatorial transport anomalies within the surface layer in the central and eastern Atlantic and both near-surface temperature and steric height anomalies in the equatorial and coastal upwelling regions. These findings are also confirmed by a corresponding coherence analysis at a period of about 5 months (not shown) where both transport time series show their energy maxima (see Figure 4.12, right panels).

4.4 Summary and discussion

The 1/12° FLAME model of the Atlantic Ocean was used here to study the EUC and associated cold tongue variability. It was shown that the FLAME model is generally in line with mean zonal velocity sections derived from shipboard observations at 35°W and near 23°W, with mean EUC transports of 19.2 and 13.7 Sv compared to 19.9 and 14.0 Sv from the observations. Considering the aspect of different vertical mixing parameterizations, FLAME was also compared to the SPFLAME run. While significant differences emerged at 35°W concerning the mean zonal velocity distribution and seasonal cycle of EUC transport, a general agreement was found at 23°W. Large discrepancies concerning the seasonal cycle of EUC transport at 35°W were also obtained by *Hüttl and Böning* [2006] using model simulations with different horizontal resolutions. Studying the seasonal variability of deep currents in the equatorial Atlantic, *Böning and Kröger* [2005] stated that in contrast to the zonal flow patterns in the interior the recirculation patterns near the western boundary appear sensitive to model resolution and parameterization choices. However, due to the limited number of observations, a clear seasonal cycle of EUC transport based on cross-equatorial ship sections is still not derivable.
A clear eastward weakening of the simulated FLAME EUC is apparent throughout the

equatorial Atlantic. The seasonal cycle of total eastward transport is generally characterized by two distinct maxima, one during boreal summer/autumn and another during boreal winter/spring, but only the boreal summer/autumn maximum is found concerning the thermocline EUC transport. In the easternmost part of the equatorial Atlantic there is additionally a weak boreal winter/spring maximum in the thermocline layer that corresponds to an Ekman divergence minimum, and a forcing by local eastward wind stress anomalies is suggested.

The simulation of the equatorial upper-layer currents, particularly the EUC, depends strongly on the parameterization of the vertical mixing of momentum [*Pacanowski and Philander*, 1981; *Wacongne*, 1989; *Blanke and Delecluse*, 1993]. Differences in the representation of the surface mixed layer were suspected to be a main reason for variations in the strength and eastward penetration of the EUC in the DYNAMO models [*Dynamo Group*, 1997]. The strong sensitivity of the simulated EUC to the vertical viscosity was confirmed by *Böning and Kröger* [2005, Figure 2] considering several test runs with different parameterizations of the near-surface vertical mixing. Nevertheless, the simulated eastward weakening of the EUC, in particular in the eastern equatorial Atlantic, is consistent with several observations in this region [e.g., *Hénin et al.*, 1986; *Hisard and Hénin*, 1987; *Gouriou and Reverdin*, 1992; *Bourlès et al.*, 2002; *Mercier et al.*, 2003]. This weakening of the EUC was explained as closely related to thermocline shoaling, equatorial upwelling and enhanced vertical mixing [*Wacongne*, 1989; *Peterson and Stramma*, 1991; *Gouriou and Reverdin*, 1992].

While the boreal summer/autumn maximum is a common and well-understood feature of the Atlantic EUC, regarded as a near-equilibrium response to the equatorial easterly trades in the western and central part of the basin [e.g., *Philander and Pacanowski*, 1980, 1986a], the causes of the boreal winter/spring maximum are less evident. In particular, different mechanisms seem to be at play in the easternmost part of the equatorial Atlantic and the regions to the west. The study by *Arhan et al.* [2006], showing the secondary EUC transport maximum most pronounced near the western boundary, suggested remote forcing by the low-latitude rotational wind component as well as supply from the western boundary currents. *Hisard and Hénin* [1987] observed a much more rapid eastward weakening of the EUC around 4°W during summer and autumn than during winter and spring and a survey of the subsurface salinity maximum associated with the EUC core suggested also a deeper penetration of the EUC in the Gulf of Guinea during the latter two seasons. In this context, the seasonal migration of the zonal wind reversal in the Gulf of Guinea is believed to be of importance. The zonal winds in the Gulf of Guinea change from easterly to westerly near 4°W in the annual mean, but this reversal migrates westward with the northward movement of the ITCZ. It is expected that the associated reversal of the zonal pressure gradient migrates with the wind reversal, leading to an earlier termination of the

EUC during boreal summer and autumn [*Philander and Pacanowski*, 1986a; *Hisard and Hénin*, 1987].

The annual mean upwelling in the central and eastern equatorial Atlantic is found to be supplied by the EUC, but the SEUC contributes as well. In the equatorial belt, the surface layer transports are predominantly characterized by a meridional divergence west of 10°W and a zonal divergence east of 10°W.

As a major contribution of the present study, a significant anticorrelation between EUC transport anomalies in the central and eastern equatorial Atlantic and both near-surface temperature and steric height anomalies in the cold tongue region is found during boreal summer. The derived cold tongue indices are also linked with equatorial zonal wind stress anomalies in the western and central part of the Atlantic basin, i.e. positive (negative) near-surface temperature and steric height anomalies in the equatorial cold tongue region occur in conjunction with weakened (enhanced) easterlies to the west. Consequently and in agreement with the dynamics of the EUC, the EUC is reduced (enhanced) while the winds relax (intensify).

In order to investigate the existence and seasonality of a coupled variability similar to ENSO in the equatorial Atlantic, a recent study by *Keenlyside and Latif* [2007] discussed the individual components of the Bjerknes feedback in the Atlantic. They concluded that a weak Bjerknes feedback exists in the Atlantic, only active during boreal spring and summer. The Bjerknes feedback which may be established on a time scale of one to two months can amplify SST anomalies in the cold tongue region. These findings are confirmed by the here performed analysis of the cold tongue season. Warm events are generally found to occur in conjunction with relaxed easterlies to the west of the equatorial cold tongue which in turn are linked with reduced EUC transports. Thus, the supply of cold thermocline waters to the equatorial upwelling regions weakens leading to a further warming of the cold tongue. In the Pacific, a pronounced variability of the EUC is known to occur in association with El Niño, including a complete shutoff of the EUC during the largest events [*Johnson et al.*, 2002; *Izumo*, 2005].

Another main point here are the results of the cross-correlation analyses between equatorial transport anomalies above $\sigma_\theta = 25.4\,\mathrm{kg/m^3}$ at 23°W and 10°W, with a spectral peak at a period of about 5 months, and both near-surface temperature and steric height anomalies in the central and eastern Atlantic. Significant correlations are found in the equatorial and coastal upwelling regions and the corresponding cross-correlation time scales point at an eastward phase propagation along the equator toward the African coast where the signal bifurcates into two poleward branches along the coast. A separation from the coast and an associated westward phase propagation are found between $2 - 5$°N and S. This propagation pattern suggests the presence of equatorial waves. The linear equatorial wave reflection theory indicates that an eastward propagating equatorial Kelvin wave imping-

ing on a meridional east coast would be reflected into symmetrical westward propagating Rossby waves and coastal Kelvin waves [*Moore and Philander*, 1977]. In consistency with these theoretical considerations, *França et al.* [2003] yielded a significant lag correlation between Kelvin and first meridional mode Rossby waves near the African coast from altimetry.

Model studies suggest different mechanisms creating SST anomalies in the cold tongue region, among them are air-sea fluxes and subsurface processes as well as horizontal temperature advection [*Peter et al.*, 2006]. Of particular importance for the mixed layer heat budget seem to be the dynamics associated with TIWs as shown by *Jochum and Murtugudde* [2006]. However, observational data are up to now not sufficient enough to close the mixed layer heat budget in the cold tongue region especially on interannual time scales.

In the present study, the Atlantic EUC and associated cold tongue variability were analyzed using the high-resolution FLAME model. While the available cross-equatorial ship sections are very useful for determining the mean flow and possibly also the seasonal cycle of EUC transport, simulated interannual EUC transport variability can only be verified by moored observations mainly due to the large intraseasonal variability that is typically not captured by shipboard measurements.

5. Upper equatorial Atlantic variability during 2002 and 2005

The model results in Section 4.3 showed that equatorial waves are of importance for the Atlantic cold tongue region and the objective here is to investigate the upper equatorial Atlantic variability associated with equatorial Kelvin waves within the context of the interannual boreal summer variability from observations.
Substantial progress in the description of equatorial waves from observations has been made with the availability of altimeter measurements: First attempts to fit meridional equatorial wave modes to altimetric SSH data took place in the Pacific to investigate the ENSO phenomenon [e.g., *Delcroix et al.*, 1991]. In the Atlantic, equatorial waves and their seasonal time scales have been described at an early stage from altimeter measurements [e.g., *Arnault et al.*, 1992] while their interannual time scales have only more recently been established by *França et al.* [2003].

5.1 Interannual boreal summer variability

Surface conditions

The interannual boreal summer SST variability in the eastern Atlantic cold tongue and the corresponding zonal wind stress variability in the western and central part of the basin are presented in terms of June-July-August averages over the respective regions (Figure 5.1; see Section 4.3). In general, warm (cold) events in the east are linked with reduced (increased) easterlies toward the west which is in good agreement with previous studies [e.g., *Servain et al.*, 1982; *Zebiak*, 1993]. The focus is here on the warm year 2002 and the cold year 2005 when concomitant moored velocity observations are available.

Figure 5.2 illustrates the evolution of the different surface conditions prevailing during

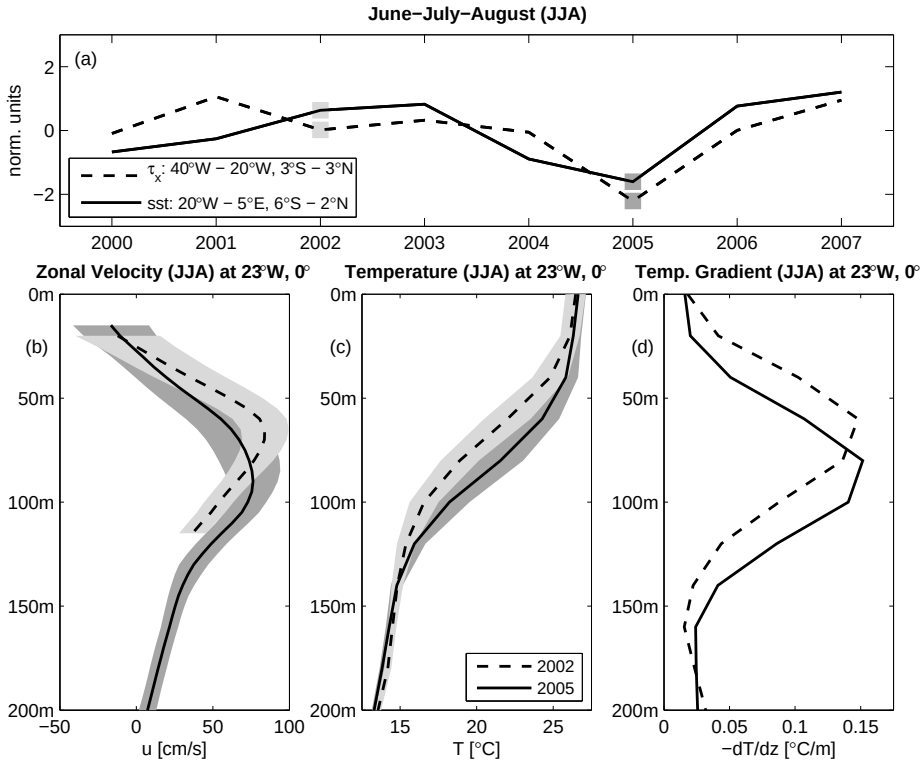

Figure 5.1: (a) June-July-August averages of SST over the region 20°W - 5°E, 6°S - 2°N (solid) and zonal wind stress over the region 40°W - 20°W, 3°S - 3°N (dashed); normalized by standard deviation. Marked are the years 2002 and 2005. (b) Mean June-July-August zonal velocity [cm/s] at 23°W, 0°, with standard deviation (shaded), during 2002 (dashed line, light gray shading) and 2005 (solid line, dark gray shading); mean flow calculated by subtracting annual and semiannual harmonics. (c) Same as (b), but for temperature [°C] at 23°W, 0°. (d) Temperature gradient [°C/m] corresponding to (c).[*Hormann and Brandt*, 2008]

these events: In boreal spring 2002, large positive SST anomalies[1] (up to 2°C) appear in the eastern cold tongue region while the corresponding pattern during 2005 resembles that of a dipole, with cold (warm) SST anomalies south (north) of the equator [see *Foltz and McPhaden*, 2006, Figure 2b]. Considering the respective wind stress fields, reduced (enhanced) easterlies are found in the western and central part of the basin during 2002 (2005). The easterlies are then around normal conditions in this region during boreal summer 2002, but still enhanced in 2005. Compared to the boreal spring situation, SST anomalies in the cold tongue region are reduced (enhanced) during boreal summer 2002 (2005) and a strong cooling of up to 2°C is now observable in 2005. During boreal fall,

[1] **Note:** Anomalies, as hereinafter referred to, are computed by subtracting the mean plus annual and semiannual harmonics of both the respective satellite and (as far as available) mooring data for the period end-August 2001 to December 2006.

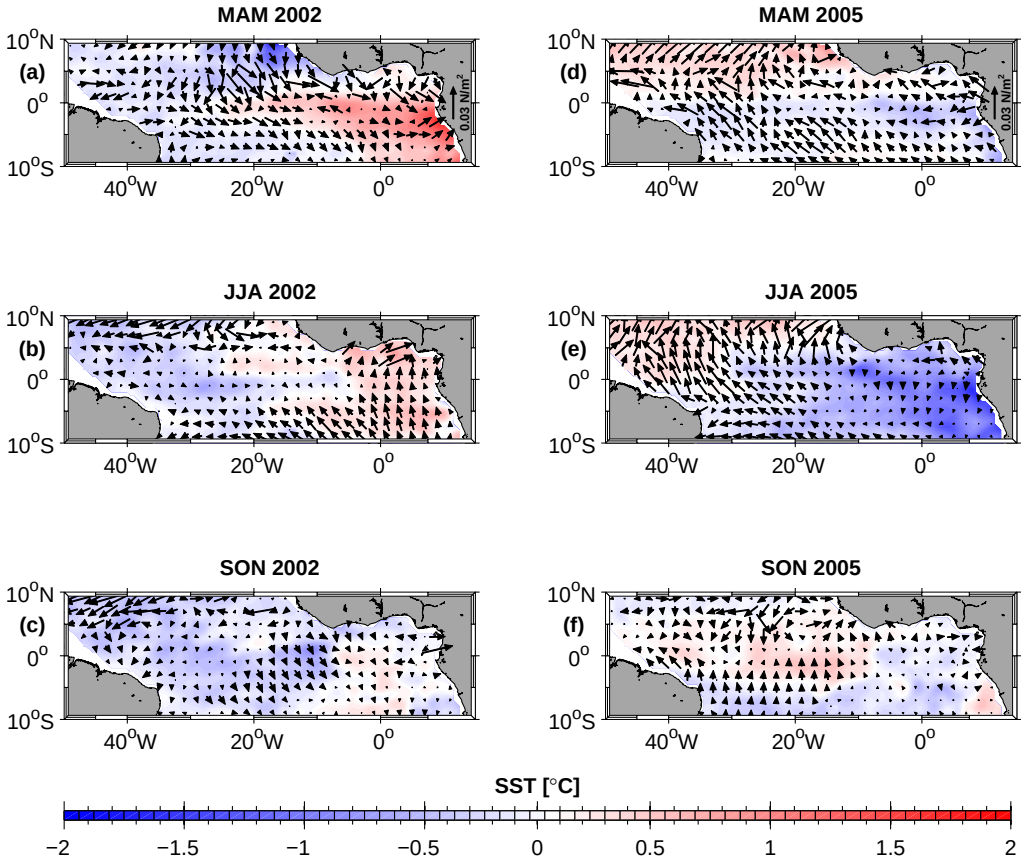

Figure 5.2: (a, c) March-April-May [MAM], (b, e) June-July-August [JJA] and (c, f) September-October-November [SON] averages of SST anomalies [°C; color coded] and zonal wind stress anomalies [N/m^2; vectors, with scale indicated in (a) and (c)] for the years 2002 (a - c) and 2005 (d - f). [*Hormann and Brandt*, 2008]

anomalies are generally small for both years.
However, the evolution of the surface conditions points to a possible relation between the meridional and zonal mode during 2005 as first suggested by *Servain et al.* [1999]. Although the northern hemisphere was on the whole anomalously cold during boreal spring 2002, the large zonal gradient of southern hemisphere SST anomalies is here not characteristic for the meridional mode.

Moored observations

In order to illustrate the subsurface differences between 2002 and 2005, mean boreal summer profiles at the equator, 23°W are calculated from the moored observations (Figure 5.1b-d).

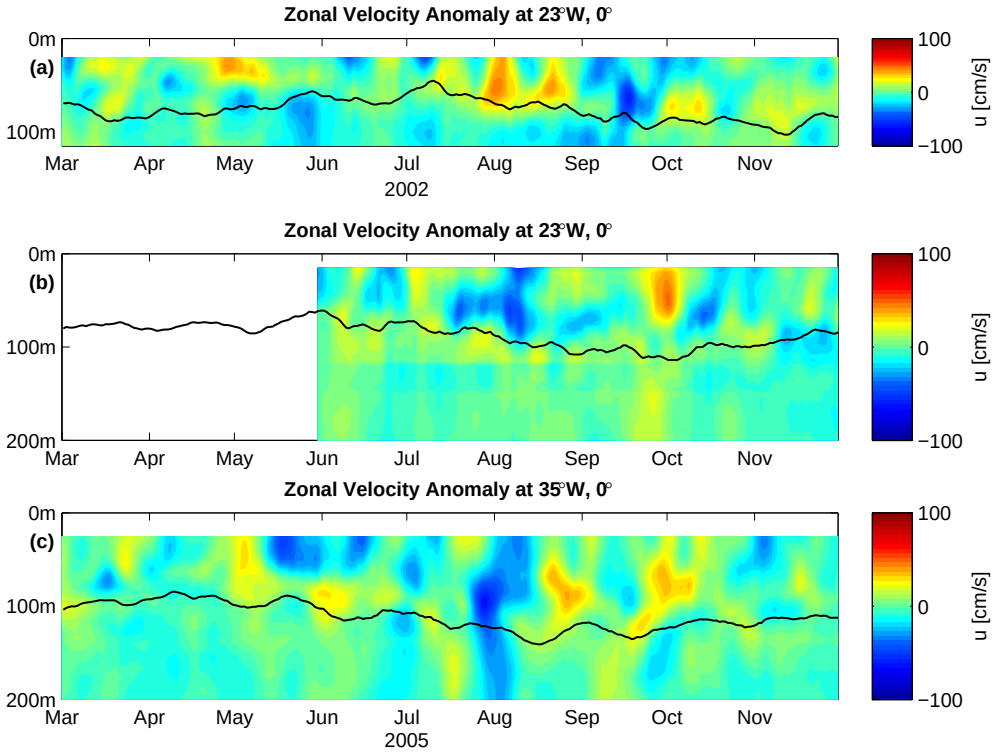

Figure 5.3: (a) Zonal velocity anomalies [cm/s] at 23°W, 0° from March to November 2002, with marked 20°C-isotherm depth (black line) to indicate thermocline depth. (b) Same as (a), but for 2005. (c) Same as (b), but at 35°W, 0°. Data are smoothed by 7-day running mean. [*Hormann and Brandt*, 2008]

The mean boreal summer zonal velocitiy profiles reveal a somewhat stronger and shallower EUC core in 2002 (84 ± 16 cm/s, 65 m) than in 2005 (76 ± 16 cm/s, 90 m). Additionally, the mean boreal summer temperature profiles reveal a deepening of the isotherms in the depth range $40 - 120$ m during 2005 compared to 2002. Considering the associated vertical temperature gradients, the EUC is found to be embedded in a shallower (deeper) thermocline during 2002 (2005).

The observed differences are also obvious as regards the corresponding zonal velocity anomalies from March to November. Using the depth of the 20°C-isotherm as an indicator for thermocline depth, positive anomalies prevail above the shallow thermocline during boreal summer 2002 (Figure 5.3a) while largely negative values are found above the deeper thermocline during boreal summer 2005 (Figure 5.3b). In contrast to 23°W, where anomalies are most pronounced above the thermocline, distinct negative zonal velocity anomalies are observable down to 200 m depth at 35°W during boreal summer 2005 (Figure 5.3c). Basically, the shallowing (deepening) of the EUC core during warm (cold) events is consistent with the dynamics of the EUC driven by the eastward zonal pressure gradient force

[e.g., *Philander and Pacanowski*, 1986a; *Wacongne*, 1989]. The observations are also in general agreement with the model study by *Góes and Wainer* [2003] as well as with the results presented in Section 4.3 revealing a shallower (deeper) structure of the EUC during warm (cold) events. The oceanic adjustment to changes in the wind (responsible for setting up the zonal pressure gradient) involves the presence of wind-driven waves [e.g., *Cane and Sarachik*, 1976, 1977; *Moore and Philander*, 1977; *Philander and Pacanowski*, 1986a]. A recent study by *Han et al.* [2008] showed that equatorial Kelvin waves dominated sea level and thermocline variability throughout the equatorial Atlantic during boreal spring 2002. In the following, these waves are further investigated with respect to the observed differences in the upper equatorial Atlantic oceanic conditions during 2002 and 2005.

5.2 Equatorial Kelvin waves

Moored observations

In order to document the presence of equatorial Kelvin waves during both the warm event in 2002 and the strong cold event in 2005, the available moored 20°C-isotherm depth (Figure 5.4a, d) and dynamic height anomalies (Figure 5.4b, e) at 35°W, 0° and 23°W, 0° are considered for the respective March to November periods. These time series are found to be highly correlated (correlation coefficient [*cc*] ~ 0.9, with 95%-significance level of 0.13) at both locations during 2002 and 2005.
Besides, reasonable correlations are found between 20°C-isotherm depth anomalies and EUC core depth anomalies ($cc = 0.54/0.38$ at 23°W, 0° during March/June to November 2002/2005 and $cc = 0.47$ at 35°W, 0° during March to November 2005), and dynamic heights are closely related to SSHs at the two mooring sites (not shown).
As stated by *Rebert et al.* [1985] for the tropical Pacific, dynamic height and sea level fluctuations agree only in those areas where the thermal structure resembles a two-layer system very well and sea level fluctuations were as well observed to be a good measure of thermocline depth variations.
Cold tongue SSH and SST anomalies are also well correlated with each other during 2002 ($cc = 0.72$, 95%-significance level is 0.22), with positive anomalies prevailing around mid-May related to the warm event (Figure 5.4c). During 2005, the correlation of the two variables drops to 0.50 and large discrepancies are found from mid-May to mid-July when SST anomalies are strongest negative (Figure 5.4f).
França et al. [2003] already noted a partial lack of correspondence between SSH and SST anomalies in the equatorial region. The propagation of equatorial Kelvin waves from the

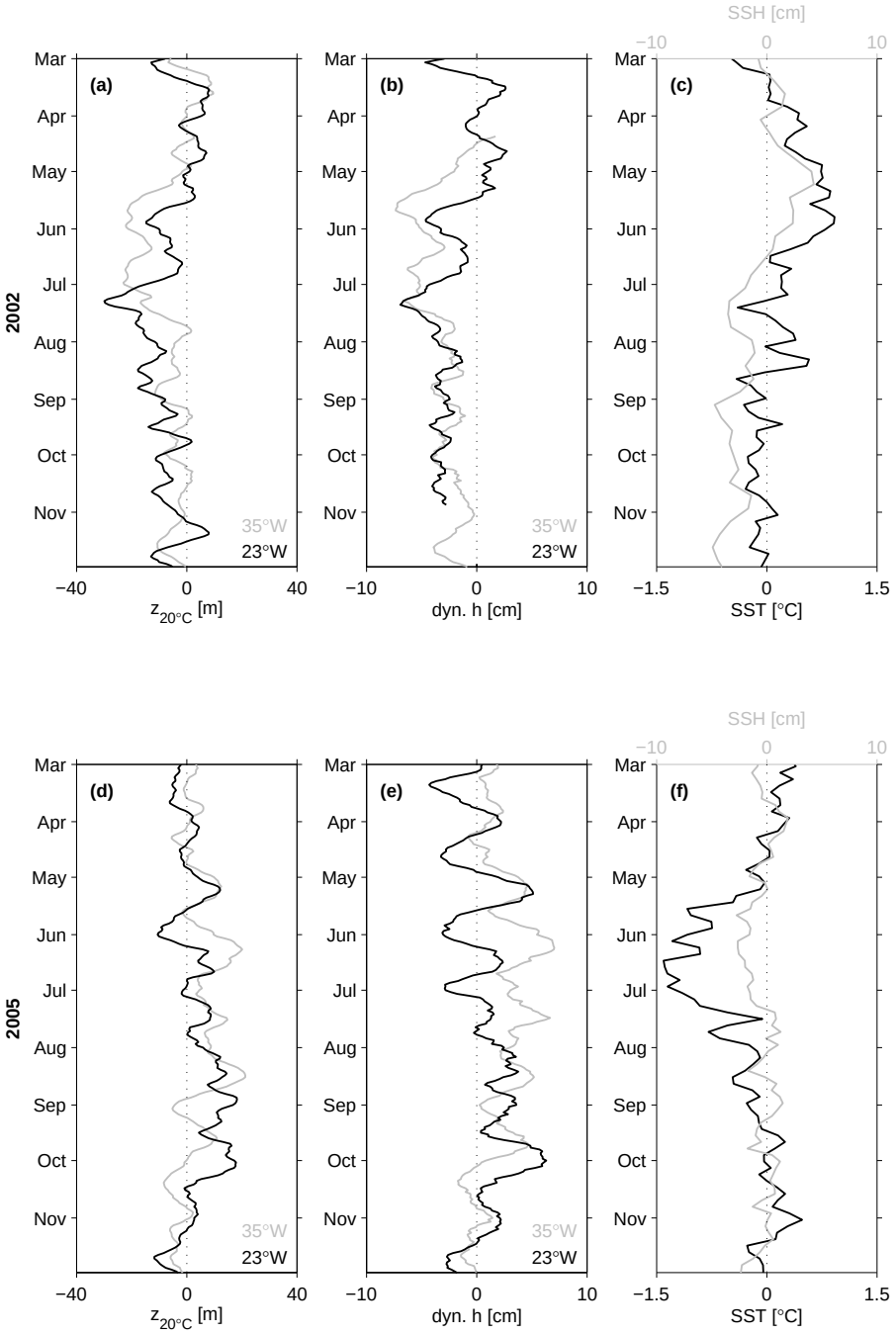

Figure 5.4: (a) Time series of 20°C-isotherm depth anomalies at 35°W, 0° [m; gray] and 23°W, 0° [m; black] from March to November 2002; positive values indicate deeper thermocline. Data are smoothed by 7-day running mean. (b) Same as (a), but for dynamic height anomalies [cm]. (c) Time series of SSH [cm; gray] and SST [°C; black] anomalies averaged over the region 20°W - 5°E, 6°S - 2°N from March to November 2002. (d - f) Same as (a - c), but for 2005. [*Hormann and Brandt*, 2008]

year (Mar. - Nov.)	variable	correlation	lag	phase velocity
2002	$z_{20°C}$	0.62	12 d	1.3 m/s
2002	dyn. h	0.58	11 d	1.4 m/s
2005	$z_{20°C}$	0.47	10 d	1.5 m/s
2005	dyn. h	0.38	7 d	2.2 m/s

Table 5.1: Maximum lagged correlation coefficients and corresponding lags of equatorial 20°C-isotherm depth anomalies ($z_{20°C}$) and dynamic height anomalies (dyn. h) at 35°W, 0° with their respective counterparts at 23°W, 0° (according to the time series shown in Figure 5.4a, b and d, e); 95%-significance level is 0.13. Also given are estimated phase velocities (see text for details). [*Hormann and Brandt*, 2008]

	35°W, 0°	∼ 23°W, 0°
1. baroclinic mode	2.5 m/s	2.4 m/s
2. baroclinic mode	1.5 m/s	1.4 m/s
3. baroclinic mode	1.0 m/s	0.9 m/s

Table 5.2: Theoretical phase velocities of the first three baroclinic modes as estimated from a vertical mode decomposition at 35°W, 0° and near 23°W, 0° (see text for details). [*Hormann and Brandt*, 2008]

western basin into the eastern basin could be followed in the SSH data, but not in the SST data. As the SSHs can mainly be attributed to dynamical effects, the observed differences between SSH and SST in the cold tongue region during boreal summer 2005 suggest that the influence of ocean dynamics on SST might be of minor importance.

However, considering lagged correlations of the equatorial 20°C-isotherm depth anomalies and dynamic height anomalies at 35°W with their respective counterparts at 23°W (Table 5.1), significantly larger coefficients are obtained for 2002 than 2005. The lags (dt) of maximum correlation are then used to estimate corresponding phase velocities:

$$c = \frac{\mathrm{d}x}{\mathrm{d}t} \tag{5.1}$$

with dx here the distance between 35°W, 0° and 23°W, 0°. Apart from the 2005 - dynamic height case, where pronounced differences are obvious between the 35°W - and 23°W - time series and correlation is lowest ($cc = 0.38$), the calculated phase velocities are around 1.4 m/s eastward.

These estimates agree well with theoretical values of the second baroclinic equatorial Kelvin wave mode (Table 5.2) as derived from a vertical mode decomposition of the mean stratification at 35°W, 0° and near 23°W, 0° by use of the available ship sections at these locations

(see Table 2.1). Comparable values were also reported in recent studies by *Illig et al.* [2004, Table 1], *Schouten et al.* [2005] and *Han et al.* [2008, Table 1].

Basinwide characteristics

In order to investigate the equatorial Kelvin waves in a basinwide context, the available satellite observations of SSHs are now considered in detail. Figure 5.5 illustrates apparent eastward propagating SSH anomalies along the equator which are superimposed on a strong seasonal cycle [see e.g., *Arnault et al.*, 1992; *Schouten et al.*, 2005]. The SSH anomalies also mirror the general features of the boreal summer extreme events as shown in Figure 5.1a, with prevailing positive (negative) values in the cold tongue region during warm (cold) events [see e.g., *França et al.*, 2003].

The wind-driven characteristics of these eastward propagations are illustrated by performing a lagged correlation analysis between zonal wind stress anomalies in the west (Figure 5.6a, same wind region as in Figure 5.1a) and SSH anomalies in the entire equatorial basin. Significant positive maximum correlation coefficients are found along the equator from about 30°W toward the African coast and an eastward phase propagation along the equator is obvious (Figure 5.6b, c). The corresponding propagation velocity can be estimated to 1.6 m/s (see Equation 5.1) which is again close to the theoretical value of the second baroclinic Kelvin wave mode (see Table 5.2). As regards the equatorial region to the west of about 30°W where positive correlations are insignificant or negative correlations are present [see *Han et al.*, 2008], the SSH variability is here generally lower than in the regions farther east along the equator as well as northward and southward along the African coast (Figure 5.6d). High SSH variability at the western boundary and along 5°N is associated with the NBC retroflection/generation of NBC rings and the instability of the NECC [e.g., *Schouten et al.*, 2005; *von Schuckmann et al.*, 2008, Figure 1].

However, zonal wind stress anomalies in the west appear to play an important role in forcing equatorial Kelvin waves as was also most recently suggested by *Han et al.* [2008]. In addition, *Han et al.* [2008] noted a particularly strong correlation between zonal wind anomalies in the central-western equatorial basin and anomalous sea levels across the equatorial basin during 2002.

Kelvin wave fit

The equatorial SSH variability, strongly indicating the presence of equatorial Kelvin waves, will now be discussed in terms of the linear equatorial wave theory [*Matsuno*, 1966].

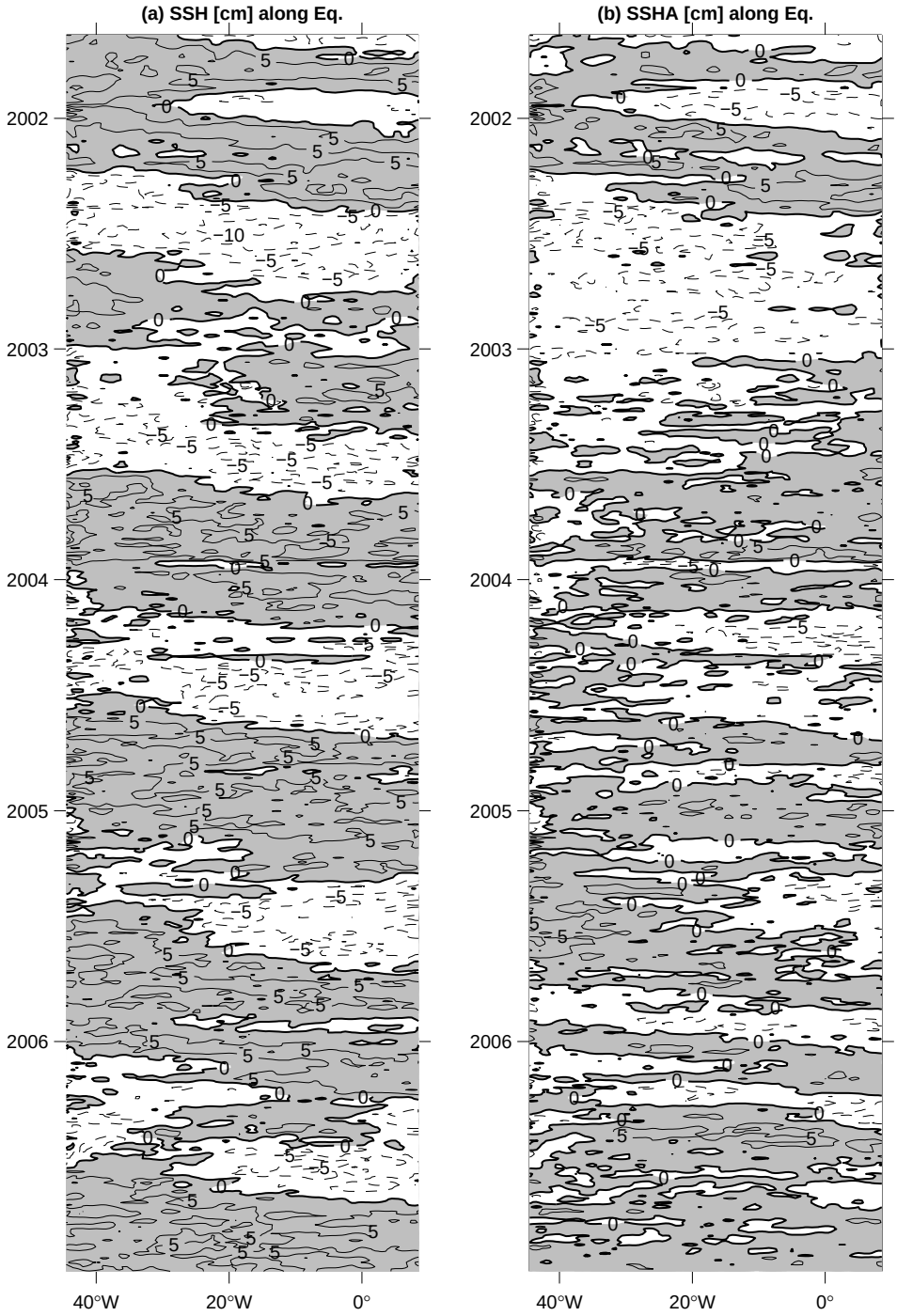

Figure 5.5: (a) SSH [cm] and (b) corresponding anomalies [cm] along the equator. Positive values are shaded gray and contour interval is 5 cm. [*Hormann and Brandt*, 2008]

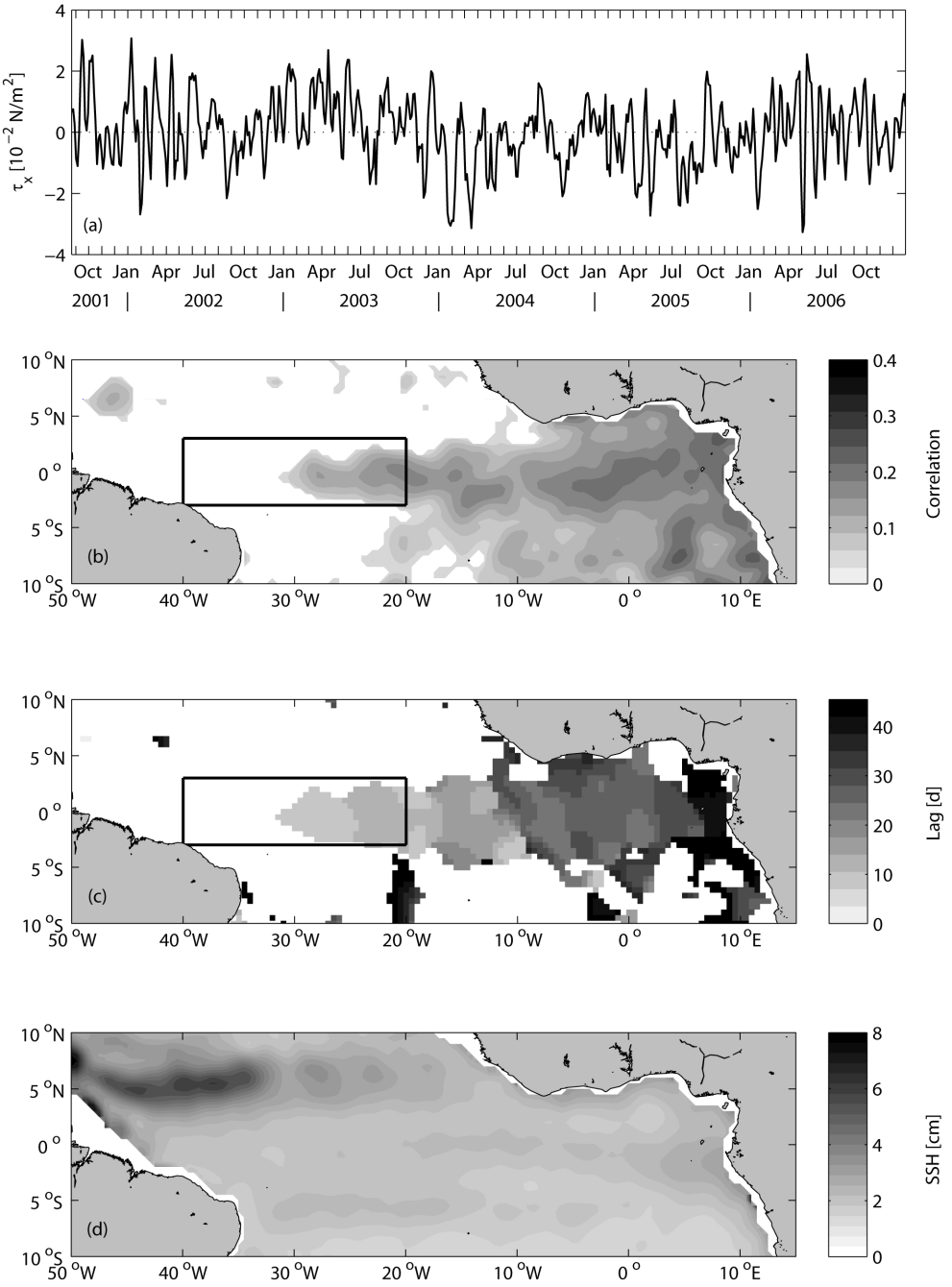

Figure 5.6: (a) Time series of zonal wind stress anomalies averaged over the region 40°W - 20°W, 3°S - 3°N. (b) Positive maximum lagged correlation coefficients above 95%-significance level [= 0.08] and (c) corresponding lags between the wind time series shown in (a), region is marked by the box, and equatorial Atlantic SSH anomalies. Anomalies are smoothed by 10.5-day running mean. (d) Standard deviation of equatorial Atlantic SSH anomalies. [*Hormann and Brandt*, 2008]

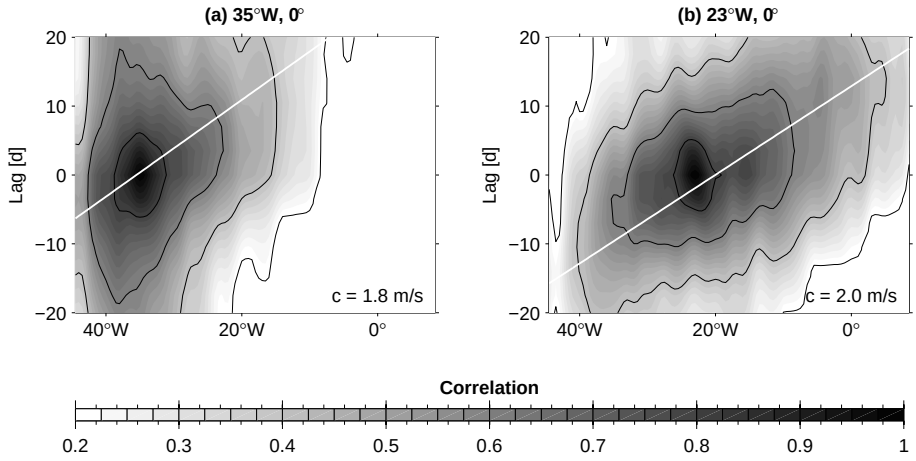

Figure 5.7: Lagged correlation analyses of SSH anomalies along the equator with (a) 35°W, 0° and (b) 23°W, 0° as reference longitudes. Contour interval is 0.2 (black) and white line corresponds to estimated phase velocity as given in the lower right-hand corner (see text for details). [*Hormann and Brandt*, 2008]

First, the phase velocitiy of the SSH anomalies along the equator for the period end-August 2001 to December 2006 is computed in a more rigorous manner by performing lagged correlation analyses as a function of longitudinal separation. 35°W and 23°W are chosen as reference longitudes and in each case a 2-dimensional polynomial fit in time is applied at all single longitudes along the equator for a better estimate of the linear slope through the points of maximum correlation. This slope is then used to finally calculate the respective phase velocities by taking only correlations greater or equal 0.2 into account (see Equation 5.1, Figure 5.7). The obtained values are 1.8 m/s for the 35°W - case and 2.0 m/s for the 23°W - case which are somewhat higher than the above estimates and fall within the range between the first and second baroclinic mode of equatorial Kelvin waves (see Table 5.2). These phase velocities are also in good agreement with previously reported values based on altimeter measurements [e.g., *Katz*, 1997; *França et al.*, 2003; *Han et al.*, 2008; *Polo et al.*, 2008].

Using an average phase velocity of c = 1.9 m/s, the equatorial Atlantic SSH anomalies are fitted in a least-square sense to the theoretical meridional (y) structure of equatorial Kelvin waves:

$$\eta(y) = \eta_0 \exp(-\beta y^2/2c) \tag{5.2}$$

with $\beta = 2.28 \times 10^{-11}$ m^{-1}s^{-1} (see Appendix A1). This fit accounts for up to 90% of the variance along the equator while explained variances decrease to about 60% at 3° and 20% at 5° in latitude, respectively (Figure 5.8). The structure function (Equation 5.2) that represents a mixture between first and second baroclinic mode waves is thus able to capture the dominant part of the equatorial Kelvin wave variability in the Atlantic.

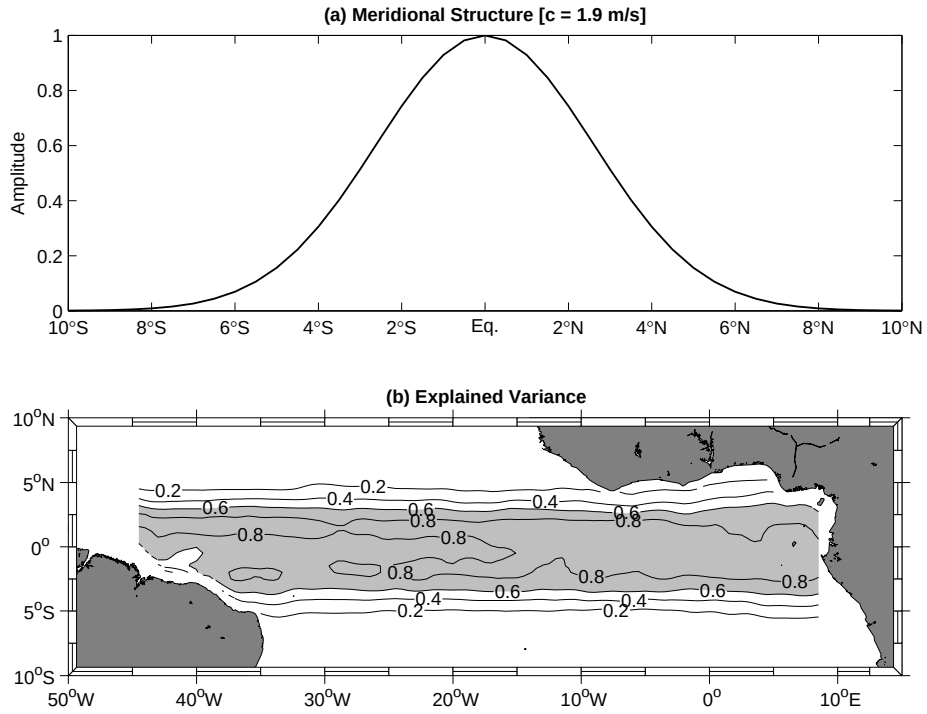

Figure 5.8: (a) Theoretical meridional structure of equatorial Kelvin waves according to Equation 5.2, with $\eta_0 = 1$ and c = 1.9 m/s. (b) Explained variances corresponding to the least-square fit of SSH anomalies in the equatorial Atlantic to the theoretical meridional structure of equatorial Kelvin waves. [*Hormann and Brandt*, 2008]

Equatorial Kelvin wave mode

The fitted SSH anomalies are then used to describe the equatorial Kelvin wave variability in terms of complex empirical orthogonal functions (CEOFs) [*Barnett*, 1983]. This technique is here more suitable than traditional EOF analysis because it is capable of detecting propagating features in space.

The 1. CEOF explains 50.1% of the variance along the equator, with spatial amplitude maxima in the central part of the basin and relative phase increasing from west to east (Figure 5.9c). This spatial phase distribution clearly indicates an eastward propagation along the equator as consistent with the equatorial Kelvin waves. Considering the corresponding temporal amplitudes, equatorial Kelvin waves appear to be exceptionally strong during 2002 (Figure 5.9a, b).

However, this mode shows a robust pattern of eastward propagating Kelvin waves along the equator and is adequate to describe their interannual variability in the equatorial region.

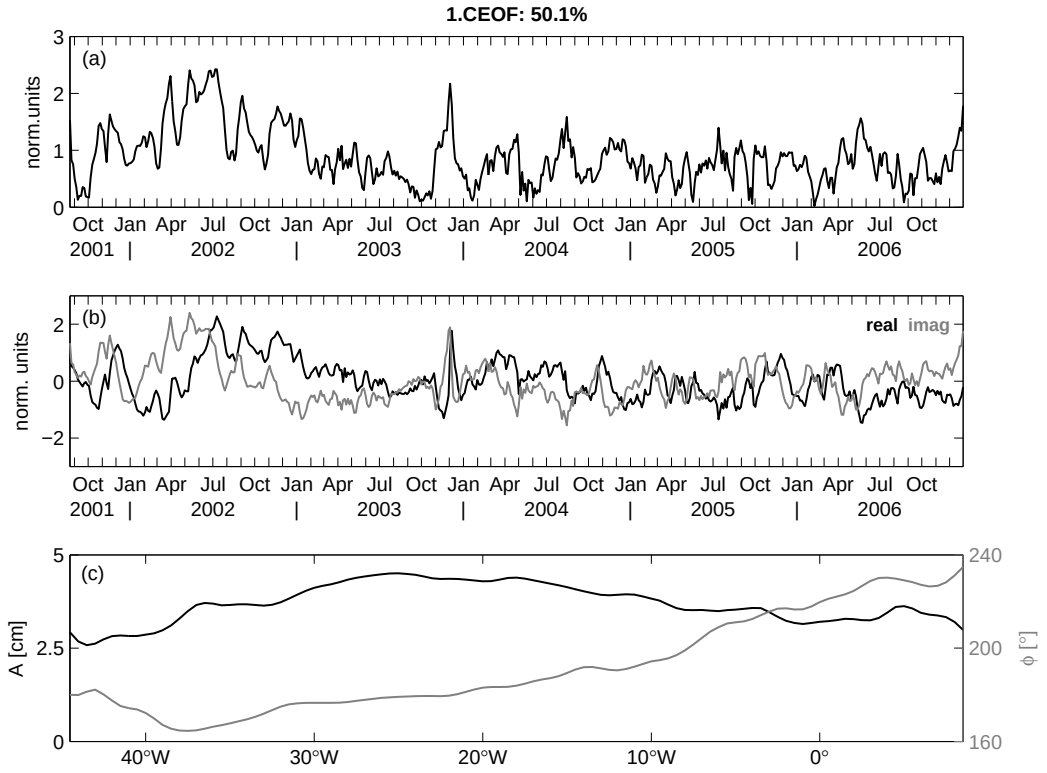

Figure 5.9: 1. CEOF of fitted SSH anomalies along the equator: (a) temporal amplitude, (b) corresponding real (black) and imaginary (gray) components [normalized units], and (c) spatial amplitude [cm; black] and relative phase [°; gray]. [*Hormann and Brandt*, 2008]

Regression analyses

The equatorial Kelvin wave mode, i.e. the real and imaginary temporal components (see Figure 5.9b), is taken as a basis to analyze related oceanic variations with respect to the observed differences during 2002 and 2005. In order to do so, linear regression analyses are carried out with both satellite and moored observations.

Satellite observations

The absolute regression map of SSH anomalies for the period end-August 2001 to December 2006 reproduces well the pattern of eastward propagating Kelvin waves along the equator, with largest amplitudes in the central equatorial Atlantic (Figure 5.10a). Remarkable dif-

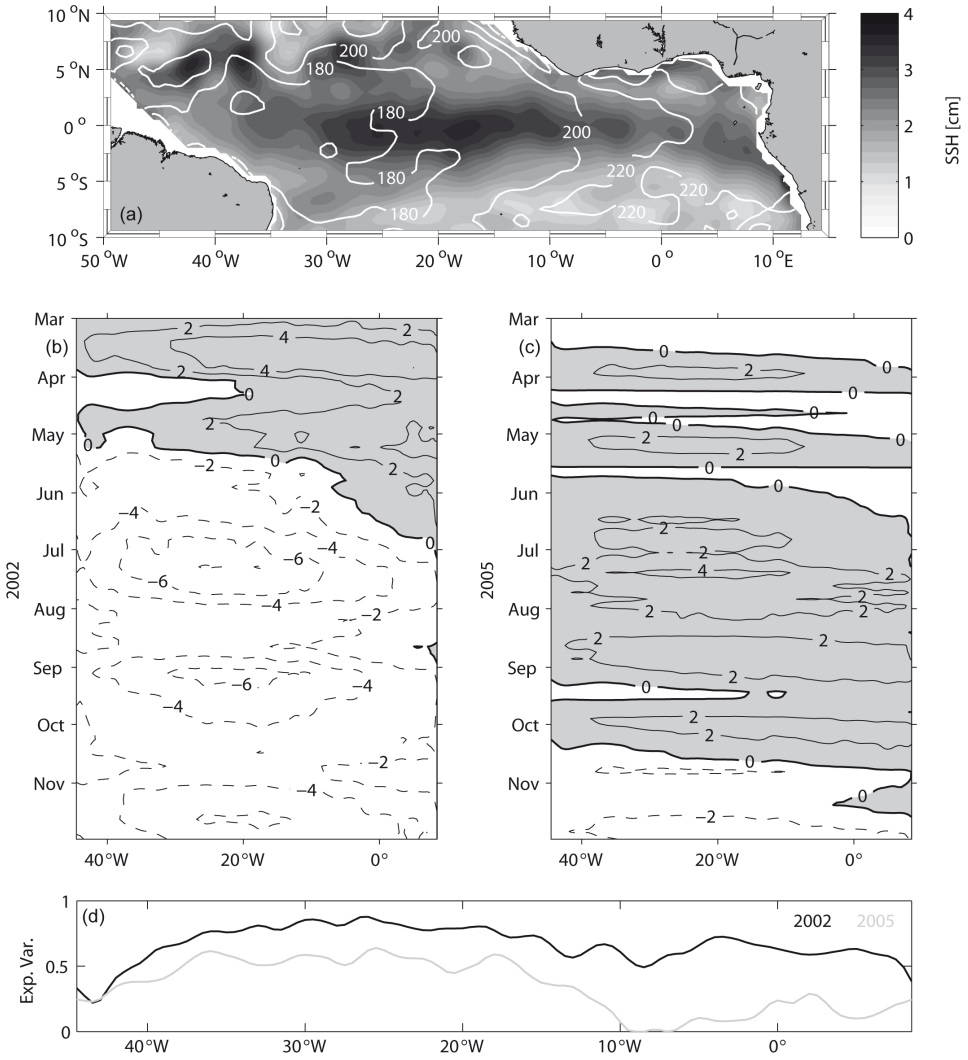

Figure 5.10: (a) Absolute regression map of SSH anomalies [cm] in the equatorial Atlantic onto the 1. CEOF real and imaginary temporal components (see Figure 5.9b), with superimposed relative phase contours [°]. (b, c) Corresponding regressed SSH anomalies [cm] along the equator for March to November 2002 (b) and 2005 (c); positive values are shaded gray and contour interval is 2 cm. (d) Explained variances according to (b, c) [2002: black, 2005: gray]. [*Hormann and Brandt*, 2008]

ferences become obvious when comparing the time series of regressed SSH anomalies along the equator from March to November 2002 and 2005. While positive (negative) anomalies prevail during boreal spring (summer and fall) 2002, weak positive anomalies are found from about mid-March to mid-October 2005 (Figure 5.10b, c).

The regression analysis accounts for about 80% and 55% of the variance in the central part of the basin during 2002 and 2005, respectively. Although somewhat lower values are also found in the eastern equatorial Atlantic during 2002, there is a substantial decrease to

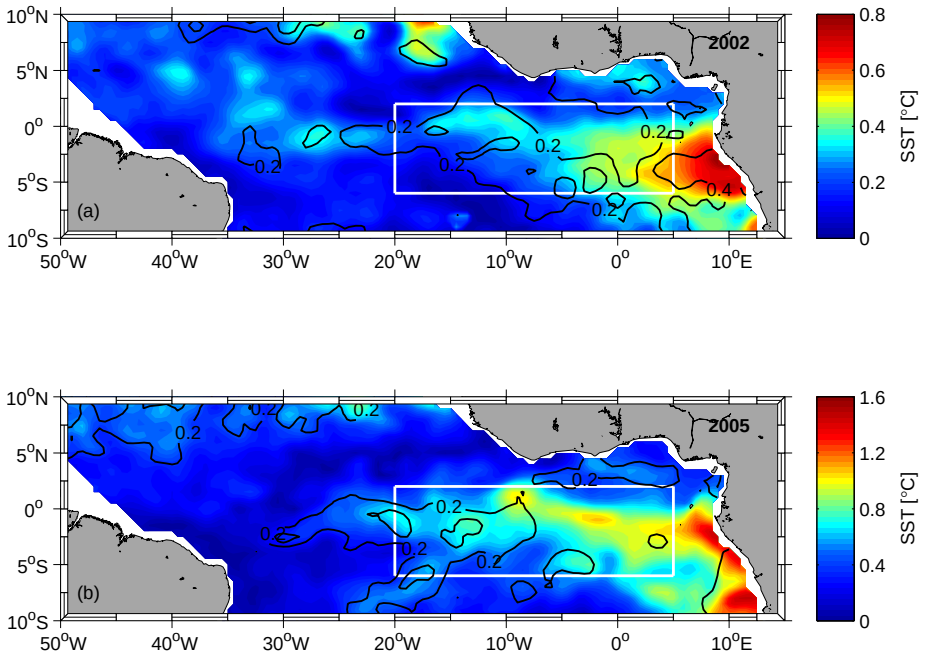

Figure 5.11: (a) Absolute regression map of SST anomalies [°C] in the equatorial Atlantic onto the 1. CEOF real and imaginary temporal components (see Figure 5.9b) for March to November 2002, with superimposed explained variances. (b) Same as (a), but for 2005. Note the different color scales for 2002 and 2005. White box marks cold tongue region. [*Hormann and Brandt*, 2008]

only about 15% of explained variance during 2005 (Figure 5.10d). This strong reduction confirms the previous suggestion that dynamic processes, i.e. the eastward propagation of equatorial Kelvin waves, might be of minor importance in the cold tongue region during boreal summer 2005.

Likewise, there are also differences in Kelvin wave related SST variability during 2002 and 2005. Figure 5.11 shows the respective March to November absolute regression maps of SST anomalies in the equatorial Atlantic, with generally larger values in the central and eastern part of the basin during 2005 (up to twice as much, note the different color scales in Figure 5.11). In the central equatorial Atlantic, where magnitudes are rather small compared to regions farther east, explained variances are in both cases between about $15 - 40\%$. In contrast, there is less agreement between both years in the eastern part of the cold tongue, with generally lower values of explained variance during 2005. These characteristics that are obtained from the co-variance between the equatorial Kelvin wave mode and SST also fit together on the one side with the observed strong cold tongue cooling during boreal summer 2005 (i.e., large amplitudes of SST anomalies) and on the other side, as above discussed, with the minor importance of equatorial Kelvin waves in the eastern equatorial Atlantic during that same year.

Additionally, maximum regression values are found in the eastern coastal regions south of the equator during both 2002 and 2005. But while the regression analysis accounts for about 40% of the variability in this region during 2002, again lower values are obtained for 2005. As indicated in Figure 5.10a, the equatorial Kelvin waves appear to propagate further along the African coast and can consequently contribute to the SST variability in the coastal upwelling regions. This continuing propagation as coastal Kelvin waves from the equator northward and southward along the African coast is studied in detail by *Polo et al.* [2008].

Moored observations

The subsurface oceanic variability during 2002 and 2005 co-varying with the equatorial Kelvin wave mode is now examined by using the available mooring data.

Basically, the regressed 20°C-isotherm depth anomalies at 35°W, 0° and 23°W, 0° (not shown) resemble the time series of regressed SSH anomalies during 2002 and 2005 (see Figure 5.10b, c). In order to point toward possible causes for the observed differences in the eastern equatorial Atlantic, corresponding regressed thermocline slope anomalies along the equator are considered here. The thermocline slope is computed as the difference between the moored 20°C-isotherm depths at 35°W and 23°W divided by the distance, with positive slope anomalies indicating an increased eastward thermocline rise compared to the mean state.

The regressed anomalies show negative thermocline slope anomalies from March to June 2002, a strong increase of the thermocline slope during June/July and positive thermocline slope anomalies afterwards. During 2005, the thermocline slope is increased (reduced) prior to (after) July 2005 (Figure 5.12a). As regards the regressed SST anomalies in the cold tongue region, positive (negative) values usually occur in correspondence with a(n) reduced (increased) thermocline slope. Note that while the observed evolution of cold tongue SST anomalies is generally captured by the regressed time series during 2002, the strong cooling during 2005 is not reproduced by the regression analysis (Figure 5.12b).

While the direct influence of equatorial Kelvin waves on SST variability in the cold tongue region is small, the anomalous reduced (increased) thermocline slope co-varying with the equatorial Kelvin wave mode prior to the cold tongue onset in 2002 (2005) appears to be favorable for the development of a warm (cold) event.

Considering now the zonal velocity anomalies at 23°W, 0° co-varying with the equatorial Kelvin wave mode, both the overall regression amplitude ($\sim$ 6.5 cm/s) and corresponding explained variance ($\sim$ 20%) are largest at 110 m depth with a secondary maximum near

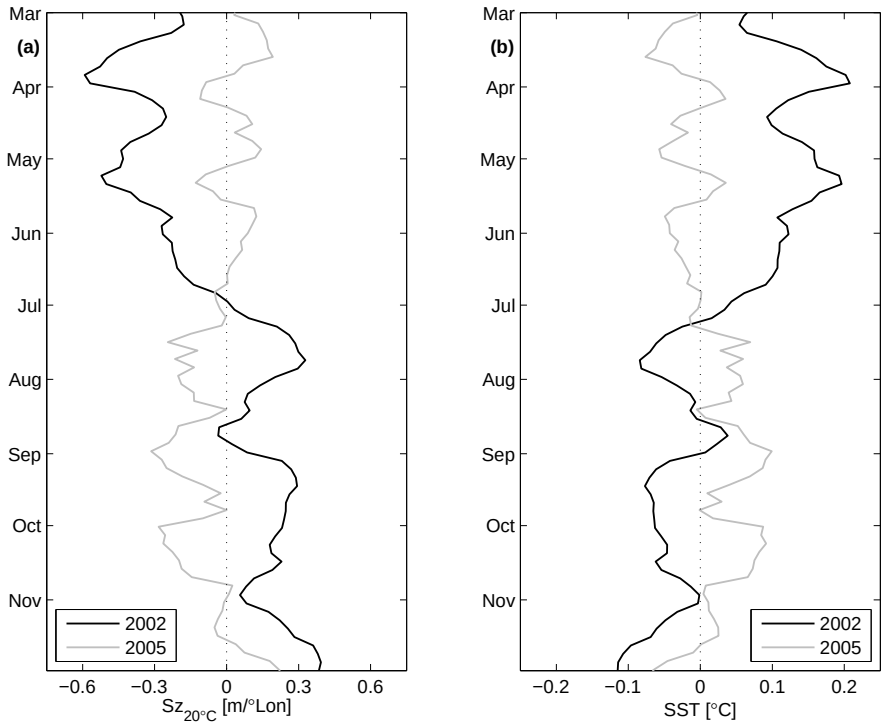

Figure 5.12: (a) Regressed thermocline slopes, with the 1. CEOF real and imaginary temporal components taken as a basis (see Figure 5.9b), from March to November 2002 (black) and 2005 (gray); positive slope anomalies indicate an increased eastward thermocline rise (see text for details). (b) Same as (a), but for regressed SST anomalies averaged over the cold tongue region 20°W - 5°E, 6°S - 2°N. [*Hormann and Brandt*, 2008]

the surface (Figure 5.13a). Figure 5.13b presents variance-conserving power spectra of 30 m - and 110 m - zonal velocities at 23°W, 0° and generally higher power is found for the near-surface current. Besides the strong spectral peaks in 30 m - zonal velocities at periods of about 7 and 25 days that are extensively discussed by e.g. *Grodsky et al.* [2005] and *Bunge et al.* [2007] for the first current meter mooring deployment period during 2002 and the latter one related to TIWs, enhanced power is also observable at a period of about 60 days. This 60 - day variability is as well present in the 110 m - zonal velocities, here of equal magnitude as the 25 - day peak, and *Han et al.* [2008] attributed the dominant spectral peak at 40 - 60 days during 2002/03 mainly to first and second baroclinic equatorial Kelvin wave modes.

In order to further illustrate the effect of equatorial Kelvin waves on 23°W - zonal velocity anomalies at the equator, a lagged correlation analysis is performed with respect to SSH anomalies all along the equator (Figure 5.13c, d). Both the primary and secondary maximum of the regression analysis (Figure 5.13a) are here well reproduced and maximum

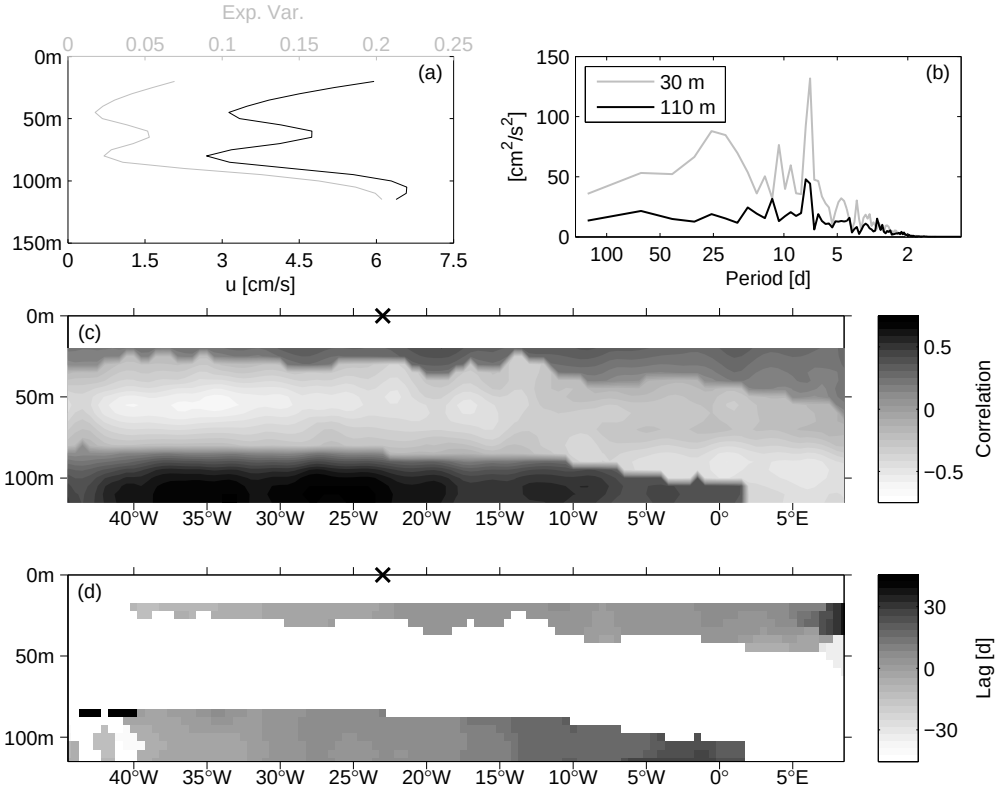

Figure 5.13: (a) Regression amplitude [black; cm/s] and corresponding explained variance (gray) of equatorial zonal velocity anomalies at 23°W onto the 1. CEOF real and imaginary temporal components (see Figure 5.9b). (b) Combined variance-conserving power spectra of 30 m - (gray) and 110 m - (black) zonal velocities at 23°W, 0° [cm^2/s^2] for the first and third deployment periods. (c) Maximum lagged correlation coefficients and (d) corresponding lags between zonal velocity anomalies at 23°W, 0° and SSH anomalies along the equator. Lags are only shown for positive correlation coefficients above 95%-significance level [= 0.14] and anomalies are smoothed by 10.5-day running mean for the correlation analysis; mooring position is marked by black "x" at 0 m. [*Hormann and Brandt*, 2008]

correlation coefficients at around 110 m depth are up to twice as much as near the surface. Note the negative values in between these maxima, with a minimum at about 50 m depth near the western boundary. In case of the near-surface currents largest coefficients are confined to the central and eastern equator whereas maximum values are found at the western and central equator as regards the currents around 110 m depth. Although there are also indications for an eastward propagation along the equator in case of the near-surface currents, such a propagation is more pronounced in the depth range of the primary regression maximum. For the 110 m - zonal velocity anomalies, the corresponding phase velocity can be estimated to about 1.8 m/s which again fits well in the range between the

first and second baroclinic equatorial Kelvin wave modes (see Table 5.2).
While the high correlation coefficients at the central and eastern equator can be related to zonal wind variations in the western and central equatorial Atlantic, such fluctuations are not responsible for the large values in the west as obtained for the depth range of the primary regression maximum (see Figure 5.6b). In this context, wave reflection processes at the western boundary may be of importance, but it was not possible to establish such a mechanism using the available data. *Illig et al.* [2004] suggested that the presence of a strong western boundary current, the NBC, may modify/inhibit reflections of westward propagating Rossby waves into equatorial Kelvin waves. During boreal fall - winter, *Polo et al.* [2008a] surmised a forcing of SSH anomalies in the west by Ekman pumping anomalies due to basinscale atmospheric intraseasonal oscillations associated with shifts of the ITCZ.
For low baroclinic modes, near-surface positive correlation coefficients are associated with Kelvin waves and negative correlation coefficients with Rossby waves. The observed negative correlation coefficients in between regions of positive correlation coefficients near the surface and below the EUC core (Figure 5.13c) might be related to equatorial Rossby waves [e.g., *Moore and Philander*, 1977], but a corresponding westward propagation could not be evidenced here.

5.3 Summary and discussion

The upper equatorial Atlantic variability during 2002 and 2005 was here analyzed with respect to equatorial Kelvin waves; based on both moored and satellite observations.
The inspection of the interannual boreal summer cold tongue variability revealed a warm event during 2002 and a strong cold event during 2005 in conjunction with reduced and enhanced easterlies to the west, respectively. According to its dynamics, the EUC was observed to be embedded in a shallower (deeper) thermocline during boreal summer 2002 (2005) at 23°W, 0°. But while model studies also indicate an overall weakening (increasing) of the upper ocean equatorial circulation during warm (cold) events [see Section 4.3; *Góes and Wainer*, 2003], the EUC core velocity was here observed to be somewhat stronger in 2002 than 2005. *Weisberg et al.* [1987] analyzed moored observations at 28°W, 0° from February 1983 to October 1985 (i.e., covering the warm event during 1984) and noted that the speed at the EUC core remained relatively steady throughout the year.
However, it was shown that anomalous winds in the west can excite Kelvin waves along the equator and former studies suggested a remote forcing of SST anomalies in the eastern equatorial Atlantic via these waves [e.g., *Moore et al.*, 1978; *Servain et al.*, 1982; *McCreary*

et al., 1984]. During both 2002 and 2005, equatorial Kelvin waves were found to be present in moored observations of 20°C-isotherm depth anomalies and dynamic height anomalies at 35°W, 0° and 23°W, 0°. Their phase velocity was basically estimated to be about 1.4 m/s eastward which is in good agreement with the theoretical value of the second baroclinic equatorial Kelvin wave mode (see Tables 5.1 and 5.2).
Eastward propagations along the equator were also prominent in the basinwide SSH anomalies, with an overall phase velocity between $1.8 - 2.0$ m/s. This somewhat higher estimate for the whole period from end-August 2001 to December 2006 fits well in the range between the first and second baroclinic mode of equatorial Kelvin waves. Note that the SSH is most sensitive to the lowest baroclinic modes as for higher baroclinic modes the canceling effect of positive and negative isopycnal displacements within the water column increases. However, the second baroclinic mode was found to be the most energetic in the model study by *Illig et al.* [2004] and *Han et al.* [2008] also suggested a more important role of this mode.

The SSH variability was then described in terms of an equatorial Kelvin wave mode by first performing a least-square fit to the theoretical meridional Kelvin wave structure that was in turn subject to a CEOF analysis. This mode accounted for 50.1% of the variance along the equator and captured well the characteristics of equatorial Kelvin waves, with wave activity exceptionally strong during 2002.
Based on the equatorial Kelvin wave mode, regression analyses were carried out to derive related oceanic variations with respect to the observed differences during 2002 and 2005. The regressed SSH anomalies along the equator clearly illustrated strong discrepencies in Kelvin wave activity during the two years, with generally weaker waves in 2005. While a large part of the SSH variability in both the central and eastern equatorial Atlantic was captured by the regression analysis during 2002, this was different during 2005: In the central part of the basin, more than 50% of the SSH variance could be explained but only about 15% in the east. In addition, the observed evolution of cold tongue SST anomalies was generally captured by the regressed time series during 2002 but the strong cooling during 2005 was not. Thus, these findings confirmed the suggested minor importance of ocean dynamics during the cold event itself (see Figure 5.4f).
The direct influence of equatorial Kelvin waves on SST was found to be generally small, i.e. SST anomalies co-varying with the equatorial Kelvin wave mode explain only a small part of the large SST variability in the cold tongue region. But preconditioning of the upper layer stratification before the onset of the cold tongue may be important for its strength during boreal summer. The examination of the regressed thermocline slope anomalies during 2002 and 2005 revealed that an anomalously reduced (increased) thermocline slope may be favorable for the development of a warm (cold) event. In consequence of an anomalously steep slope, the thermocline will be closer to the surface in the east than usual and

subsurface ocean processes are more tightly coupled to surface processes. As a result, the role of equatorial dynamics may be diminished in this region and the exceptional shallow thermocline in the eastern equatorial Atlantic during boreal summer 2005 [B. Bourlès, pers. comm.] may be a reason for the ascertained minor importance of the equatorial Kelvin waves here compared to 2002.

Anomalous thermocline slopes prior to Atlantic extreme events are generally well established and ocean dynamics are known to play a prominent role in their generation [e.g., *Philander*, 1986; *Weisberg and Tang*, 1987; *Carton and Huang*, 1994; *Carton et al.*, 1996; *Vauclair and du Penhoat*, 2001]. For instance, the anomalous deepening of the oceanic thermocline in the eastern basin prior to the warm event in 1984 that was proceeded by weaker-than-normal trade winds [*Philander*, 1986] resulted from an eastward shift of anomalous heat within the equatorial waveguide [*Carton and Huang*, 1994]. Due to relaxed (intensified) winds in the west, the thermocline there shoals (deepens) and excited equatorial Kelvin waves are believed to be important for the subsequent adjustment of the thermocline slope along the equator [e.g., *Moore et al.*, 1978; *McCreary et al.*, 1984; *Zebiak*, 1993]. In addition, linear equatorial wave reflection theory indicates that an eastward propagating Kelvin wave impinging on a meridional east coast would be reflected into symmetrical westward propagating Rossby waves and coastal Kelvin waves [*Moore and Philander*, 1977]; leading to an extended response throughout the eastern basin.

The reversal of the regressed thermocline slope anomalies during boreal summer also indicates a possible contribution of equatorial Kelvin waves to the oceanic readjustment after the extreme events, with prevailing upwelling (downwelling) Kelvin waves along the equator after the warm (cold) event in 2002 (2005). Otherwise, the simple model study by *Zebiak* [1993] suggested that the dominant processes contributing to the decay of the SST in the eastern equatorial Atlantic are horizontal advection, particularly the meridional component, and the damping effect of the surface heat flux.

However, the zonal velocity anomalies at 23°W, 0° were also found to co-vary with the equatorial Kelvin wave mode and the main effect of these waves was noticed well below the EUC core at 110 m depth, with a secondary maximum near the surface. *Johnson and McPhaden* [1993a] studied the vertical structure of equatorial Kelvin waves in the Pacific using frequency-domain EOFs. Besides an amplitude maximum at the surface, the spatial zonal velocity patterns revealed a local amplitude maximum below the EUC core attributed to wave - mean flow interactions. In a follow-up study, *Johnson and McPhaden* [1993b] identified mean vertical advection as the most important effect in modifying linear equatorial Kelvin wave propagations. A subsurface amplitude maximum in zonal velocity below the EUC core was also found by *Kutsuwada and McPhaden* [2002] investigating intraseasonal variations in the upper equatorial Pacific prior to and during the 1997-98 El Niño.

As a key result here, the presence of equatorial Kelvin waves resulted in a flat (inclined) thermocline prior to the cold tongue onset in 2002 (2005) that is crucial for the shallowing (deepening) of the EUC core at 23°W and that might precondition the development of the warm (cold) event. Preconditioning of the upper layer stratification may also be important for a predictability of Atlantic extreme events that are closely linked with rainfall variability over the tropical ocean and adjacent land regions [e.g., *Carton and Huang*, 1994; *Giannini et al.*, 2003; *Kushnir et al.*, 2006; *Chang et al.*, 2006].

6. Concluding synthesis

The aim of this study was to contribute to the understanding of the ocean's role for climate variability in the tropical Atlantic sector. In this regard, the focus was on the importance of the EUC and equatorial Kelvin waves for SST variability in the eastern Atlantic cold tongue region. On interannual time scales, the coupled ocean-atmosphere variability associated with the zonal mode is often viewed as the Atlantic counterpart of the Pacific ENSO [e.g., *Merle et al.*, 1980; *Xie and Carton*, 2004; *Kushnir et al.*, 2006; *Chang et al.*, 2006]. While considerable progress has been made in understanding tropical Pacific variability with the deployment of the Tropical Atmosphere-Ocean (TAO) array starting in the mid-1980s [*McPhaden et al.*, 1998], observations are more limited in the Atlantic; particularly in the eastern part of the basin.
Although a sufficient number of shipboard current profiling sections is now available in both the western and central equatorial Atlantic to determine the mean structure of the zonal circulation, and to estimate mean transports of the principal equatorial current branches (see Chapter 3), the observations are still not conclusive with regard to the seasonal transport cycles (see Chapter 4). In addition, shipboard measurements usually do not capture interannual transport variability (mainly due to large intraseasonal fluctuations) that can only be determined by moored observations. On the other hand, a single equatorial mooring does not allow definite statements on transport changes, even though they have been shown to be extremely valuable for documenting upper ocean processes such as equatorial waves (see Chapter 5). Despite limitations in spatial and temporal coverage of moored observations compared to satellite data sets typically used to study equatorial wave dynamics, these latter products need to be evaluated against in-situ measurements.

The backbone of the current observational system in the tropical Atlantic are the PIRATA Autonomous Temperature Line Acquisition System (ATLAS) buoys, with data made available in real time, complemented by (non-real time) equatorial subsurface moorings at 35°W, 23°W, 10°W, and 0°. Within the framework of various programs, specifically the Tropical Atlantic Climate Experiment (TACE), observational efforts are underway to extend the moored time series measurements in the central and eastern tropical Atlantic that are essential for the understanding of the relative contributions of air-sea fluxes and ocean dynamics to SST variability and subsurface heat content at seasonal to interannual time

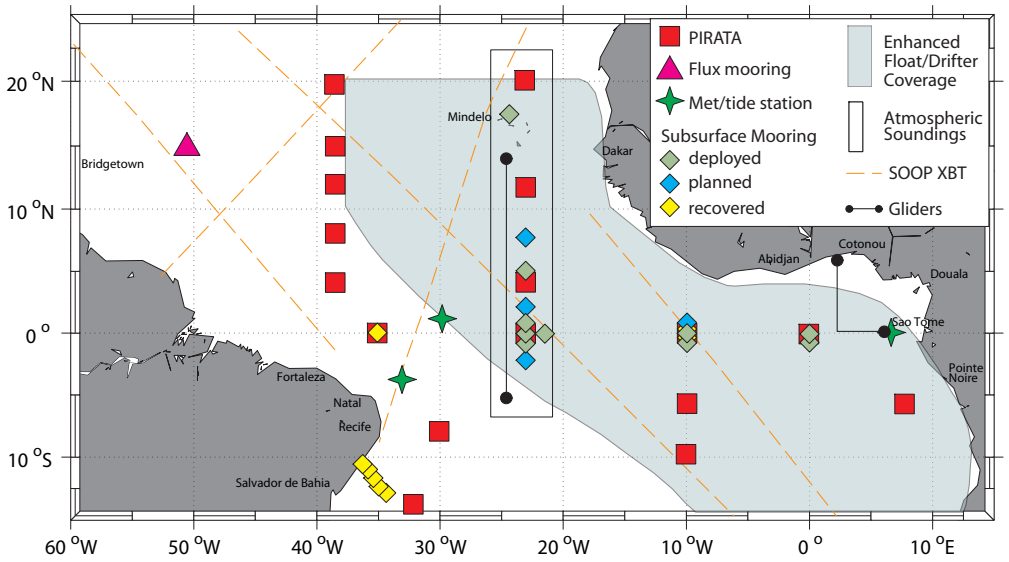

Figure 6.1: TACE observational strategy. The proposed observing system components include (see legend): Continuation of PIRATA moorings, subsurface moorings, island meteorological and tide gauge stations, enhanced float/drifter coverage in the eastern tropical Atlantic, repeated atmospheric soundings along 23°W, ship-of-opportunity (SOOP) expendable bathythermograph (XBT) lines, and selected glider transects. [From http://tace.ifm-geomar.de]

scales. Besides an extended mooring array, the proposed TACE observational strategy includes also an enhanced drifter/float coverage in this region as well as glider transects (see Figure 6.1) [*Schott et al.*, 2004a]. As proven by the Pacific TAO array, intensified observations are needed for a more comprehensive understanding of the underlying dynamics of coupled ocean-atmosphere phenomena and their predictability to develop forecast systems using coupled ocean-atmosphere models.

At present, the eastern equatorial Atlantic is poorly represented in such models and is a region of low prediction skill on seasonal to interannual time scales. Most coupled models without flux corrections show large deviations from observed SST in this area, displacing the cold tongue far to the west and instead possessing a warm eastern equatorial regime [*Davey et al.*, 2002]. Any successful dynamic prediction, requires the elimination of such biasses in the fully coupled models. In order to achieve progress in this regard, a more realistic model representation of the important ocean mechanisms affecting cold tongue SST is required and the current observational initiatives in the tropical Atlantic will provide the necessary data base to critically test and improve forecast models. In this context, the proposed observations can be utilized in the routine generation of assimilation products for both state estimation and initialization of the coupled ocean-atmosphere models.

SST prediction as well as climate change projections in the tropical Atlantic sector are presently still limited, but focused observational and modelling efforts in this region are underway to shed light on the underlying processes that are crucial for advancing the predictability of climate variability in the Atlantic.

Appendix

A1 Linear equatorial wave theory

A brief review of the linear equatorial wave theory is presented to establish the theoretical framework of the analysis in Section 5.2.
Considering the nondimensionalized inviscid shallow water equations on an equatorial β-plane in the long-wave, low-frequency approximation [with c_n defined as the nth baroclinic mode phase speed, nondimensionalization is performed by a horizontal length scale $L = (c_n/\beta)^{1/2}$ and a time scale $T = 1/(\beta c_n)^{1/2}$]:

$$\begin{aligned} u_t - yv + \eta_x &= F \\ yu + \eta_y &= G \\ \eta_t + u_x + v_y &= Q \end{aligned} \tag{A1.1}$$

where u, v, and η are the nondimensionalized zonal velocity, meridional velocity, and sea level, respectively; F, G, and Q are the three nondimensionalized components of the forcing vector; and subscripts denote differentiation.

A detailed solution of the shallow water equations (A1.1) is given by *Cane and Sarachik* [1976]. They have shown that these equations can be reduced to a single equation in v:

$$v_{yy} + (\omega^2 - k\omega^{-1} - k^2 - y^2)v = 0 \tag{A1.2}$$

with k and ω the zonal wavenumber component and frequency, respectively. In nondimensional form, the dispersion relation of the equatorially trapped waves results then in [$v \to 0$ for $y \to \pm\infty$]:

$$\omega^2 - k\omega^{-1} - k^2 = 2m + 1 \tag{A1.3}$$

where m is the meridional mode number (Figure A1.1). The corresponding eigenfunctions are expressed in terms of the Hermite functions:

$$\Psi_m(y) = \pi^{-1/4}(2^m m!)^{-1/2} \exp(-y^2/2) H_m(y) \tag{A1.4}$$

with H_m the mth Hermite polynomial (see Figure A1.2).

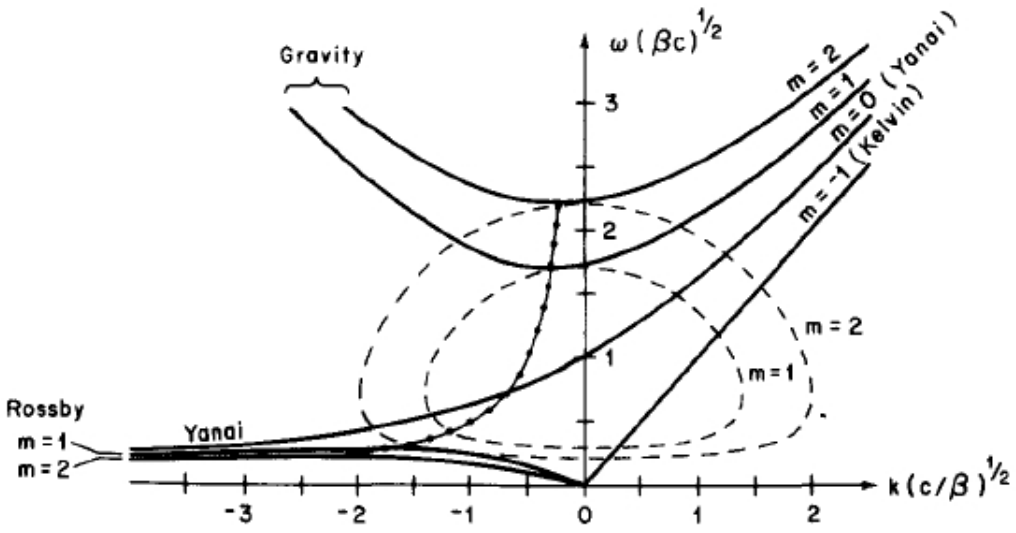

Figure A1.1: Dispersion relation for equatorial wave modes. The scaling applied [length and time scales related by $c = L/T$, $\beta = (LT)^{-1}$] collapses plots for all vertical modes onto one set of curves. In meridional modes $m = 1, 2, \ldots$ the propagating Rossby and inertia-gravity modes are plotted as solid lines, while the complex wavenumber at frequencies between the maximum Rossby and the minimum gravity wave frequency is plotted with dashes (solid/dot) for the imaginary (real) part. Curve for the real part is $\omega k = -\beta/2$ for all m; this is locus of points of zero zonal group velocity. The only physically meaningful root at $m = 0$ is the Yanai or mixed Rossby-gravity wave, which shares with Kelvin wave the property of real wavenumber and eastward group velocity at all ω.[*Knox and Anderson*, 1985]

For the equatorial Kelvin waves, the sea level and zonal velocity fields are

$$\eta = u = \Psi_0(y) \exp(ikx - \omega t) \tag{A1.5}$$

and for the long low-frequency Rossby waves ($m \geq 1$), they become

$$\eta = 2^{-3/2}[(m+1)^{-1/2}\Psi_{m+1}(y) + m^{-1/2}\Psi_{m-1}(y)] \exp(ikx - \omega t) \tag{A1.6}$$

$$u = 2^{-3/2}[(m+1)^{-1/2}\Psi_{m+1}(y) - m^{-1/2}\Psi_{m-1}(y)] \exp(ikx - \omega t) \tag{A1.7}$$

Note that (1) at low frequency, Kelvin waves as well as long Rossby waves are nondispersive and have η and u in geostrophic balance; and (2) the phase (= group) speeds of the equatorial Kelvin wave c_k and Rossby wave c_r are linked by the following relationship:

$$c_r = -c_k/(2m+1) \tag{A1.8}$$

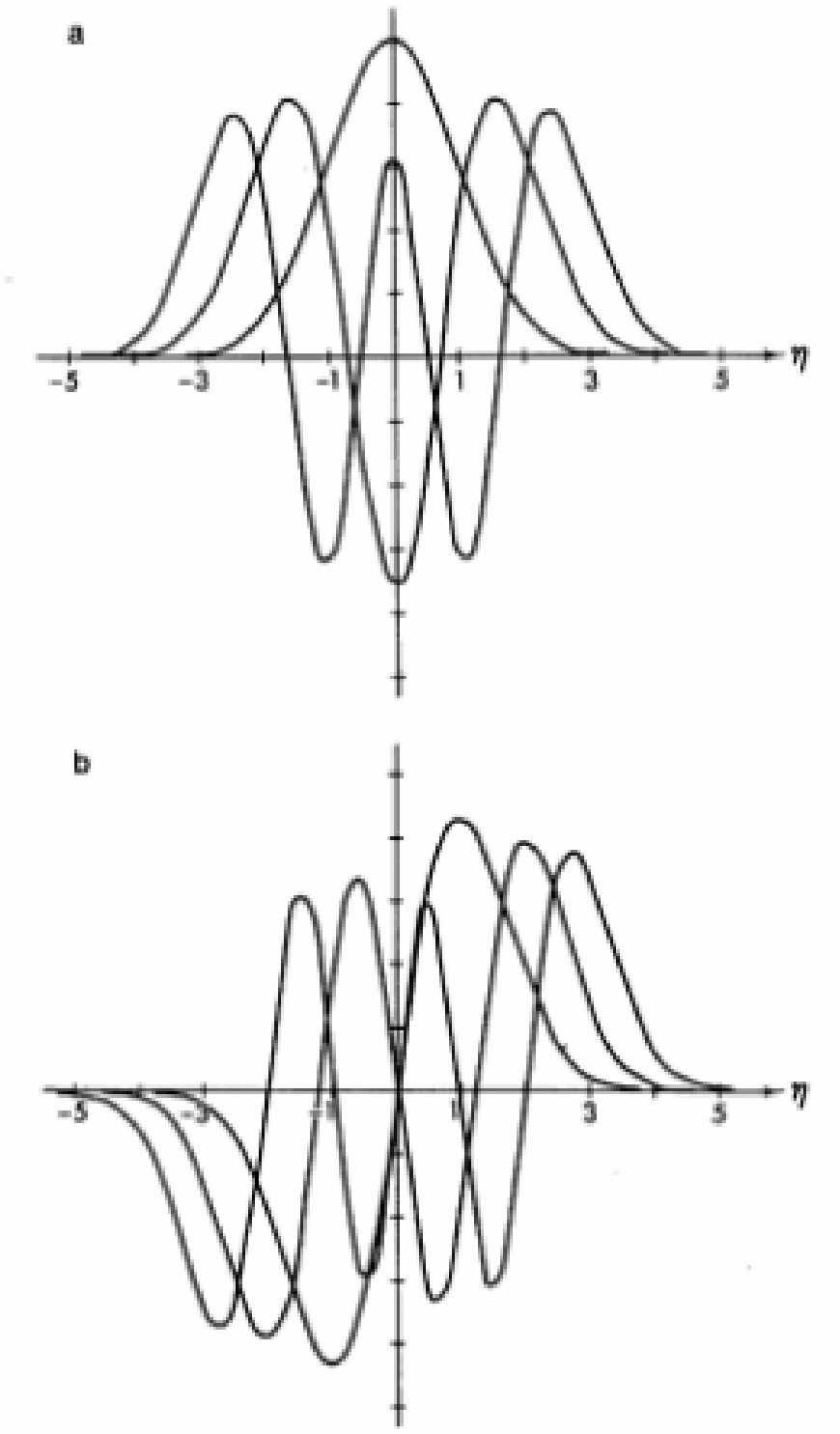

Figure A1.2: The latitudinal structure of (a) symmetrical and (b) antisymmetrical Hermite functions that describe the meridional velocity component. The unit of distance in the northward direction is the equatorial radius of deformation. [*Philander*, 1990]

A2 Oxygen tongues and zonal currents

Recent moored observations at 23°W confirmed the presence of westward mean current cores associated with the EIC below the EUC [*Brandt et al.*, 2006]. A strong seasonal cycle of the flow in the depth range of the EIC as suggested by different model studies [*Jochum and Malanotte-Rizzoli*, 2003; *Thierry et al.*, 2004] is in general agreement with recent observations of seasonal variability of the equatorial current and density fields [*Brandt and Eden*, 2005]. This variability can be best described by equatorial Kelvin and Rossby beams represented by the first few baroclinic modes [*McCreary*, 1984]. At intermediate depths (as well as at larger depth) the zonal circulation often shows the presence of vertically alternating eastward and westward jets with short vertical length scales [e.g., *Ponte et al.*, 1990; *Gouriou et al.*, 2001]. In the deep water layers of the central equatorial Atlantic, eastward jets are associated with a maximum in Chlorofluorocarbon concentration indicating advection of newly formed North Atlantic Deep Water from the western boundary toward the interior Atlantic [*Andrié et al.*, 1998; *Gouriou et al.*, 2001; *Bourlès et al.*, 2003]. These so-called equatorial deep jets or stacked jets are in general not well represented in present ocean general circulation models, probably because their simulation requires very high vertical and horizontal resolutions [*d'Orgeville et al.*, 2007; *Eden and Dengler*, 2008].

New current and hydrographic observations are used here to describe the mean and interannually varying equatorial circulation and its effects on the oxygen distribution in the equatorial belt.

Zonal flow in the equatorial Atlantic

The zonal velocity on the equator at 35°W and 23°W as measured by the moored ADCPs (Figure A2.1) shows the eastward flowing EUC as the dominant signal. The core depths (core velocities) in the Eulerian mean flow field are 95 m (69 ± 3 cm/s) at 35°W and

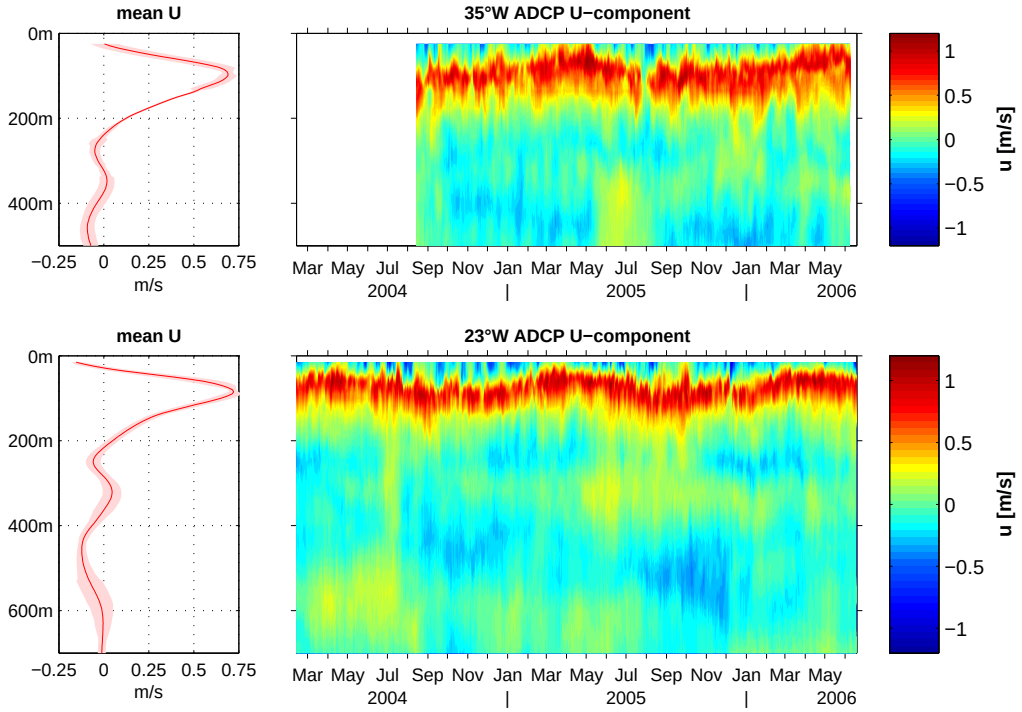

Figure A2.1: (Upper panels) Zonal velocity at the equator, 35°W from two 150-kHz narrow-band ADCPs, and (lower panels) zonal velocity at the equator, 23°W from 300-kHz Workhorse ADCPs and 75-kHz Long Ranger ADCPs. Data are detided, and data gaps in between the instruments are interpolated. The mean flow is calculated by subtracting the annual and semiannual harmonics (left panels, solid red line) with standard error (shaded). [*Brandt et al.*, 2008]

85 m (72 ± 2 cm/s) at 23°W, respectively. The seasonal cycle of the equatorial zonal velocity associated with the EUC shows a shallow current core during March to April and a deep current core during late summer to autumn. During the latter phase the ITCZ is farthest north, the zonal wind on the equator is westward, the zonal surface pressure gradient is strongest toward the east and the near-surface flow is strongest toward the west [see Chapter 4; *Provost et al.*, 2004]. In general, the EUC at 35°W extends deeper and has a larger vertical extent compared to the EUC at 23°W. The standard error[1] of the mean zonal velocity in the depth range of the EUC is small, despite the large standard deviation of about 15 cm/s. This is due to the high numbers of degrees of freedom (NDF) of the time series resulting from pronounced intraseasonal fluctuations (see Figure A2.1 and Table A2.1).

[1] The standard errors of the moored mean currents, calculated after subtracting annual and semiannual harmonics of the moored time series, are estimated by scaling the standard deviations with the numbers of degrees of freedom (NDF; see e.g. Table A2.1) determined from the autocorrelation of the detided time series.

	Depth [m]	Mean [m/s]	Standard Deviation [m/s]	Standard Error [m/s]	NDF
		Equator, 35° *W*			
Near surface	25	0.00	0.18	0.03	49
EUC	95	0.69	0.17	0.03	36
EIC, upper core	280	-0.05	0.09	0.03	10
Eastward core	345	0.02	0.08	0.02	16
EIC, lower core	455	-0.09	0.08	0.02	12
		Equator, 23° *W*			
Near surface	15	-0.15	0.21	0.02	101
EUC	85	0.72	0.15	0.02	55
EIC, upper core	250	-0.06	0.07	0.02	17
Eastward core	320	0.05	0.10	0.05	4
EIC, lower core	455	-0.12	0.05	0.01	23

Table A2.1: Depth of local maxima of the zonal flow on the equator at 35°W and 23°W; together with means, standard deviations, standard errors, and numbers of degrees of freedom (NDF) of the zonal velocity time series. [*Brandt et al.*, 2008]

Above the EUC the mean flow, as estimated by surface drifter trajectories, is westward [*Lumpkin and Garzoli*, 2005]. Their climatology, yielding a zonal flow on the equator of -13 ± 15 cm/s at 35°W and -19 ± 14 cm/s at 23°W, can be compared to the uppermost ADCP measurements. The upward looking ADCP at 23°W yielded better data to shallower depths than did the instrument at 35°W owing to a shallower instrument position and less range reduction associated with surface reflections. The moored mean near-surface velocity of 0 ± 3 cm/s in 25 m depth at 35°W and -15 ± 2 cm/s in 15 m depth at 23°W are smaller than the drifter velocities from the climatology. This discrepancy may result from the vertical shear present in the upper 20 m of the water column that was not covered by the moored observations and is completely missed by standard shipboard observations.

Below the EUC, the zonal flow measured by the moored ADCPs is mostly westward and associated with the EIC (Figure A2.1). The deeper current meters at 35°W, down to 1100 m, also recorded predominantly westward velocities (Figure A2.2), which confirm previous results obtained from shipboard measurements at 35°W showing westward velocities in the depth range from below the EUC down to 2500 m [*Schott et al.*, 2003]. The amplitudes of the annual harmonics of the deeper velocity time series are larger than 10 cm/s at 500 m, 652 m, and 809 m with maximum eastward velocities in July, May, and March, respectively. These findings are in general agreement with the presence of down-

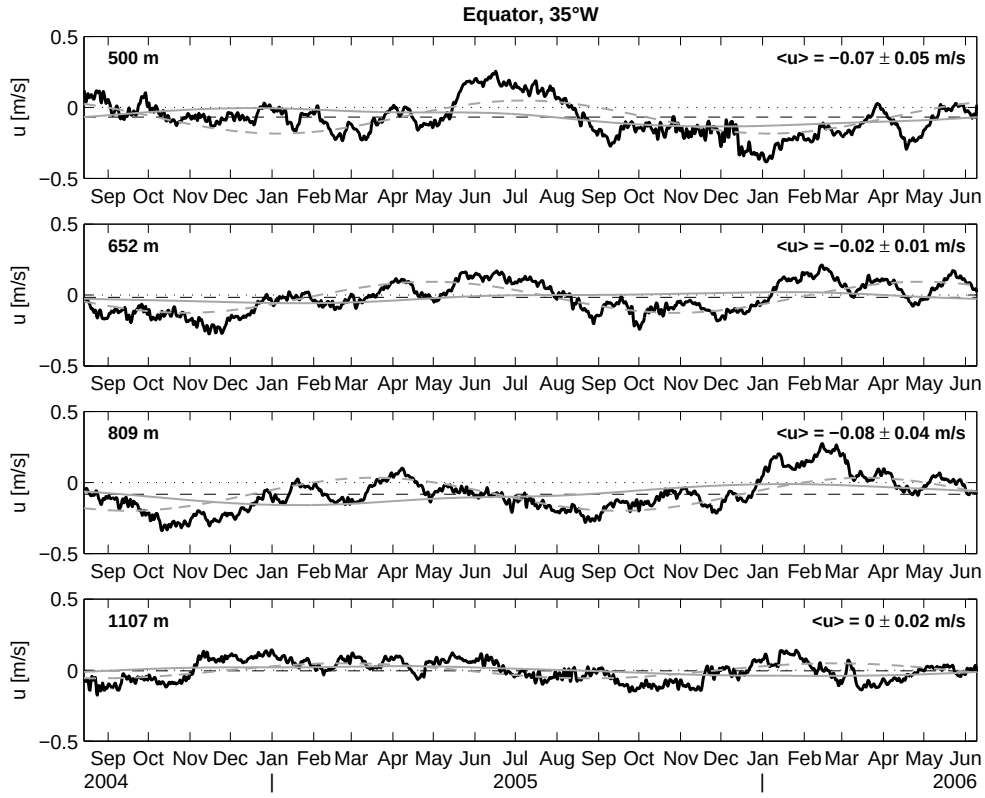

Figure A2.2: Zonal velocity time series from four Argonaut current meters at the equator, 35°W (solid black lines). Also given are interannual variations (solid gray lines) calculated by subtracting annual and semiannual harmonics and 9-month low-passed filtering, annual harmonics (dashed gray lines), and deployment-long means (black dashed lines) with standard error, calculated by subtracting annual and semiannual harmonics. Zero velocity is marked by dotted lines. [*Brandt et al.*, 2008]

ward propagating Rossby beams as already suggested from the analysis of meridional ship sections taken along 35°W by *Brandt and Eden* [2005].

Ollitrault et al. [2006], analyzing trajectories of acoustically tracked floats drifting at 750 to 850 m also obtained a mean westward velocity on the equator of -6 ± 2 cm/s between 33°W and 20°W that was attributed to the EIC. The moored mean at 35°W at about 800 m depth yields -8 ± 4 cm/s (Figure A2.2), slightly larger than the float velocity, but in agreement within the standard errors of both observations.

The mean flow structure obtained in the western and central Atlantic shows many similarities with that of the Pacific. *Firing et al.* [1998] described a westward EIC in the depth range $250 - 500$ m using direct current measurements from 41 sections taken along 159°E within about 16 months. Below 500 m, down to 2500 m the flow was still mostly westward, however, superimposed by current bands with short vertical scales. Using direct current

measurements of the upper 400 m, *Johnson et al.* [2002] found a westward strengthening of the EIC with strong westward velocities at about 350 m depth in the western Pacific west of 155°W and weak or slightly eastward flow east of that longitude at the same depth. In the moored records from 35°W and 23°W, two cores of westward flow can be identified in the EIC depth range. The upper core of the EIC deepens from about 250 m at 23°W to about 280 m at 35°W, following the depth changes of the lower EUC limit located above. In contrast, the lower core of the EIC stays at the same depth from 23°W to 35°W (Figure A2.1 and Table A2.1). Between the two westward flowing cores insignificant mean eastward flow is found (Figure A2.1 and Table A2.1). The particularly large standard error at 23°W below the EUC is predominantly due to strong interannual variability that will be discussed in the following.

Oxygen tongues and zonal jets

The oxygen distribution in the ocean is a result of a subtle balance between supply via advection and diffusion and oxygen consumption as a result of heterotrophic respiration. In the tropical Atlantic, oxygen minimum zones (OMZs) are located north and south of the equator in the shadow zones of the ventilated thermocline [*Luyten et al.*, 1983]. The 23°W section from 4°S to 15°N that was taken during June - July 2006 cuts through the OMZ of the tropical North Atlantic as well as through the equatorial belt (Figure A2.3). Minimum dissolved oxygen values of about 17 μmol/kg and 40 μmol/kg in the South and North Atlantic, respectively, are found at depths of 300 to 500 m or in the potential density range $\sigma_\theta = 26.6\,\mathrm{kg/m^3}$ to $\sigma_\theta = 27.1\,\mathrm{kg/m^3}$ [*Tsuchiya et al.*, 1992; *Karstensen et al.*, 2008; *Stramma et al.*, 2008]. The potential density surface $\sigma_\theta = 27.1\,\mathrm{kg/m^3}$ represents the boundary between Central Water and Antarctic Intermediate Water. In general, there is an eastward decrease of dissolved oxygen concentration throughout the central and intermediate water layers from the western boundary regime toward the sluggish flow near the eastern boundary. In the equatorial zone, westward and eastward subsurface jets are thus often characterized by low and high oxygen concentrations, respectively.

Below the surface mixed layer, the EUC can be identified as an oxygen maximum. The cross-sectional area of the EUC with dissolved oxygen values larger than 130 μmol/kg as well as the oxygen maximum at about the core depth of the EUC decreases from 35°W to 10°W (Figure A2.4). The EUC mainly carries ventilated waters from the southern hemisphere supplied by the NBUC in the potential density range $\sigma_\theta = 24.5 - 26.8\mathrm{kg/m^3}$ [*Metcalf and Stalcup*, 1967; *Tsuchiya et al.*, 1992; *Schott et al.*, 1995, 2005]. The high-oxygen tongue associated with the EUC is flanked by low-oxygen waters transported westward with the

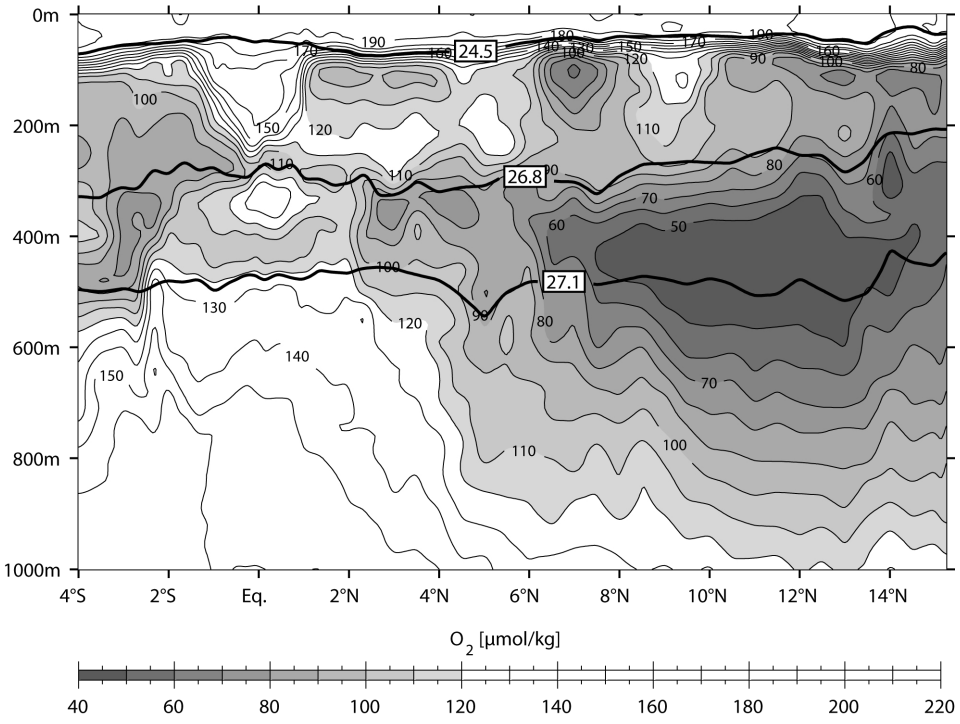

Figure A2.3: Dissolved oxygen [μmol/kg] along 23°W from shipboard observations in June - July 2006. Also included are depths of potential density surfaces [kg/m^3] (thick solid lines). [*Brandt et al.*, 2008]

nSEC and eSEC [*Stramma and Schott*, 1999].

The shipboard observations during June - July 2006 show a secondary oxygen maximum underneath the EUC between the upper and lower cores of the EIC (Figure A2.4). This tongue of increased dissolved oxygen can be found at the three meridional sections along 35°W, 23°W and 10°W between about 300 and 350 m depth. It can also be followed along the equatorial section from 23°W to 10°W, with the maximum dissolved oxygen concentration decreasing from 130 μmol/kg at 23°W to 110 μmol/kg at 10°W (Figure A2.4, lower panel). As already discussed, the moored mean velocity profiles at 35°W and 23°W show an eastward velocity anomaly between two westward velocity cores associated with the EIC, which is associated with the oxygen tongue. Velocity measurements at 23°W during June - July 2006 strongly deviate from the annual mean profile for the period March 2005 to February 2006 suggesting that the high-oxygen tongue is generated by the eastward jet prevailing during the preceding year (Figure A2.5). Above and below this oxygen maximum, low oxygen values are associated with the upper and lower core of the westward flowing EIC. The dissolved oxygen concentration increases in these EIC cores from 10°W to 35°W.

While the two EIC cores represent a drainage pathway for low-oxygen waters from the OMZs, the eastward jet in between represents a pathway for high-oxygen waters toward

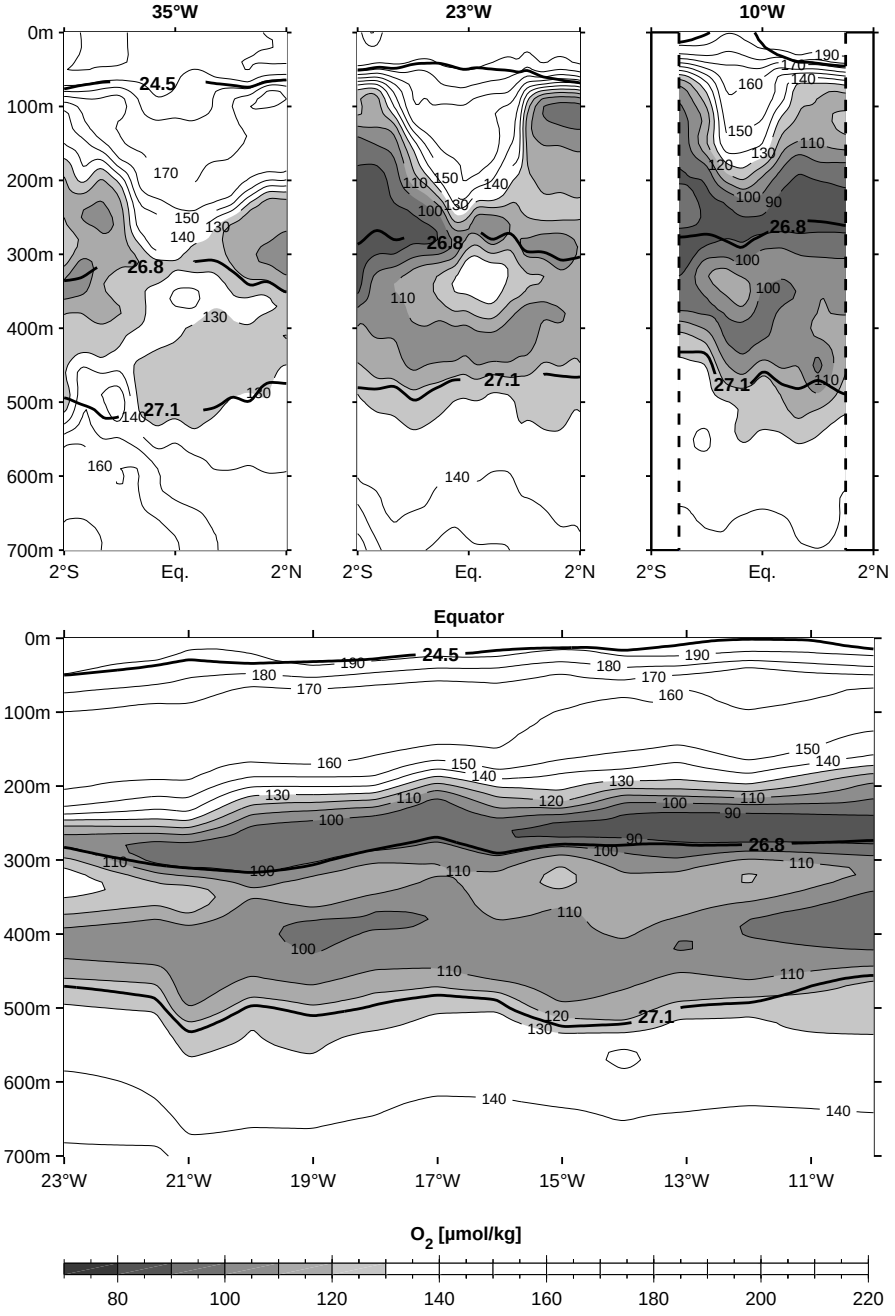

Figure A2.4: Dissolved oxygen [μmol/kg] from shipboard observations in June - July 2006 along meridional sections crossing the equator at (upper left panel) 35°W, (upper middle panel) 23°W, and (upper right panel) 10°W, and (lower panel) along the equator. Also included are depths of potential density surfaces [kg/m^3] (thick solid lines). Dashed lines in (upper right panel) mark the measurement limits at 10°W. See text for details. [*Brandt et al.*, 2008]

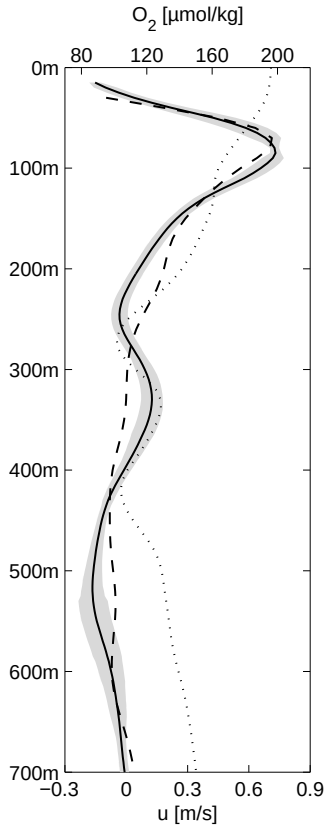

Figure A2.5: Zonal velocity [m/s; lower x axis] and dissolved oxygen [μmol/kg; upper x axis] at 23°W, 0°. Solid curve denotes zonal velocity obtained from moored instruments for the period March 2005 to February 2006 with standard error derived for the whole mooring period February 2004 to June 2006 (see Figure A2.1, left panels; shaded); dashed and dotted curves denote zonal velocity and dissolved oxygen, respectively, observed in June 2006 and averaged between 1°S and 1°N. [*Brandt et al.*, 2008]

the eastern equatorial Atlantic. Previous observational studies concentrated on the SICC and NICC which are located at about 2°S and 2°N and which are marked by high oxygen values originating in the NBUC [*Tsuchiya et al.*, 1992; *Schott et al.*, 1995; *Boebel et al.*, 1999; *Bourlès et al.*, 2002]. In particular, the NICC was identified as an oxygen source for the OMZ of the tropical North Atlantic [*Stramma et al.*, 2005]. In the observational data taken during June - July 2006, the highest oxygen values in the depth range of the tropical OMZ are found directly at the equator (Figure A2.3).

Acoustically tracked RAFOS floats [*Rossby et al.*, 1986] drifting along isopycnal surfaces are additionally used to study the equatorial circulation and the rapid exchange between the western boundary current regime and the eastern tropical Atlantic is captured by the

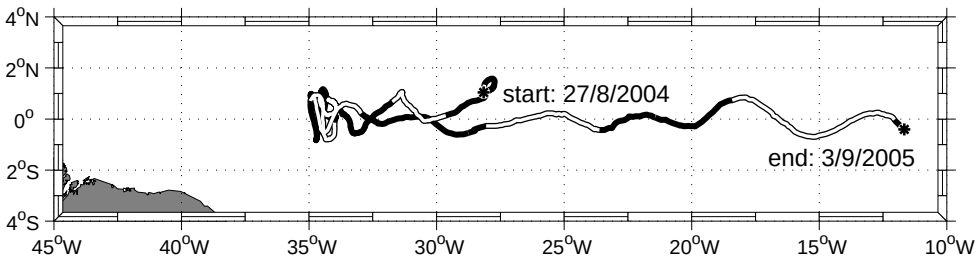

Figure A2.6: Trajectory of an acoustically tracked RAFOS float (RAFOS 623) drifting at potential density surface $\sigma_\theta = 26.8\,\mathrm{kg/m^3}$ (about 300 m depth). Even months are plotted white, and odd months are plotted black. [*Brandt et al.*, 2008]

RAFOS float trajectory[2] shown in Figure A2.6. This float drifted on an isopycnal surface of $\sigma_\theta = 26.8\,\mathrm{kg/m^3}$ at about 300 m depth. After a relative slow westward drift starting at 1°N, 28°10′W in August 2004 the float reached the equator at 35°W in December 2004 (Figure A2.7, yellow arrows). There the float stalled until April 2005. With the onset of eastward flow at 35°W (Figure A2.1), the float accelerated eastward and covered the distance between 35°W and 12°W in about 5 months, meandering around the equator along its way east. During the latter period, the Lagrangian zonal velocity fluctuated between 15 and 30 cm/s (Figure A2.7).

Figure A2.7 summarizes direct velocity observations at the depth of the potential density surface $\sigma_\theta = 26.8\,\mathrm{kg/m^3}$ from the two equatorial moorings at 35°W and 23°W and from RAFOS floats drifting near the equator between 1°S and 1°N. These observations suggest large zonal coherence of the eastward jet during May to September 2005.

To address the relative importance of oxygen consumption, diapycnal turbulent diffusivity, and lateral eddy diffusivity, the following Lagrangian diffusion equation for the oxygen decrease along the equator from 35°W to 10°W within the oxygen tongue at $300 - 350$ m is applied:

$$\frac{\partial C}{\partial t} = -JC + K_\nu \frac{\partial^2 C}{\partial z^2} + K_h \frac{\partial^2 C}{\partial y^2} \tag{A2.1}$$

Here, C is the dissolved oxygen concentration, J is the dissolved oxygen consumption constant, K_ν is the coefficient of the diapycnal turbulent diffusivity, and K_h is the coefficient of the lateral eddy diffusivity. The temporal derivative on the left-hand side of Equation A2.1 must be balanced by the sum of the terms on the right-hand side. The temporal derivative can be estimated given the time that the RAFOS float (Figure A2.6) needed

[2] For the calculation of float trajectories, the arrival time data of acoustic signals stored by the floats are used. These signals were transmitted from seven different sound sources at a repetition period of 12 h. To get an optimum coverage the sound sources were distributed between 35°W and 10°W and between 10°S and 1°N. The RAFOS floats used here were equipped with a compressee adjusting the float compressibility to that of seawater [*Rossby et al.*, 1985].

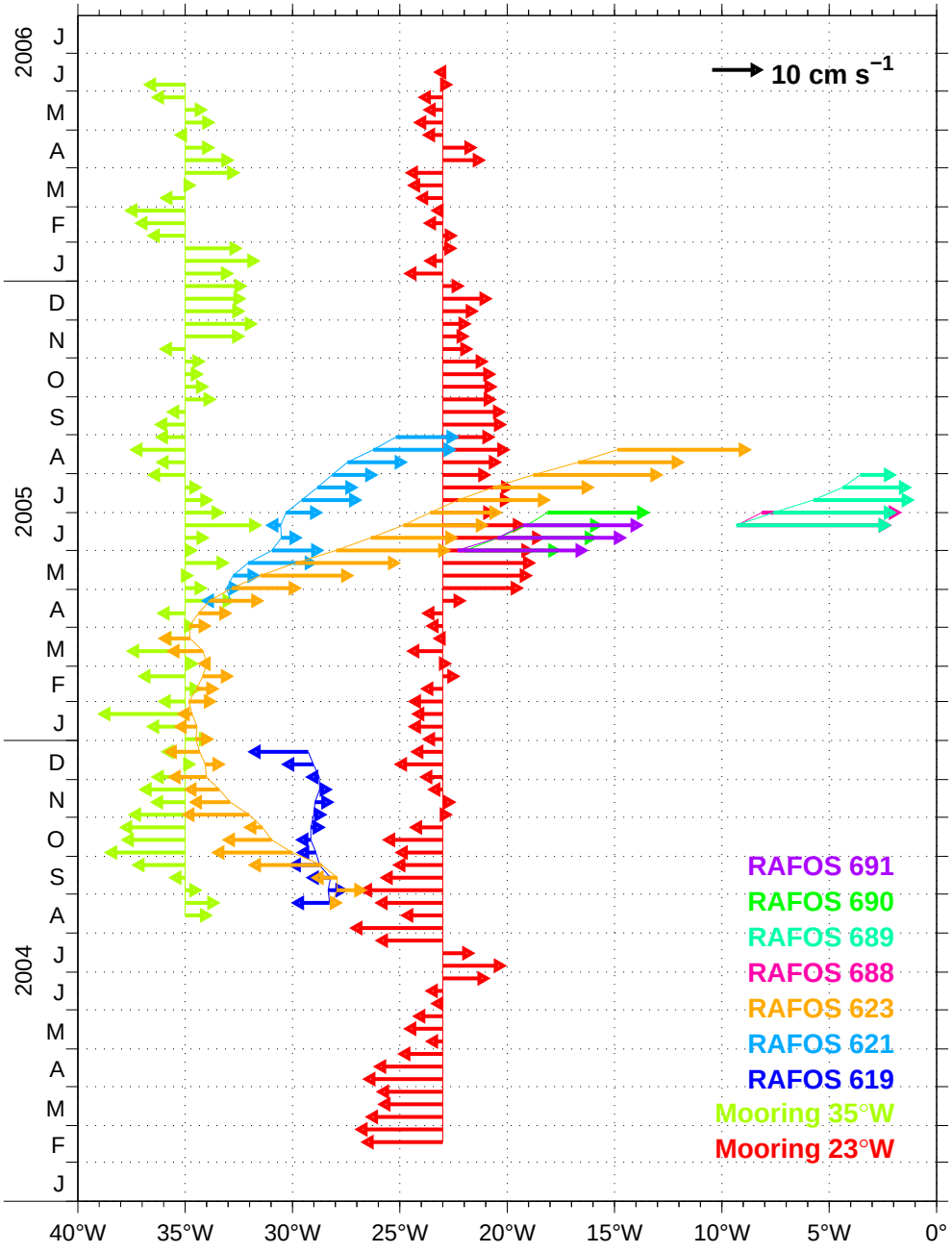

Figure A2.7: Zonal velocity at the equator at the depth of the potential density surface $\sigma_\theta = 26.8\,\mathrm{kg/m^3}$ (about 300 m depth) from moored observations at 35°W and 23°W as well as from RAFOS float trajectories drifting near the equator between 1°S and 1°N. Trajectory of RAFOS float 623 is shown in Figure A2.6. [*Brandt et al.*, 2008]

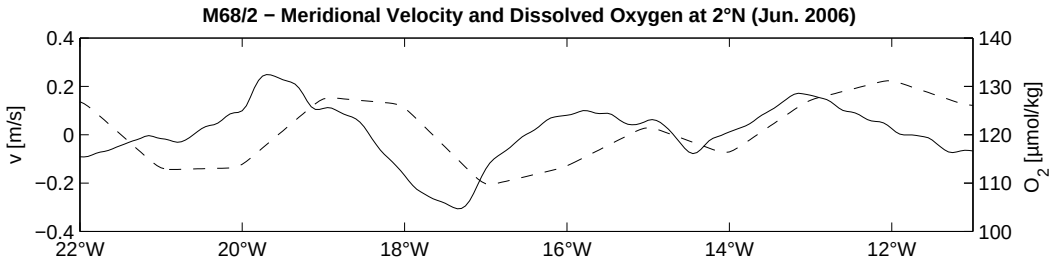

Figure A2.8: Meridional velocity component [m/s; solid, left y axis] and dissolved oxygen [μmol/kg; dashed, right y axis) along 2°N averaged between 400 and 600 m depth from shipboard observations in June 2006. [*Brandt et al.*, 2008]

to travel from 35°W to 10°W, that is, about 6 months. The difference in the dissolved oxygen concentration at the core of the oxygen tongue from 35°W to 10°W measured in June - July 2006 was about $-30\,\mu$mol/kg. Thus, the left-hand side of Equation A2.1 is about $-60\,\mu$mol/kg a^{-1}. The first term on the right-hand side of Equation A2.1 describes the oxygen consumption, which is taken from literature. *van Geen et al.* [2006] estimated the dissolved oxygen consumption constant by constraining a one-dimensional advection-diffusion model for the North Pacific OMZ with Chlorofluorocarbon data. Using their best fit value of 0.041 a^{-1} and a mean dissolved oxygen concentration of 130 μmol/kg, an oxygen consumption rate of 5.3 μmol/kg a^{-1} is obtained. This is in general agreement with rates estimated for the Pacific and Atlantic Oceans by *Karstensen et al.* [2008], who obtained a maximum oxygen consumption rate of about 10 μmol/kg a^{-1} below the euphotic zone decreasing exponentially with depth. The oxygen consumption is one order of magnitude smaller than the temporal derivative of Equation A2.1 and cannot explain the decrease in oxygen concentration from west to east within the core of the oxygen tongue.
The diapycnal turbulent diffusivity and the lateral eddy diffusivity are estimated by fitting second-order polynomials to vertical and horizontal profiles, respectively, through the oxygen maximum of the oxygen tongue. The obtained quadratic coefficients varied only slightly among the different oxygen distributions at 35°W, 23°W, and 10°W and correspond to a reduction in oxygen of 10 μmol/kg within mean distances of 37 m and 63 km above/below and north/south of the oxygen maximum, respectively. Using a diapycnal turbulent diffusivity coefficient of $K_\nu = 10^{-5}$ m^2/s that is at the upper bound of coefficients observed in the equatorial Pacific and Atlantic Oceans below the EUC [*Gregg et al.*, 2003], a diapycnal turbulent diffusivity of $-4.7\,\mu$mol/kg a^{-1} results. This value is of the same order of magnitude as the oxygen consumption, but it is also one order of magnitude smaller than the temporal derivative in Equation A2.1.

Using a lateral eddy diffusivity coefficient of $K_h = 400$ m^2/s that can be considered as a typical value [*Eden et al.*, 2007], a lateral eddy diffusivity of $-63\,\mu$mol/kg a^{-1} results.

These rough estimates suggest that the reduction of the dissolved oxygen concentration from west to east in the core of the oxygen tongue is dominantly balanced by lateral eddy diffusivity. Substantial meridional velocity and oxygen fluctuations that possibly generate lateral eddy fluxes were in fact observed in June 2006 along the zonal section along 2°N in the depth range 400 to 600 m (Figure A2.8). Such fluctuations could result in an oxygen flux away from the equatorial region toward the OMZs of the tropical North and South Atlantic.

Interannual variability of zonal flow

The zonal velocity on the equator at 23°W at about 300 m depth, shows predominantly westward flow from February 2004 to February 2005 and eastward flow during a 7-month period afterward (Figure A2.7) suggesting substantial interannual variability of the flow at intermediate depths. The strong year-to-year variability below the EUC at 23°W becomes also evident, when calculating successive annual mean zonal velocities, that is, from March 2004 to February 2005 and from March 2005 to February 2006, respectively (Figure A2.9). While the EUC remains almost unchanged, the annual mean velocities below 300 m differ by up to 20 cm/s. Main differences between the two annual mean profiles are a weakening of the upper core of the EIC, a strengthening of the eastward velocity anomaly between the two cores of the EIC associated with a lowering of the intermediate maximum, and a lowering of the lower core of the EIC.

Strong interannual variability of the flow at intermediate depth was also found in a regional model of the tropical Atlantic forced by interannually varying wind fields [*Brandt and Eden*, 2005]. The simulated interannual variations in the velocity field were interpreted as downward propagating Kelvin and Rossby beams. However, these beams that are similar to those obtained for the annual cycle are composed of the first few baroclinic modes and are not able to explain the short vertical scales associated with the observed eastward jet within the EIC.

Top to bottom velocity profiles have revealed the existence of high baroclinic mode variability in the equatorial Atlantic, occupying almost the whole water column below the EUC [*Ponte et al.*, 1990; *Gouriou et al.*, 1999; *Schmid et al.*, 2005; *d'Orgeville et al.*, 2007]. These stacked jets are characterized by alternating zonal flow with amplitudes of up to 20 cm/s and a meridional scale of about 1° in latitude. In the deeper ocean, their vertical wavelengths peak at about 600 m, which corresponds to vertical modes 14 through 16 [*Gouriou et al.*, 1999; *Eden and Dengler*, 2008]. Here, a vertical mode decomposition of a top to bottom mean density profile from the central equatorial Atlantic is performed. The resulting

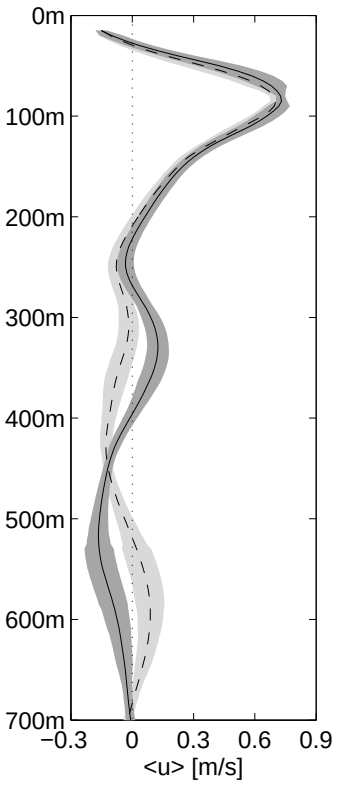

Figure A2.9: Annual mean equatorial zonal velocity profiles at 23°W for March 2004 to February 2005 (dashed) and March 2005 to February 2006 (solid). Standard errors are derived for the whole mooring period February 2004 to June 2006 (see Figure A2.1, left panels; shaded). [*Brandt et al.*, 2008]

dimensionless vertical structure functions are then fitted to the vertically detrended 23°W mooring data between 200 m and 700 m using a covariance criterion. The obtained vertical mode spectrum (Figure A2.10a) shows higher energy levels at vertical modes 12 through 20, with a distinct peak at mode 15. A comparison between this vertical mode spectrum and a vertical mode spectrum calculated from velocity data between 700 and 2000 m is depicted in Figure A2.10a. The used 47 deep zonal velocity profiles are acquired between 0.5°S and 0.5°N and between 35°W and 23°W. The mean deep vertical mode spectrum shows smaller energy levels than the shallow vertical mode spectrum, while single deep vertical mode spectra may overcome the energy levels of the mean shallow vertical mode spectrum. However, largest energy levels in the deep spectrum are found between mode 13 and 21 suggesting that the high baroclinic mode fluctuations at shallower depth have similar vertical wavelengths as the stacked jets in the deeper water column as analyzed by *Eden and Dengler* [2008].

A description of the temporal variability of the stacked jets is particularly difficult owing to their long time scales. While an analysis of extensive hydrographic data by *Johnson*

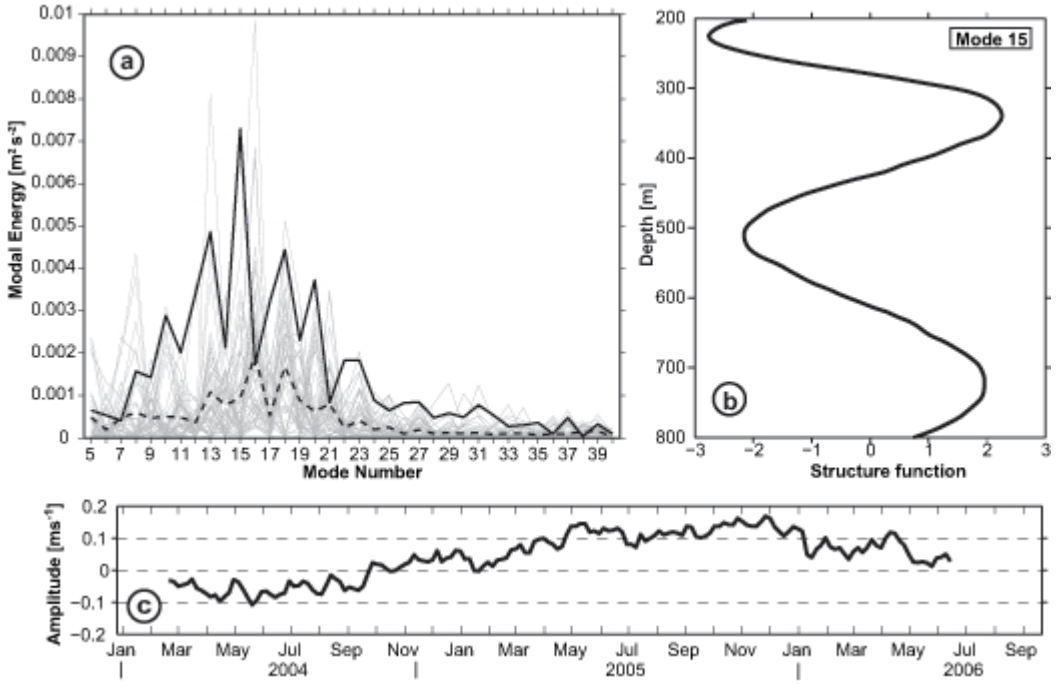

Figure A2.10: Vertical mode analysis of zonal velocity at the equator, 23°W. Vertical mode spectrum (a) is obtained by fitting dimensionless vertical structure functions to moored velocity data from below the EUC between 200 and 700 m (thick solid line) using a covariance criterion. In (b) the dimensionless vertical structure function of mode 15 is shown, and in (c) the time series of the corresponding amplitude is shown. Also included in (a) are vertical mode spectra that are calculated from zonal velocity data between 700 and 2000 m (thin gray lines) of 47 deep velocity profiles measured between 0.5°S and 0.5°N and between 35°W and 23°W as well as their mean (dashed line). [*Brandt et al.*, 2008]

and Zhang [2003] suggested a period of stacked jets of about 5 years, recent direct velocity observations show that individual jets seem to persist over a time span from 6 months to 2 years [*Send et al.*, 2002; *Schmid et al.*, 2005; *Bunge et al.*, 2006]. *Firing* [1988] described jet-like structures in the Pacific Ocean at intermediate depths below the EUC. In his observations, these jets were nearly constant in depth for about half of the 16-month time series, while constantly rising during the rest of the observational period. In the moored data set used here, the mode (mode 15, Figure A2.10b) that best represents the eastward jet has eastward velocities at 330 m from February 2005 to May 2006 (Figure A2.10c). The temporal behavior of the observed feature thus agrees with the temporal behavior of stacked jets observed previously.

The high-resolution oxygen distribution of different meridional sections taken during RV Thalassa cruise along 23°W in August 1999, during RV Ron Brown cruise along 25°W in August 2003, and during RV Meteor cruise along 23°W in June - July 2006 (Figure A2.11)

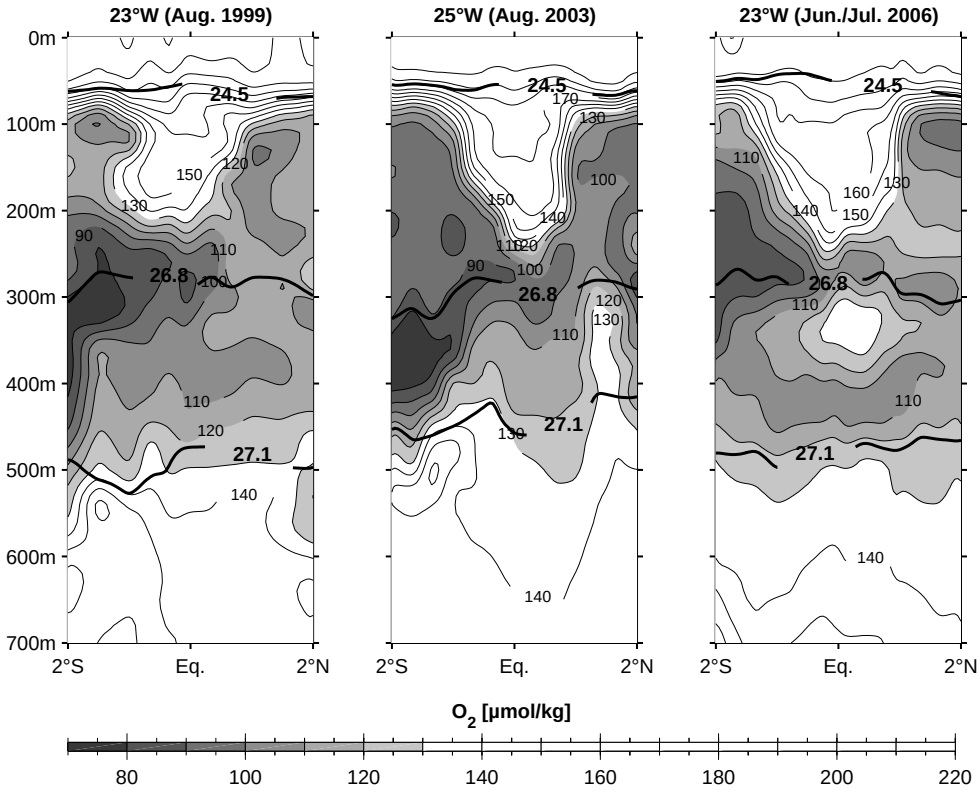

Figure A2.11: Dissolved oxygen [μmol/kg] from shipboard observations along meridional sections crossing the equator at 23°W in August 1999, at 25°W in August 2003, and at 23°W in June - July 2006. Also included are depths of potential density surfaces [kg/m^3] (thick solid lines). [*Brandt et al.*, 2008]

additionally suggest a large variability in the occurrence of the jets in the central equatorial Atlantic. During August 1999 and August 2003 the dissolved oxygen concentration at intermediate depths ($300 - 700$ m) does not show an equatorial oxygen maximum. During August 2003 the oxygen concentration is enhanced away from the equator, particularly at about 1.5°N. This structure can be explained by the presence of the SICC and NICC with eastward core velocities larger than 10 cm/s as found in the mean zonal velocity field obtained from different ship sections in the central equatorial Atlantic (see Section 3.1). However, during June - July 2006 the situation changed and maximum dissolved oxygen concentration is found right on the equator at 300 to 350 m depth that could be explained by the presence of a strong eastward zonal jet prevailing during the preceding year.

Summary and Discussion

The availability of about 22-month- and 28-month-long velocity time series from 35°W and 23°W allows for the first time to determine annual mean zonal velocities at two separate equatorial positions unbiased by seasonal Rossby waves. It was shown that during the observational period a westward flowing EIC was present at 35°W and 23°W consisting of two current cores at about 250 m and 450 m depth, respectively. The upper core deepens westward from 23°W (mean velocity of 6 ± 2 cm/s) to 35°W (mean velocity of 5 ± 3 cm/s) by about 30 m. The lower core is about twice as strong with 12 ± 1 cm/s at 23°W and 9 ± 2 cm/s at 35°W.

A similar two-core structure of the EIC was simulated in a high-resolution model of the Atlantic Ocean [*Böning and Kröger*, 2005]. However, the simulated mean core velocities were substantially smaller than observed. Other models likewise show weak time-mean currents at intermediate depths [*Jochum and Malanotte-Rizzoli*, 2003; *Brandt and Eden*, 2005; *Eden*, 2006]. In general, the recent model developments have shown that the time-mean current structure and strength improves when switching from low to high resolution [*Hüttl and Böning*, 2006, Figure 3], suggesting that a further reduction of vertical and/or lateral mixing of momentum may improve the simulation of the mean equatorial flow field at intermediate depths.

Between the two westward flowing EIC cores, a weak mean eastward flow was present during the mooring period. At 23°W, the eastward flow was particularly strong from May to September 2005 in the depth range between 300 and 350 m while during the same period one year earlier the flow was westward or only slightly eastward (Figure A2.7). This strong year-to-year variability below the EUC was emphasized by a comparison of two annual mean velocity profiles from 23°W (Figure A2.9). The eastward jet with an annual mean velocity of about 15 cm/s for the period March 2005 to February 2006 (Figure A2.7) was found to be responsible for the equatorial oxygen maximum in the depth range $300-350$ m observed during June - July 2006 (Figures A2.4 and A2.5). An analysis of the vertical scale suggested that the feature is best described by vertical mode number 15 that corresponds to a wavelength of about 600 m in the deep ocean. The temporal as well as vertical scale both agree with characteristics of stacked jets in the deep Atlantic Ocean as previously observed.

The large time scale associated with the stacked jets results in small NDF and correspondingly in large standard errors of the mean zonal velocity profiles below the EUC (Figure A2.1). While the interannual variations may exceed 20 cm/s in the depth range 200 to 500 m, the deeper velocity observations at 35°W show strong interannual fluctuations, as well, with observed interannual fluctuations at 800 m reaching 7 cm/s (Figure A2.2). To estimate the effect of the stacked jets on the mean zonal velocity, the moored means

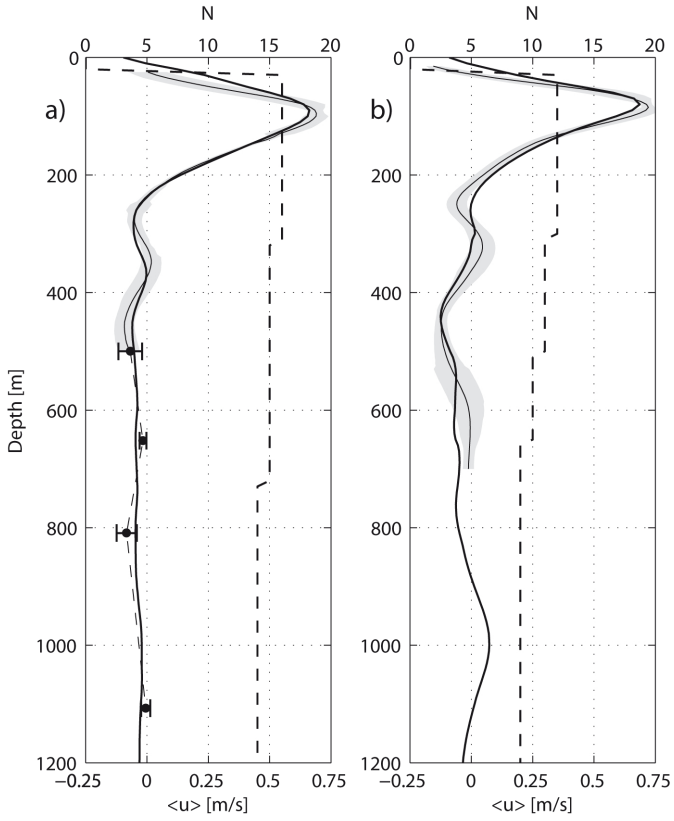

Figure A2.12: Mean equatorial zonal velocity profiles at (a) 35°W and (b) about 23°W, from shipboard observations (thick solid line), moored ADCP observations (thin solid line) with standard error (see Figure A2.1, left panels; shaded), and moored Argonaut observations (thin dashed line, black circles with error bars). The number of available shipboard observations from different ship sections at 35°W (a) and between $29-23$°W (b) is denoted by the thick dashed line (N, upper x axis). [*Brandt et al.*, 2008]

at 35°W and 23°W are compared with mean zonal velocities calculated from shipboard velocity data taken at 35°W (Figure A2.12a) and between $29-23$°W (Figure A2.12b), respectively. The shipboard observations span here a period from 1990 to 2006 (see Section 3.1). The amplitude of the high-baroclinic mode variability in the shipboard means is smaller compared to the moored means. Particularly at 35°W, where a large number of shipboard observations is available, there is an almost depth-independent westward flow below 500 m suggesting the presence of a mean EIC independent on the existence of the stacked jets.

Eastward jets as the one observed from May to September 2005 at 300 to 350 m contribute to the ventilation of the eastern equatorial Atlantic: The fast exchange between western boundary current regime and the eastern equatorial Atlantic could be demonstrated by an isopycnic RAFOS float drifting within a few months along the equator from 35°W to 12°W

(Figure A2.6). By applying a simple advection-diffusion balance it is suggested that the oxygen decrease from 35°W to 10°W within the observed oxygen tongue is mainly balanced by lateral eddy diffusivity, oxygen consumption and diapycnal turbulent diffusivity playing only a minor role. As observed velocities in the SICC and NICC are of similar magnitude as in the eastward jet described here, such balance may hold also for the off-equatorial countercurrents. The strong variability of the oxygen concentration in the region of the SICC and NICC during different years (Figure A2.11) consequently should result from interannual variations in the strength of the off-equatorial countercurrents.

The measurements along the 23°W section revealed that during June - July 2006 the equatorial oxygen maximum associated with the observed eastward jet was characterized by the highest oxygen concentrations in the isopycnal layer defined by potential density surfaces $\sigma_\theta = 26.8\,\mathrm{kg/m^3}$ and $\sigma_\theta = 27.1\,\mathrm{kg/m^3}$ from 4°S to 15°N (Figure A2.3). Besides the zonal supply pathways via the NECC system and the NICC, transporting high-oxygen waters from the western boundary eastward [*Stramma et al.*, 2005, 2008], equatorial zonal jets could significantly contribute, via lateral eddy fluxes, to the ventilation of the OMZ of the tropical North Atlantic.

Glossary

AD	*Angola Dome*
EIC	*Equatorial Intermediate Current*
ENSO	*El Niño Southern Oscillation*
EUC	*Equatorial Undercurrent*
GD	*Guinea Dome*
ITCZ	*Intertropical Convergence Zone*
MOC	*Meridional Overturning Circulation*
NBC	*North Brazil Current*
NBUC	*North Brazil Undercurrent*
NEC	*North Equatorial Current*
NECC	*North Equatorial Countercurrent*
NEUC	*North Equatorial Undercurrent*
NICC	*Northern Intermediate Countercurrent*
OMZ	*Oxygen Minimum Zone*
SEC	*South Equatorial Current*
eSEC	*equatorial SEC*
nSEC	*northern SEC*
SEUC	*South Equatorial Undercurrent*
SICC	*Southern Intermediate Countercurrent*
SSH	*Sea Surface Height*
SST	*Sea Surface Temperature*
STC	*Subtropical Cell*
TAV	*Tropical Atlantic Variability*
TIW	*Tropical Instability Wave*

References

Andrié, C., J. F. Ternon, M. J. Messias, L. Memery, B. Bourlès, Y. Gouriou, and C. Oudot (1998), Chlorofluoromethane distributions in the deep equatorial Atlantic during January - March 1993, *Deep-Sea Res., Part I*, *45*, 903–930.

Arhan, M., H. Mercier, B. Bourlès, and Y. Gouriou (1998), Hydrographic sections across the Atlantic at 7°30N and 4°30S, *Deep-Sea Res., Part I*, *45*, 829–872.

Arhan, M., A. M. Treguier, B. Bourlès, and S. Michel (2006), Diagnosing the annual cycle of the Equatorial Undercurrent in the Atlantic Ocean from a general circulation model, *J. Phys. Oceanogr.*, *36*, 1502–1522.

Arnault, S. (1987), Tropical Atlantic geostrophic currents and ship drifts, *J. Geophys. Res.*, *92*(C5), 5076–5088.

Arnault, S., A. Morlière, J. Merle, and Y. Ménard (1992), Low-frequency variability of the tropical Atlantic surface topography: Altimetry and model comparison, *J. Geophys. Res.*, *97*(C9), 14,259–14,288.

Barnett, T. P. (1983), Interaction of the monsoon and Pacific trade wind system at interannual time scales. Part I: The equatorial zone, *Mon. Weather Rev.*, *111*, 756–773.

Barnier, B., L. Siefridt, and P. Marchesiello (1995), Thermal forcing for a global ocean circulation model using a three-year climatology of ECMWF analysis, *J. Mar. Sys.*, *6*, 363–380.

Berwin, R. W., and J. R. Benada (2000), *TOPEX/POSEIDON Sea Surface Anomaly Product*, User's Reference Manual, Version 1.0, Physical Oceanography Distributed Active Archive Center.

Bjerknes, J. (1969), Atmospheric teleconnections from the equatorial Pacific, *Mon. Weather Rev.*, *97*, 163–172.

Blanke, B., and P. Delecluse (1993), Variability of the tropical Atlantic Ocean simulated by a general circulation model with two different mixed-layer physics, *J. Phys. Oceanogr.*, *23*, 1363–1388.

Boebel, O., R. E. Davis, M. Ollitrault, R. G. Peterson, P. L. Richardson, C. Schmid, and W. Zenk (1999), The intermediate depth circulation of the western South Atlantic, *Geophys. Res. Lett.*, *26*(21), 3329–3332.

Böning, C. W., and F. O. Bryan (1996), Large-scale transport processes in high-resolution circulation models, in *The Warmwatersphere of the North Atlantic Ocean*, edited by W. Krauss, pp. 91–128, Gebr. Borntraeger, Berlin, Stuttgart.

Böning, C. W., and J. Kröger (2005), Seasonal variability of deep currents in the equatorial Atlantic: A model study, *Deep-Sea Res., Part I*, *52*, 99–121.

Bourlès, B., M. d'Orgeville, G. Eldin, Y. Gouriou, R. Chuchla, Y. du Penhoat, and S. Arnault (2002), On the evolution of the thermocline and subthermocline eastward currents in the equatorial Atlantic, *Geophys. Res. Lett.*, *29*(16), 10.1029/2002GL015098.

Bourlès, B., et al. (2003), The deep currents in the eastern equatorial Atlantic Ocean, *Geophys. Res. Lett.*, *30*(5), 8002, doi:10.1029/2002GL015095.

Bourlès, B., et al. (2007), African Monsoon Multidisciplinary Analysis (AMMA): Special measurements in the tropical Atlantic, *CLIVAR Exchanges*, *41*(12), 7–9.

Boyer, T. P., and S. Levitus (1997), *Objective analyses of temperature and salinity for the world ocean on a 1/4 degree grid*, NOAA Atlas NESDIS 11, U.S. Govt. Print. Off., Washington, D.C.

Brandt, P., and C. Eden (2005), Annual cycle and interannual variability of the mid-depth tropical Atlantic, *Deep-Sea Res., Part I*, *52*, 199–219.

Brandt, P., F. A. Schott, C. Provost, A. Kartavtseff, V. Hormann, B. Bourlès, and J. Fischer (2006), Circulation in the central equatorial Atlantic: Mean and intraseasonal to seasonal variability, *Geophys. Res. Lett.*, *33*(L07609), doi:10.1029/2005GL025498.

Brandt, P., V. Hormann, B. Bourlès, J. Fischer, F. A. Schott, L. Stramma, and M. Dengler (2008), Oxygen tongues and zonal currents in the equatorial Atlantic, *J. Geophys. Res.*, *113*(C04012), doi:10.1029/2007JC00435.

Bryan, F. O., and W. R. Holland (1989), A high resolution simulation of the wind- and thermohaline-driven circulation in the North Atlantic Ocean. Parameterization of small-scale processes, in *'Aha Huliko'a, Hawaiian Winter Workshop*, edited by P. Müller and D. Henderson, pp. 99–115, Hawaii Institute Geophysics Spec. Publ.

Bunge, L., C. Provost, J. Lilly, M. d'Orgeville, A. Kartavtseff, and J. L. Melice (2006), Variability of the horizontal velocity structure in the upper 1600 m of the water column on the equator at 10°W, *J. Phys. Oceanogr.*, *36*, 1287–1304.

Bunge, L., C. Provost, and A. Kartavtseff (2007), Variability in horizontal current velocities in the central and eastern equatorial Atlantic in 2002, *J. Geophys. Res.*, *112*(C02014), doi:10.1029/2006JC003704.

Bunge, L., C. Provost, B. L. Hua, and A. Kartavtseff (2008), Variability at intermediate depths at the equator in the Atlantic Ocean in 2000-06: Annual cycle, equatorial deep jets, and intraseasonal meridional velocity fluctuations, *J. Phys. Oceanogr.*, *38*, 1794–1806, doi:10.1175/2008JPO3781.1.

Cane, M. A., and E. S. Sarachik (1976), Forced baroclinic ocean motions: I. The linear equatorial unbounded case, *J. Mar. Res.*, *34*, 629–666.

Cane, M. A., and E. S. Sarachik (1977), Forced baroclinic ocean motions: II. The linear equatorial bounded case, *J. Mar. Res.*, *35*, 395–432.

Carton, J. A., and B. Huang (1994), Warm events in the tropical Atlantic, *J. Phys. Oceanogr.*, *24*, 888–903.

Carton, J. A., X. Cao, B. S. Giese, and A. M. D. Silva (1996), Decadal and interannual SST variability in the tropical Atlantic Ocean, *J. Phys. Oceanogr.*, *26*, 1165–1175.

Chang, P., et al. (2006), Climate fluctuations of tropical coupled systems - The role of ocean dynamics, *J. Clim.*, *19*, 5122–5174.

Davey, M. K., et al. (2002), STOIC: A study of coupled model climatology and variability in tropical ocean regions, *Clim. Dyn.*, *18*, 403–420, doi:10.1007/s00382-001-0188-6.

Delcroix, T., J. Picaut, and G. Eldin (1991), Equatorial Kelvin and Rossby waves evidenced in the Pacific Ocean through Geosat sea level and surface current anomalies, *J. Geophys. Res.*, *96*(Suppl.), 3249–3262.

Dengg, J., C. W. Böning, U. Ernst, R. Redler, and A. Beckmann (1999), Effects of an improved model representation of overflow water on the subpolar North Atlantic, *WOCE Newsletter*, *37*, 10–15.

d'Orgeville, M., B. L. Hua, and H. Sasaki (2007), Equatorial deep jets triggered by a large vertical scale variability within the western boundary layer, *J. Mar. Res.*, *65*, 1–25.

du Penhoat, Y., and A. M. Treguier (1985), The seasonal linear response of the tropical Atlantic Ocean, *J. Phys. Oceanogr.*, *15*, 316–329.

Dynamo Group (1997), *DYNAMO Dynamics of North Atlantic models: Simulation and assimilation with high resolution models*, Berichte aus dem Institut für Meereskunde 294, IfM Kiel.

Eden, C. (2006), Mid-depth equatorial tracer tongues in a model of the Atlantic Ocean, *J. Geophys. Res.*, *111*(C12025), doi:10.1029/2006JC003565.

Eden, C., and C. W. Böning (2002), Sources of eddy kinetic energy in the Labrador Sea, *J. Phys. Oceanogr.*, *32*(12), 3346–3363.

Eden, C., and M. Dengler (2008), Stacked jets in the deep equatorial Atlantic Ocean, *J. Geophys. Res.*, *113*(C04003), doi:10.1029/2007JC004298.

Eden, C., R. J. Greatbatch, and J. Willebrand (2007), A diagnosis of thickness fluxes in an eddy-resolving model, *J. Phys. Oceanogr.*, *37*, 727–742.

Firing, E. (1988), Shallow equatorial jets, *J. Geophys. Res.*, *93*, 9213–9222.

Firing, E., R. Lukas, J. Sadler, and K. Wyrtki (1983), Equatorial Undercurrent disappears during 1982-1983 El Niño, *Science*, *222*, 1121–1123.

Firing, E., S. E. Wijffels, and P. Hacker (1998), Equatorial subthermocline currents across the Pacific, *J. Geophys. Res.*, *103*, 21,413–21,423.

Fischer, J., P. Brandt, M. Dengler, M. Müller, and D. Symonds (2003), Surveying the upper ocean with the Ocean Surveyor: A new phased array Doppler current profiler, *J. Atmos. Oceanic Technol.*, *20*, 742–751.

Fischer, J., V. Hormann, P. Brandt, F. A. Schott, B. Rabe, and A. Funk (2008), The South Equatorial Undercurrent in the western to central tropical Atlantic, *Geophys. Res. Lett.*, *35*(L21601), doi:10.1029/2008GL035753.

Foltz, G. R., and M. J. McPhaden (2006), Unusually warm sea surface temperatures in the tropical North Atlantic during 2005, *Geophys. Res. Lett.*, *33*(L19703), doi:10.1029/2006GL027394.

Foltz, G. R., S. A. Grodsky, and J. A. Carton (2003), Seasonal mixed layer heat budget of the tropical Atlantic Ocean, *J. Geophys. Res.*, *108*(3146), doi:10.1029/2002JC001584.

França, C., I. Wainer, A. Mesquita, and G. Goni (2003), Planetary equatorial trapped waves in the Atlantic Ocean from TOPEX/POSEIDON altimetry, in *Interhemispheric Water Exchange in the Atlantic Ocean*, edited by G. J. Goni and P. Malanotte-Rizzoli, pp. 213–232, Elsevier Oceanographic Series 68.

Fratantoni, D. M., W. E. Johns, T. L. Townsend, and H. E. Hurlburt (2000), Low-latitude circulation and mass transport pathways in a model of the tropical Atlantic Ocean, *J. Phys. Oceanogr.*, *30*, 1944–1966.

Ganachaud, A., and C. Wunsch (2001), Improved estimates of global ocean circulation, heat transport and mixing from hydrographic data, *Nature*, *408*, 453–457.

Gaspar, P., Y. Gregoris, and J.-M. Lefevre (1990), A simple eddy kinetic energy model for simulations of the oceanic vertical mixing: Tests at station PAPA and Long-Term Upper Ocean Study site, *J. Geophys. Res.*, *95*, 16,179–16,193.

Giannini, A., R. Saravanan, and P. Chang (2003), Oceanic forcing of Sahel rainfall on interannual to interdecadal time scales, *Science*, *302*, 1027–1030.

Giarolla, E., P. Nobre, M. Malagutti, and P. Pezzi (2005), The Atlantic Equatorial Undercurrent: PIRATA observations and simulations with GFDL Modular Ocean model at CPTEC, *Geophys. Res. Lett.*, *32*(L10617), doi:10.1029/2004GL022206.

Góes, M., and I. Wainer (2003), Equatorial currents transport changes for extreme warm and cold events in the Atlantic Ocean, *Geophys. Res. Lett.*, *30*(5), 8006, doi:10.1029/2002GL015707.

Gordon, A. L., and K. T. Bosley (1991), Cyclonic gyre in the tropical South Atlantic, *Deep-Sea Res.*, *38*(Suppl. I), 323–343.

Gouretski, V. V., and K. Jancke (1998), A new world ocean climatology: Objective analysis on neutral surfaces, *Tech. Rep. 3*, WHP Spec. Anal. Cent., Hamburg, Germany.

Gouriou, Y., and G. Reverdin (1992), Isopycnal and diapycnal circulation of the upper equatorial Atlantic Ocean in 1983-1984, *J. Geophys. Res.*, *22*, 25,165–25,179.

Gouriou, Y., B. Bourlès, H. Mercier, and R. Chuchla (1999), Deep jets in the equatorial Atlantic Ocean, *J. Geophys. Res.*, *104*, 21,216–21,226.

Gouriou, Y., et al. (2001), Deep circulation in the equatorial Atlantic Ocean, *Geophys. Res. Lett.*, *28*, 819–822.

Gregg, M. C., T. B. Sanford, and D. P. Winkel (2003), Reduced mixing from the breaking of internal waves in equatorial waters, *Nature*, *442*, 513–515.

Grodsky, S. A., and J. A. Carton (2002), Surface drifter pathways originating in the equatorial Atlantic cold tongue, *Geophys. Res. Lett.*, *29*(23), 62–65.

Grodsky, S. A., J. A. Carton, C. Provost, J. Servain, J. A. Lorenzzetti, and M. J. McPhaden (2005), Tropical instability waves at 0°N, 23°W in the Atlantic: A case study using Pilot Research Moored Array in the Tropical Atlantic (PIRATA) mooring data, *J. Geophys. Res.*, *110*(C08010), doi:10.1029/2005JC002941.

Gu, D., and S. G. H. Philander (1997), Interdecadal climate fluctuations that depend on exchanges between the tropics and extratropics, *Science*, *272*, 805–808.

Han, W., P. J. Webster, J.-L. Lin, W. T. Liu, R. Fu, D. Yuan, and A. Hu (2008), Dynamics of intraseasonal sea level and thermocline variability in the equatorial Atlantic during 2002-03, *J. Phys. Oceanogr.*, *38*(5), 945–967, doi:10.1175/2008JPO3854.1.

Haney, L. (1971), Surface thermal boundary conditions for ocean circulation models, *J. Phys. Oceanogr.*, *1*, 241–248.

Hazeleger, W., and P. de Vries (2003), Fate of the Equatorial Undercurrent in the Atlantic, in *Interhemispheric Water Exchange in the Atlantic Ocean*, edited by G. J. Goni and P. Malanotte-Rizzoli, pp. 175–191, Elsevier Oceanographic Series 68.

Hazeleger, W., P. de Vries, and Y. Friocourt (2003), Sources of the Equatorial Undercurrent in the Atlantic in a high-resolution ocean model, *J. Phys. Oceanogr.*, *33*, 677–693.

Hénin, C., P. Hisard, and B. Piton (1986), *Observations hydrologiques dans l'océan Atlantique équatorial (juillet 1982-août 1984)*, FOCAL Vol. 1, Editions de l'O.R.S.T.O.M., Collection Travaux et Documents No. 196, Paris.

Hisard, P., and C. Hénin (1987), Response of the equatorial Atlantic Ocean to the 1983-1984 wind from the Programme Français Océan et Climat Dans l'Atlantique Equatorial cruise data set, *J. Geophys. Res.*, *92*(C4), 3759–3768.

Hisard, P., C. Hénin, R. Houghton, B. Piton, and P. Rual (1986), Oceanic conditions in the tropical Atlantic Ocean during 1983 and 1984, *Nature*, *322*, 243–245.

Hormann, V., and P. Brandt (2007), Atlantic Equatorial Undercurrent and associated cold tongue variability, *J. Geophys. Res.*, *112*(C06017), doi:10.1029/2006JC003931.

Hormann, V., and P. Brandt (2008), Upper equatorial Atlantic variability during 2002 and 2005 associated with equatorial Kelvin waves, *J. Geophys. Res.*, submitted.

Hüttl, S., and C. W. Böning (2006), Mechanisms of decadal variability in the shallow subtropical-tropical circulation of the Atlantic Ocean: A model study, *J. Geophys. Res.*, *111*(C07011), doi:10.1029/2005JC003414.

Hüttl-Kabus, S., and C. W. Böning (2008), Pathways and variability of the off-equatorial undercurrents in the Atlantic Ocean, *J. Geophys. Res.*, *113*(C10018), doi:10.1029/2007JC004700.

Illig, S., B. Dewitte, N. Ayoub, Y. du Penhoat, G. Reverdin, P. D. Mey, F. Bonjean, and G. S. E. Lagerloef (2004), Interannual long equatorial waves in the tropical Atlantic from a high-resolution ocean general circulation model experiment in 1981-2000, *J. Geophys. Res.*, *109*(C02022), doi:10.1029/2003JC001771.

Inui, T., A. Lazar, P. Malanotte-Rizzoli, and A. Busalacchi (2002), Wind stress effects on subsurface pathways from the subtropical to tropical Atlantic, *J. Phys. Oceanogr.*, *32*, 2257–2276.

Izumo, T. (2005), The Equatorial Undercurrent, meridional overturning circulation, and their roles in mass and heat exchanges during El Niño events in the tropical Pacific Ocean, *Ocean Dyn.*, *55*(2), 110–123.

Jochum, M., and P. Malanotte-Rizzoli (2003), The flow of AAIW along the equator, in *Interhemispheric Water Exchange in the Atlantic Ocean*, edited by G. J. Goni and P. Malanotte-Rizzoli, pp. 193–212, Elsevier Oceanographic Series 68.

Jochum, M., and P. Malanotte-Rizzoli (2004), A new theory for the generation of the equatorial subsurface countercurrents, *J. Phys. Oceanogr.*, *34*, 755–771.

Jochum, M., and R. Murtugudde (2006), Temperature advection by tropical instability waves, *J. Phys. Oceanogr.*, *36*, 592–605.

Johnson, E. S., and M. J. McPhaden (1993a), Structure of intraseasonal Kelvin waves in the equatorial Pacific Ocean, *J. Phys. Oceanogr.*, *23*, 608–625.

Johnson, E. S., and M. J. McPhaden (1993b), Effects of a three-dimensional mean flow on intraseasonal Kelvin waves in the equatorial Pacific Ocean, *J. Geophys. Res.*, *98*(C6), 10,185–10,194.

Johnson, G. C., and D. Zhang (2003), Structure of the Atlantic Ocean equatorial deep jets, *J. Phys. Oceanogr.*, *33*, 600–609.

Johnson, G. C., B. M. Sloyan, W. S. Kessler, and K. E. McTaggart (2002), Direct measurements of upper ocean currents and water properties across the tropical Pacific during the 1990s, *Prog. Oceanogr.*, *52*, 31–61.

Kalnay, E., et al. (1996), The NCEP/NCAR 40-year reanalysis project, *Bullet. Amer. Meteorol. Soc.*, *77*, 437–471.

Karstensen, J., L. Stramma, and M. Visbeck (2008), Oxygen minimum zones in the eastern tropical Atlantic and Pacific Oceans, *Prog. Oceanogr.*, *77*(4), 331–350.

Katz, E. J. (1987), Equatorial Kelvin waves in the Atlantic, *J. Geophys. Res.*, *92*(C2), 1894–1898.

Katz, E. J. (1997), Waves along the equator in the Atlantic, *J. Phys. Oceanogr.*, *27*, 2536–2544.

Katz, E. J., R. L. Molinari, D. E. Cartwright, P. Hisard, H. U. Lass, and A. de Mesquita (1981), The seasonal transport of the Equatorial Undercurrent in the western Atlantic (during the Global Weather Experiment), *Oceanol. Acta*, *4*(4), 445–450.

Katz, E. J., P. Hisard, J. M. Verstraete, and S. Garzoli (1986), Annual change of sea surface slope along the equator of the Atlantic Ocean in 1983 and 1984, *Nature*, *222*, 245–247.

Keenlyside, N., and R. Kleeman (2002), Annual cycle of equatorial zonal currents in the Pacific, *J. Geophys. Res.*, *107*(C8), 3093, doi:10.1029/2000JC000711.

Keenlyside, N. S., and M. Latif (2007), Understanding equatorial Atlantic interannual variability, *J. Clim.*, *20*(1), 131–142, doi:10.1175/JCLI3992.1.

Kleeman, R., J. P. McCreary, and B. A. Klinger (1999), A mechanism for generating ENSO decadal variability, *Geophys. Res. Lett.*, *26*(12), 1743–1746.

Knox, R. A., and D. L. T. Anderson (1985), Recent advances in the study of the low-latitude-ocean circulation, *Prog. Oceanogr.*, *14*, 259–317.

Kraus, E. B., and J. S. Turner (1967), A one-dimensional model of the seasonal thermocline: I. A laboratory experiment and its interpretation, *Tellus*, *19*, 88–97.

Kushnir, Y., W. A. Robinson, P. Chang, and A. W. Robertson (2006), The physical basis for predicting Atlantic sector seasonal-to-interannual climate variability, *J. Clim.*, *19*, 5949–5970.

Kutsuwada, K., and M. J. McPhaden (2002), Intraseasonal variations in the upper equatorial Pacific Ocean prior to and during the 1997-98 El Niño, *J. Phys. Oceanogr.*, *32*, 1133–1149.

Latif, M., and A. Grötzner (2000), The equatorial Atlantic oscillation and its response to ENSO, *Clim. Dyn.*, *16*, 213–218.

Liu, Z., S. G. H. Philander, and R. C. Pacanowski (1994), A GCM study of tropical-subtropical upper-ocean water exchange, *J. Phys. Oceanogr.*, *24*, 2606–2623.

Lumpkin, R. (2003), Decomposition of surface drifter observations in the Atlantic Ocean, *Geophys. Res. Lett.*, *30*(1753), doi:10.1029/2003GL017519.

Lumpkin, R., and S. L. Garzoli (2005), Near-surface circulation in the tropical Atlantic Ocean. Part II: Time-mean currents and seasonal variability, *Deep-Sea Res., Part I*, *52*(3), 495–518.

Lumpkin, R., and K. Speer (2003), Large-scale vertical and horizontal circulation in the North Atlantic Ocean, *J. Phys. Oceanogr.*, *33*, 1902–1920.

Luyten, J. R., J. Pedlosky, and H. Stommel (1983), The ventilated thermocline, *J. Phys. Oceanogr.*, *13*, 292–309.

Malanotte-Rizzoli, P., K. Hedstrom, H. Arango, and D. B. Haidvogel (2000), Water mass pathways between the subtropical and tropical ocean in a climatological simulation of the North Atlantic Ocean circulation, *Dyn. Atmos. Oceans*, *32*, 331–371.

Matsuno, T. (1966), Quasi-geostrophic motions in the equatorial area, *J. Met. Soc. Japan*, *44*, 25–43.

McCreary, J. P. (1984), Equatorial beams, *J. Mar. Res.*, *42*, 395–430.

McCreary, J. P., and P. Lu (1994), Interaction between the subtropical and equatorial ocean circulations: The subropical cell, *J. Phys. Oceanogr.*, *24*, 466–497.

McCreary, J. P., J. Picaut, and D. W. Moore (1984), Effects of remote annual forcing in the eastern tropical Atlantic Ocean, *J. Mar. Res.*, *42*, 45–81.

McPhaden, M. J., et al. (1998), The Tropical Ocean-Global Atmosphere (TOGA) observing system: A decade of progress, *J. Geophys. Res.*, *103*, 14,169–14,240.

Mercier, H., M. Arhan, and J. R. E. Lutjeharms (2003), Upper-layer circulation in the eastern equatorial and south Atlantic Ocean in January-March 1995, *Deep-Sea Res., Part I*, *50*, 863–887.

Merle, J. (1980), Variabilité thermique annuelle et interannuelle de l'océan Atlantique équatorial est. L'hypothèse d'un "El Niño" Atlantique, *Oceanol. Acta*, *3*, 209–220.

Merle, J. M., M. Fieux, and P. Hisard (1980), Annual signal and interannual anomalies of sea surface temperatures in the eastern equatorial Atlantic Ocean, *Deep-Sea Res.*, *26*(Suppl. II-V), 77–102.

Metcalf, W. G., and M. C. Stalcup (1967), Origin of the Atlantic Equatorial Undercurrent, *J. Geophys. Res.*, *72*, 4959–4974.

Moore, D., and S. G. H. Philander (1977), Modeling of the tropical oceanic circulation, in *The Sea*, vol. 6, pp. 319–361, John Wiley Interscience, New York.

Moore, D. W., P. Hisard, J. P. McCreary, J. Merle, J. J. O'Brien, J. Picaut, J. M. Verstraete, and C. Wunsch (1978), Equatorial adjustment in the eastern Atlantic, *Geophys. Res. Lett.*, *5*, 637–640.

Ollitrault, M., M. Lankhorst, D. Fratantoni, P. Richardson, and W. Zenk (2006), Zonal intermediate currents in the equatorial Atlantic Ocean, *Geophys. Res. Lett.*, *33*(L05605), doi:10.1029/2005GL025368.

Pacanowski, R. C. (1995), MOM 2-documentation, User's Guide and Reference Manual, *Tech. rep.*, Geophysical Fluid Dynamics Labaratory, Princeton, NJ, USA.

Pacanowski, R. C., and S. G. H. Philander (1981), Parameterization of vertical mixing in numerical models of tropical oceans, *J. Phys. Oceanogr.*, *11*, 1443–1451.

Peter, A.-C., M. L. Hénaff, Y. du Penhoat, C. E. Menkes, F. Marin, J. Vialard, G. Caniaux, and A. Lazar (2006), A model study of the seasonal mixed layer heat budget in the equatorial Atlantic, *J. Geophys. Res.*, *111*(C06014), doi:10.1029/2005JC003157.

Peterson, R. G., and L. Stramma (1991), Upper-level circulation in the South Atlantic Ocean, *Prog. Oceanogr.*, *26*, 1–73.

Philander, S. G. H. (1986), Unusual conditions in the tropical Atlantic Ocean in 1984, *Nature*, *222*, 236–238.

Philander, S. G. H. (1990), *El Niño, La Niña, and the Southern Oscillation*, 293 pp., Academic Press.

Philander, S. G. H., and R. C. Pacanowski (1980), The generation of equatorial currents, *J. Geophys. Res.*, *85*, 1123–1136.

Philander, S. G. H., and R. C. Pacanowski (1986a), A model of the seasonal cycle in the tropical Atlantic Ocean, *J. Geophys. Res.*, *91*, 14,192–14,206.

Philander, S. G. H., and R. C. Pacanowski (1986b), The mass and heat budget in a model of the tropical Atlantic Ocean, *J. Geophys. Res.*, *91*, 14,212–14,220.

Philander, S. G. H., W. J. Hurlin, and A. D. Seigel (1987), Simulation of the seasonal cycle of the tropical Pacific Ocean, *J. Phys. Oceanogr.*, *17*, 1986–2002.

Polo, I., A. Lazar, B. Rodríguez-Fonseca, and S. Arnault (2008), Oceanic Kelvin waves and tropical Atlantic intraseasonal variability: 1. Kelvin wave characterization, *J. Geophys. Res.*, *113*(C07009), doi:10.1029/2007JC004495.

Polo, I., A. Lazar, and B. Rodríguez-Fonseca (2008a), Oceanic Kelvin waves and tropical Atlantic intraseasonal variability: 2. Mechanisms and impacts, *J. Geophys. Res.*, submitted.

Ponte, R., J. Luyten, and P. L. Richardson (1990), Equatorial deep jets in the Atlantic Ocean, *Deep-Sea Res.*, *37*, 711–713.

Provost, C., S. Arnault, N. Chouaib, A. Kartavtseff, L. Bunge, and E. Sultan (2004), TOPEX/Poseidon and Jason equatorial sea surface slope anomaly in the Atlantic in 2002: Comparison with winds and currentmeter at 23W, *Mar. Geod.*, *27*, 31–45.

Rapp, R. H., Y. Yi, and Y. Wang (1994), Mean sea surface and geoid gradient comparisons with TOPEX altimeter data, *J. Geophys. Res.*, *99*(C12), 24,657–24,668.

Rebert, J. P., J. R. Donguy, G. Eldin, and K. Wyrtki (1985), Relations between sea level, thermocline depth, heat content, and dynamic height in the tropical Pacific Ocean, *J. Geophys. Res.*, *90*(C6), 11,719–11,725.

Redler, R., K. Ketelsen, J. Dengg, and C. W. Böning (1998), *A high-resolution model for the circulation of the Atlantic Ocean*, Fourth European SGI/CRAY MPP Workshop, Garching.

Reynolds, R. W., and T. M. Smith (1994), Improved global sea surface temperature analysis using optimum interpolation, *J. Clim.*, *7*, 929–948.

Reynolds, R. W., N. A. Rayner, T. M. Smith, D. C. Stokes, and W. Wang (2002), An improved in situ and satellite SST analysis for climate, *J. Clim.*, *15*, 1609–1625.

Richardson, P. L., and T. K. McKee (1984), Average seasonal variation of the Atlantic equatorial currents from historical ship drifts, *J. Phys. Oceanogr.*, *14*, 1226–1238.

Rossby, T., E. R. Levine, and D. N. Conners (1985), The isopycnal Swallow float: A simple device for tracking water parcels in the ocean, *Prog. Oceanogr.*, *14*, 511–525.

Rossby, T., D. Dorson, and J. Fontaine (1986), The RAFOS system, *J. Atmos. Oceanic Technol.*, *3*(4), 672–679.

Ruiz-Barradas, A., J. A. Carton, and S. Nigam (2000), Structure of interannual-to-decadal climate variability in the tropical Atlantic sector, *J. Clim.*, *13*, 3285–3297.

Schmid, C., B. Bourlès, and Y. Gouriou (2005), Impact of the deep equatorial jets on the zonal transport in the Atlantic, *Deep-Sea Res., Part II*, *52*, 409–428.

Schott, F., J. Carton, W. Hazeleger, W. Johns, Y. Kushnir, C. Reason, and S.-P. Xie (2004a), White paper on a "Tropical Atlantic Climate Experiment" (TACE).

Schott, F., M. Dengler, R. J. Zantopp, L. Stramma, J. Fischer, and P. Brandt (2005), The shallow and deep western boundary circulation of the South Atlantic at $5° - 11°$S, *J. Phys. Oceanogr.*, *35*, 2031–2053.

Schott, F. A., and C. W. Böning (1991), The WOCE model in the western equatorial Atlantic: Upper layer circulation, *J. Geophys. Res.*, *96*(C4), 6993–7004.

Schott, F. A., L. Stramma, and J. Fischer (1995), The warm water inflow into the western tropical Atlantic boundary regime, spring 1994, *J. Geophys. Res.*, *100*, 24,745–24,760.

Schott, F. A., J. Fischer, and L. Stramma (1998), Transports and pathways of the upper-layer circulation in the western tropical Atlantic, *J. Phys. Oceanogr.*, *28*, 1904–1928.

Schott, F. A., M. Dengler, P. Brandt, K. Affler, J. Fischer, B. Bourlès, Y. Gouriou, R. L. Molinari, and M. Rhein (2003), The zonal currents and transports at 35°W in the tropical Atlantic, *Geophys. Res. Lett.*, *30*(7), 1349, doi:10.1029/2002GL016849.

Schott, F. A., J. P. McCreary, and G. C. Johnson (2004), Shallow overturning circulations of the tropical-subtropical oceans, in *Earth's Climate: The Ocean-Atmosphere Interaction and Climate Variability*, edited by C. Wang, S.-P. Xie, and J. A. Carton, Geophysical Monograph Series 147, AGU, Washington, D. C.

Schouten, M. W., R. P. Matano, and T. P. Strub (2005), A description of the seasonal cycle of the equatorial Atlantic from altimeter data, *Deep-Sea Res., Part I*, *52*, 477–493.

Seidel, H. F., and B. S. Giese (1999), Equatorial currents in the Pacific Ocean 1992-97, *J. Geophys. Res.*, *104*(C4), 7849–7863.

Send, U., C. Eden, and F. Schott (2002), Atlantic equatorial deep jets: Space-time structure and cross-equatorial fluxes, *J. Phys. Oceanogr.*, *32*, 891–902.

Servain, J., J. Picaut, and J. Merle (1982), Evidence of remote forcing in the equatorial Atlantic Ocean, *J. Phys. Oceanogr.*, *12*, 457–463.

Servain, J., A. J. Busalacchi, M. J. McPhaden, A. D. Moura, G. Reverdin, M. Vianna, and S. E. Zebiak (1998), A Pilot Research Moored Array in the Tropical Atlantic (PIRATA), *Bullet. Amer. Meteorol. Soc.*, *79*, 2019–2031.

Servain, J., I. Wainer, J. P. McCreary, and A. Dessier (1999), Relationship between the equatorial and meridional modes of climatic variability in the tropical Atlantic, *Geophys. Res. Lett.*, *26*(4), 485–488.

Snowden, D. P., and R. L. Molinari (2003), Subtropical cells in the Atlantic Ocean: An observational summary, in *Interhemispheric Water Exchange in the Atlantic Ocean*, edited by G. J. Goni and P. Malanotte-Rizzoli, pp. 287–312, Elsevier Oceanographic Series 68.

Stramma, L., and F. Schott (1999), The mean flow field of the tropical Atlantic Ocean, *Deep-Sea Res., Part II*, *46*, 279–303.

Stramma, L., J. Fischer, P. Brandt, and F. Schott (2003), Circulation, variability and near-equatorial meridional flow in the central equatorial Atlantic, in *Interhemispheric Water Exchange in the Atlantic Ocean*, edited by G. J. Goni and P. Malanotte-Rizzoli, pp. 1–22, Elsevier Oceanographic Series 68.

Stramma, L., S. Hüttl, and J. Schafstall (2005), Water masses and currents in the upper tropical Northeast Atlantic off northwest Africa, *J. Geophys. Res.*, *110*(C12006), doi:10.1029/2005JC002939.

Stramma, L., P. Brandt, J. Schafstall, F. Schott, J. Fischer, and A. Körtzinger (2008), The oxygen minimum zone in the North Atlantic south and east of the Cape Verde Islands, *J. Geophys. Res.*, *113*(C04014), doi:10.1029/2007JC004369.

Thierry, V., A.-M. Treguier, and H. Mercier (2004), Numerical study of the annual and semi-annual fluctuations in the deep equatorial Atlantic Ocean, *Ocean Modelling*, *6*, 1–30.

Tsuchiya, M., L. D. Talley, and M. S. McCartney (1992), An eastern Atlantic section from Iceland southward across the equator, *Deep-Sea Res., Part A*, *39*, 1885–1917.

van Geen, A., W. M. Smethie, A. Horneman, and H. Lee (2006), Sensitivity of the North Pacific oxygen minimum zone to changes in ocean circulation: A simple model calibrated by Chlorofluorocarbons, *J. Geophys. Res.*, *111*(C10004), doi:10.1029/2005JC003192.

Vauclair, F., and Y. du Penhoat (2001), Interannual variability of the upper layer of the tropical Atlantic Ocean from in situ data between 1979 and 1999, *Clim. Dyn.*, *17*, 527–546.

Verstraete, J.-M. (1992), The seasonal upwellings in the Gulf of Guinea, *Prog. Oceanogr.*, *29*, 1–60.

Visbeck, M. (2002), Deep velocity profiling using lowered acoustic Doppler current profilers: Bottom track and inverse solutions, *J. Atmos. Oceanic Technol.*, *19*, 794–807.

von Schuckmann, K., P. Brandt, and C. Eden (2008), Generation of tropical instability waves in the Atlantic Ocean, *J. Geophys. Res.*, *113*(C08034), doi:10.1029/2007JC004712.

Wacongne, S. (1989), Dynamical regimes of a fully nonlinear stratified model of the Atlantic Equatorial Undercurrent, *J. Geophys. Res.*, *94*, 4801–4815.

Weare, B. C. (1977), Empirical orthogonal analysis of the Atlantic Ocean surface temperatures, *Q. J. R. Meteorol. Soc.*, *103*, 467–478.

Weisberg, R. H., and C. Colin (1986), Upper ocean temperature and current variations along the equator in the Atlantic Ocean during 1983-1984, *Nature*, *322*, 240–243.

Weisberg, R. H., and Y. Tang (1987), Further studies on the response of the equatorial thermocline in the Atlantic Ocean to the seasonally varying trade winds, *J. Geophys. Res.*, *92*(C4), 3709–3727.

Weisberg, R. H., J. H. Hickman, T. Y. Tang, and T. J. Weingartner (1987), Velocity and temperature observations during the Seasonal Response of the Equatorial Atlantic Experiment at 0°, 28°W, *J. Geophys. Res.*, *92*(C5), 5061–5075.

Willebrand, J., et al. (2001), Circulation characteristics in three eddy-permitting models of the North Atlantic, *Prog. Oceanogr.*, *48*, 123–161.

Wyrtki, K. (1975), El Niño - The dynamic response of the equatorial Pacific Ocean to atmospheric forcing, *J. Phys. Oceanogr.*, *5*, 572–584.

Xie, S.-P., and J. A. Carton (2004), Tropical Atlantic variability: Patterns, mechanisms, and impacts, in *Earth's Climate: The Ocean-Atmosphere Interaction and Climate Variability*, edited by C. Wang, S.-P. Xie, and J. A. Carton, Geophysical Monograph Series 147, AGU, Washington, D. C.

Yu, X. R., and M. J. McPhaden (1999), Dynamical analysis of seasonal and interannual variability in the equatorial Pacific, *J. Phys. Oceanogr.*, *29*(9), 2350–2369.

Zebiak, S. E. (1993), Air-sea interaction in the equatorial Atlantic region, *J. Clim.*, *6*, 1567–1586.

Zhang, D., M. J. McPhaden, and W. E. Johns (2003), Observational evidence for flow between the subtropical and tropical Atlantic: The Atlantic subtropical cells, *J. Phys. Oceanogr.*, *33*(8), 1783–1797.

Acknowledgments

At first, special thanks to Prof. Dr. Peter Brandt for his dedicated supervision of this study. Besides I would like to thank Drs. Jürgen Fischer, Marcus Dengler, Noel Keenlyside and Frédéric Marin for helpful discussions, as well as Rainer Zantopp, Tim Fischer and Dr. Andreas Funk for proof-reading. Many thanks also to all my colleagues from the department of Physical Oceanography at IFM-GEOMAR.

The effort of the Kiel FLAME group in developing the model simulations is acknowledged and I particularly thank Dr. Sabine Hüttl-Kabus and PD Dr. Carsten Eden for providing the data; model integrations have been performed using the computing facilities at MLRE, Hamburg supported by the staff of the DKRZ. I am also grateful for allocating shipboard current and hydrographic data by the PIs of the various German, French and US cruises. Moored ADCP measurements were provided by C. Provost as well as B. Bourlès and PIRATA mooring data were made available through the TAO project office. The drifter climatology was developed by R. Lumpkin (NOAA/AOML) in collaboration with S. Garzoli and M. Pazos (NOAA/AOML), J. Redman (CIMAS), and Z. Garraffo (RSMAS, University of Miami). Multimission gridded SSHs were produced by SSALTO/DUACS and distributed by AVISO with support from CNES. Surface wind stress data were obtained from CERSAT, at IFREMER, Plouzané (France). Microwave OI SST data were produced by Remote Sensing Systems and sponsored by the National Oceanographic Partnership Program (NOPP), the NASA Earth Science Physical Oceanography Program, and the NASA REASoN DISCOVER Project.

Funding was received through the Deutsche Bundesministerium für Bildung und Forschung (BMBF) as part of the German CLIVAR project (03F0377B) and of the Verbundvorhaben Nordatlantik (03F0443B), the EU Integrated Project AMMA (004089-2), and the German Science Foundation (DFG) under contract FI 871/1-1.